University of Reading

SCHOOL OF BIOLOGICAL SCIENCE

PhD DISSERTATION

Functional Connectivity Signatures of Visual-Motor Coordination using Spectral Dynamical Analysis

XINZHE LI

SUPERVISORS:

Prof. Yoshikatsu Hayashi   Prof. Slawomir J. Nasuto

October 2018

Abstract

Visual-motor coordination is an essential function of human motion control, which requires interactions of multiple brain regions. Visual tracking is a behavioural task that requires intensive visual-motor coordination, which makes it a good paradigm to study the underlying mechanism of visual-motor coordination. In this research, tracking paradigm was used to study the visual-motor coordination, and both behaviour and electroencephalography (EEG) functional connectivity were analysed.

The behavioural analysis explored the anticipatory characteristic of human motion control. In the tracking paradigm, participants were asked to trace a target moving with constant speed along a circular trajectory. Two different types of tracking paradigm were applied in the research. Firstly, the full visibility tracking trials were performed, in which participants had the full visibility of the target movement. Participants showed weak anticipatory behaviour in the full visibility tracking trials. In order to observe stronger anticipatory behaviour, the intermittent tracking trials were then performed, in which two target-invisible zones were added. It was found that participants applied two distinctive control modes of visual-motor coordination in the target-visible zone and target-invisible zone, respectively. The result showed that the target-invisible zone made participants perform anticipatory control of visual tracking.

In order to identify the brain activities related to visual processing and motion control separately in the visual-motor feedback loops, two reference conditions were designed and compared with the tracking trials. The functional connectivity was defined using phase-locking synchrony, and both static and dynamical features of the network were investigated. For static analysis, the time-averaged graphical properties of functional connectivity were investigated. To investigate dynamical properties, a new dynamical network analysis method was developed based on eigenvector representation of functional connectivity. Both static and dynamic analyses demonstrated significant differences between cortical functional connectivity networks of open and closed visual-motor loop. Additionally, the dynamical network analysis also revealed that the EEG network related to visual-motor coordination undergoes a meta-stable state dynamics in the prime eigenvector space. This method can also potentially be applied to other network system to reveal the meta-stable states structure.

Contents

Chapter 1

Introduction

Motion is the only way that creatures can affect the environment. For humans, visual-motor coordination is an essential way of motion control, as humans perceive majority of information from the visual system. Research has shown that the inter-regional correlations of neural signals play an important role in the motion control of visual-motor behaviour [1, 2, 3]. The collection of these neural correlations also forms a structure of complex network, which is called functional connectivity network, whose topological structure and dynamics could indicate the underlying neural activities corresponding to the motion control. The functional connectivity network specifically related to the visual-motor coordination, however, has not been fully explored. In this study, I investigated the functional connectivity patterns of the human visual-motor coordination behaviour.

Understanding the underlying mechanism of visual-motor coordination would provide an insight into human motion control, and greatly promote the progression of the brain-computer interface (BCI) technology. BCI is an interface that enable direct communication between human brain and external devices [4]. BCI records and translates neural signals and sends them to other devices. A person with BCI can send messages or com-

mands directly from the neural system without using any muscles. BCI could lead to medical use, in which case amputees could recover their mobility with BCI embedded prosthetic limbs, and potential usage of human augmentation. Uncovering the pattern of functional connectivity network corresponding to the visual-motor coordination gives an insight of how the distributed cortical regions integrate into a precess feedback loop, and make decoding the neural activities possible.

The human visual-motor coordination is a complicated process, which involves multiple cortical regions [5]. From the control theory point of view, the whole visual-motor loop can be divided into different functional modules, such as visual feedback modules, tactile feedback, motion control, etc. However, those individual modules could still activate even when participants are not performing visual-motor coordination. For example, the neurons of visual perception would function even the subject doesn't perform any movement. Therefore, it is essential to carefully separate different parts of the visual-motor system. In this study, I designed a set of visual tracking tasks which could separate different parts of the visual-motor loop. Electroencephalograph (EEG) was recorded during the whole behaviour experiment session, and the functional connectivity network was derived from EEG. Both topological analysis and dynamical analysis were performed on the functional connectivity. A new method was developed in order to extract the dynamical properties of the functional connectivity network.

In this dissertation, firstly a literature review will be provided to introduce the necessary background of this research, then the analysis on the behaviour data of participants will be presented. The behaviour data analysis

showed that participants exhibited the anticipatory motion control in the intermittent tracking paradigm. From Chapter 4, I will start to investigate the EEG functional connectivity network. But before directly analysing the neural signal, in Chapter 4 I will develop a new eigenvector-based dynamical analysis method and set up a simulation model of synchronous network to testify our method of functional connectivity. In Chapter 5 and Chapter 6, I will demonstrate the time-averaged topological properties and dynamical properties of the functional connectivity network respectively, and explain how those properties of the network distinguish open and closed visual-motor loop. The results showed that the functional connectivity of the alpha band is related to the motion control, while the functional connectivity of the gamma band is related to the visual feedback control. In the last chapter, all the results will be summarized and concluded. The eigenvector-based dynamical analysis method showed a great potential to uncover the attractor structure of the network evolution, therefore in the last chapter, I will also discuss the possible future directions along this dynamical analysis, which could be applied to reveal the full picture of the functional connectivity dynamics.

Chapter 2

Literature Review

Contents

2.1   Introduction

The literature review of this dissertation includes 3 parts. In the first part, the behaviour studies of human motion control are introduced, which will have two themes, the visual-motor coordination and anticipatory behaviour. The second part of this chapter discusses the neural signal analysis, specifically the functional connectivity analysis, and also talks about

the neural signal research of visual-motor coordination. The last part focuses on the methodology of network analysis, including the topological properties and dynamical analysis.

2.2 Behaviour study of motion control

2.2.1 Visual-motor coordination

Visual-motor coordination, or more generally, the sensorimotor coordination, is a critical ability for motor control of humans. The sensorimotor coordination is a form of referential behaviour [6], in which the action is coordinated with an external object, which is called referent. For example, when a person plays tennis or video games, the motion of that person is coordinated with the tennis ball or visual information shown on the display. For this scenario, the ball or image shown on the display plays the role of referent. In the research, sensorimotor coordination is usually investigated with behaviour tasks in which participants were asked to perform certain type of motion coordinated to visual or auditory cue. Many different variants of behaviour tasks have been applied, including different types of motion (finger tapping, finger flexion, or movement involving the whole upper limb), different cue (visual or auditory stimulation), and different coordination form (in-phase synchrony or anti-phase synchrony).

Tracking paradigm is a visual-motor task in which participants were asked to track a moving target with a tracer which is controlled by the participant, usually both target and tracer were shown on a display. The movement of the target can be either one dimensional or two dimensional, and usually the tracer would share the same moving space with the tar-

get. During tracking, participants have to synchronize their movement with the target, which requires both visual input processing and precise movement control. Different modifications of tracking paradigm have been applied in previous research. There are a number of studies using "force tracking" paradigm [7, 8, 9, 10], where participants usually interact with a force sensor through one or more fingers (usually the thumb and the index finger) to control the tracer. Participants press or do finger tapping to control the position of tracer and try to overlap it with the target. The other type of tracking involves the motion of the whole arm. For example, in Lin's research [11], participants controlled a tracer through a joystick, while the tracer was restricted within a square track. A target moved counter-clockwise along the square track, and participants were instructed to overlap with the target within a tolerance limitation. The drawback of the force tracking paradigm is obvious: it only involves the motion of fingers, which may only result in very limited neural activity of the motor cortex, and the brain signal feature could be hard to observe. Another problem for both paradigms introduced above are the restriction of the degree of freedom. In both cases, the movement of target and tracer were restricted in one dimension. It may also make the visual-motor feedback loop less active for lack of degree of freedom as well as lack of challenge of the task. This study followed the tracking paradigm in Hayashi's work [12], in which participant was asked to control a freely-moving tracer to track a moving target which was moving in a circle trajectory on the display. The advantage of this set up is that the non-restricted movement better simulates natural movement such as locomotion and reaching. Participants used a haptic device to control the tracer, which meant the whole arm was

involved in the movement, while force tracking and other restricted movement paradigms only involve limited degree of freedom, which may not fully activate visual-motor feedback loop as less information flow is required to control the movement.

2.2.2 Anticipatory behaviour of humans

Some of the early studies have noted the anticipatory behaviour of humans. Some very early works [13, 14] have noted that the error between taps and stimuli tend to have positive-biased distribution (taps preceded stimuli) rather than symmetric distribution. Klemmer [15, 16] found that responses of participants were likely to precede, rather than follow, the stimuli in a behaviour task with relatively high frequency of the isochronous stimuli sequence. These positive errors or the preceding of tapping suggest that those participants were performing anticipatory behaviour [17, 18].

People are generally unconscious about their anticipatory behaviour [5]. In the work of Aschersleben [19], participants reported that they had to intend to delay the tap so that they could perfectly synchronize with the visual stimuli, which suggests that the anticipatory behaviour is a spontaneous rather than subjective behaviour. This phenomenon implies that the anticipatory behaviour could result from a specific motion control mode which would be activated unconsciously. The other empirical finding of the anticipatory behaviour is that there are large variance between individuals [20, 21, 22]. In the work of Ishida [23], participants performed a visual tracking task in which they were asked to track a visual target moving at a constant frequency. There were a number of trials with different target moving frequencies in the experiment so that researchers could investigate

the effect of target frequency. They found that the behaviour of participants preceded the target in a finite frequency range. The positive error increased as the function of the target frequency and reached its peak at 1.5Hz, and then decreased as the target frequency increased over 1.5Hz. This result suggested that the anticipatory behaviour of humans is affected by the frequency of the target. Participants showed anticipation only if the frequency of target is within a certain range. They also noted that the positive error of the anticipation was variable for different participants. A number of different theories have been proposed to explain the anticipatory behaviour, but none of them could provide a satisfactory explanation and more evidence is needed [20, 5]. In this study, the behaviour analysis was performed to investigate the anticipatory behaviour.

2.3   The neural network

The human brain can be seen as a huge scale network of millions of neurons anatomically. It is widely accepted that brain as a complex neural network has capacity to store and process information [24]. Some theoretical models, such as Hopfield network [25], have demonstrated that it is possible to store information in the network structure. Therefore, the neural network structure is the key for understanding the mechanisms of human cognition and behaviour. With the framework of graph theory from mathematics, complex network has become a powerful model to describe and study the brain activity.

The brain network demonstrates a hierarchical structural [26], where in the bottom of the hierarchy are the small clusters composed by local

neurons, which are called neural assemblies [27, 28, 29]. Cognitive acts of humans are generally thought to be related to specific neural assemblies [30]. In a specific neural assembly, neurons are connected by selective interactions, which means that they preferentially connect with a sub-network of neurons that are interconnected with each other. Those interconnections are typically reciprocal [31]. A specific neural integration which is called phase synchrony plays an important role in the interaction of these local networks [32].

2.3.1 Neural correlation

Phase and synchrony have been given many different definitions in different works. In a general sense, two signals x and y are considered correlated with each other if one of the signals is related with the other. The most commonly used measurement of correlation is the Pearson correlation coefficient which evaluates the product of the variance of the two signals:

$$r_{xy}(\tau) = \frac{\sum_u (x_u - \overline{x})(y_{u-\tau} - \overline{y})}{S_x S_y} \qquad (2.1)$$

where S_x and S_y are the sample standard deviation of the signals x and y respectively, while $\overline{x}$ and $\overline{y}$ are the mean values of the signals. τ is the offset between the two signals, so that the Pearson correlation in this form also considers the coupling with a constant time-lag. The range of r is $[-1, 1]$. The higher the absolute value of r is, the stronger linear correlation of the two signals it suggests. This measurement can also be used on band passed data if a specific frequency band is of interest [33].

While the correlation coefficient take into consideration the phase of

the signal, phase synchrony specifies the phase correlation between signals. Different definitions can be applied on "synchrony" of phase. A generally used one is the in-phase synchrony which is defined as phase equivalence between two signals x and y:

$$\phi_{x,u} = \phi_{y,u} \qquad (2.2)$$

where u refers to time. However, this measure only account for one of many types of phase synchrony. Another measurement of phase synchrony is the phase coherence [34] which is defined as following:

$$C = \frac{1}{T} |\sum_{u=1}^{T} e^{i(\phi_{x,u} - \phi_{y,u})}| \qquad (2.3)$$

where T is the width of time window. From Equation (2.3), it can be learned that phase coherence C would have a large value if the phase difference $\phi_{x,u} - \phi_{y,u}$ within the time window keeps constant, no matter what exact value the phase difference takes. In other words, this measurement characterises the consistence of the relative phase difference. Therefore, the phase coherence can not only detect the in-phase synchrony of the two signals, but also the synchrony with a certain time-lag. In this dissertation, the latter situation is specifically named as "phase-locking". However, the time window limits the temporal resolution of this measurement, which means that the relative phase difference changes inside the time window would be ignored. In this research, rather than calculating the average phase difference of the time window, the phase coherence C was calculated with a new method which is based on the Euclidean distance of the time window segments of the phase time series. The details will be described

13

in Chapter 4. By this way, the temporal resolution of phase difference was not limited by the time window resolution any more.

Evidence found in the research of visual binding has shown that phase synchrony mediates communication in the neural networks. Visual-binding research studies the question about how the different visual characteristics of an object, like shape, color, position, motion, are brought together into a unified image given that those visual characteristics are processed in distributed brain regions. Phase synchronization have been found in the local field potential (LFP) studies of Roelfsema et.al. [1, 35, 36]. The local field potential (LFP) records the summed electrical signal generated by multiple nearby neurons within a small volume of brain tissue. In their experiment, cats were trained to response to a visual stimulus, and the LFP of the visual, somatosensory, and motor areas of cats' cortex were recorded and analysed over time. They found a selective increase of the phase synchrony in LFPs of visual-parietal cortex as well as parietal-motor cortex. The synchronization pattern rose simultaneously when the animal moved its attention on the visual stimulus, and disappeared when the animal finished the task and had the reward. This research provides a direct evidence that large-scale phase synchrony emerges along with the visual-motor task. Bressler [2, 3] also reported that phase synchrony was observed from the cortex of monkeys who were trained to perform a visual discrimination task. The researchers observed a dynamical pattern of the phase synchrony in the beta and gamma bands synchronisation strength changed during the visual-motor task. Phase synchrony is also observed in EEG signals, which are the electrical potentials recorded by scalp surface electrodes. Study of Rodriguez et.al. [37] investigated the perception of high-contrast human

face images. The images were presented both normally or upside down, the latter way of presenting the image made the human face hardly recognizable. The long-range synchrony between occipital, parietal and frontal areas were observed during the face recognition session, and disappeared when the image were shown upside down. These studies demonstrated that phase synchrony plays an important role in the visual-motor coordination.

2.3.2 Neural connectivity

As we saw in the previous section, the emergence of phase synchrony is usually accompanied with certain behaviour task. It is generally believed that the brain regions synchronized with each other are functionally correlated, and this functional correlation is related to the behaviour task that an individual is currently performing. If there are phase synchrony correlations between multiple regions of the brain, a network structure emerges. Studying the topological structure of the network could reveal the information of the underlying neural activities. Neural networks are usually studied from two different aspects, the functional connectivity and the structural connectivity. The functional connectivity is the network whose connections denote the statistical coherence of neural signals, while the structural connectivity is the network whose connections denote the anatomical connection of different brain parts. The connections in the functional connectivity are virtual and defined by neural signal analysis, while the connections of the structural connectivity usually have physical form, such as synapses or axonal projections. Structural connectivity analysis has been applied in planar microelectrode array (MEA) studies [38], where the synaptic connection of neurons can be clearly observed.

In human brain studies, however, structural connectivity analysis is less feasible due to the tremendous scale of brain network which is difficult to study if every physical neural connection is considered. The functional connectivity is derived from neural signals, so it is more commonly used in the research with human subjects. The definition of nodes and links of a functional connectivity network largely depends on the neural signal acquisition method. For example, in fMRI studies, the nodes of the functional connectivity are usually called Region of Interest (ROI) which is an abstract point that represent a certain surrounding region of the brain, while the links are usually weighted by the Pearson correlation coefficient of the corresponding two signals [39]. With EEG recording, however, the nodes are physically bound to the electrodes. As EEG signals have much higher temporal resolution than fMRI signal, more different methods determining the weight of network links have been developed [40]. Phase-locking synchronization which was employed in the this work is one of those measures that used to define the non-directed functional connectivity. It is generally believed that phase-locking synchrony plays an important role in the neural information transmission process [41, 42, 43]. It has been found that the degree of phase synchronization is related to the pathological activity of epilepsy patients [34]. Also phase locking synchrony was used to define functional connectivity [44, 45]. In this work, functional connectivity is derived from EEG. Characterized by the high temporal resolution, EEG is an ideal neural signal for investigation of dynamical property of functional connectivity.

2.3.3 Neural signature of visual-motor coordination

Experimentalists have shown that cortical cross-regional correlations play an important role in visual-motor coordination. Mehrkanoon et.al. [46] investigated corticomuscular coherence in the dynamical visual-motor task of human participants. They measured the synchrony with time-frequency coherency and this result showed that EEG synchronized with electromyographic (EMG) signal in the beta band, while participant was exerting constant force on the object. However, when participant changed the output force, the corticomuscular coherence in the beta was replaced by coherence in the alpha and gamma band. This study suggested that neural activities in the alpha and gamma bands involve movement prediction and error correction process. In the work of Rilk et. al. [7], participants were instructed to track an irregularly fluctuation target shown on the screen through a force sensor held by index finger and thumb. They demonstrated that better performance was associated with higher occipitocentral coherence, while high tracking error was associated with stronger fronto-central coupling. There are also a number of reports suggesting that the coherence of the alpha band would increase in the visual motor task comparing with the rest state [8, 9]. To sum up, current research shows that visual-motor coordination involves coordination of multiple cortical regions through multiple frequency bands synchronization. However, those research only focused on the individual coherence rather than the overall topological structure of the neural coherence network. The study reported in this dissertation investigates both topological and dynamical properties of the neural functional connectivity network related to the visual-motor coordination behaviour of humans.

2.4   Network theory

With the framework of graph theory from mathematics, complex network has become a powerful model to describe and study the brain activity. A network, which is often called a graph in the graph theory of mathematics, is a representation of the topological structure abstracted from the physical entity of the system. Therefore, the network can be noted as an ordered pair $G = (V, E)$, where V refers to the set of nodes or set of vertices, and E refers to the set of connections, or the set of edges, between the nodes. The connections of a network can be either weighted or unweighted. Connections of an unweighted network are homogenous, while in weighted networks, the weight of connections represents a specific property of the network, the actual interpretation depends on the nature of the network itself. In the research of neural connectivity, the network connections are first weighted by the measurement of the coherence of the neural signal, and then usually binarized to unweighted network connection with a threshold [47, 48]. The binarization of network connections can make the main topological features of the network stand out by pruning the weak connections, but caution must be paid as a bad selection of threshold could lead to loss of topological structure information of the network [47]. The choice of threshold can be arbitrary, but usually related with the distribution and the properties of the coherence measurement [49]. Each connection can also have its own direction, which represents the asymmetric effects from one node to another. The network with directed connection is called directed network, while the undirected network only have undirected connections, which represent the symmetric interactions between nodes. The directed network can better represent a system than the undirected network if the

system has asymmetric effects between its nodes. If we assume symmetric interaction between nodes, however, the undirected network would be a better choice given its simplicity.

The method that modeling a system from its network of interactions has been applied in many different fields including computer science, communication, social dynamics, and marketing [50, 51]. As the brain naturally has a network structure, this approach has been extensively used in the neuroscience and psychology [52, 47, 53].

2.4.1 Topological property measurement

A network is an abstractive representation that specifically focuses on the topological structure of a system. For that purpose, many different measures have been developed to quantitatively describe the topological structure of the network. The most common measures are introduced below [52]:

Node degree

The degree of a node is the number of connections attached to the node. In the case of a weighted network, the degree of a node is the sum of the weights of all the connections attached to the node. It is one of the most fundamental measures of a network. The degrees of all the nodes in the network propose the degree distribution, which is an important characteristic of a network [54]. In this research, this property was not investigated, so the details of the degree distribution won't be introduced here.

Network density

Network density or connection density is the ratio of the actual number of connections versus the maximum possible connections number. A network with low connection density can be described as a "sparse" network, although the "sparse" is an arbitrary criteria.

Clustering coefficient

Clustering coefficient describes how likely nodes tend to gather into a cluster. An adjacent node n_i, or neighbour, of a node n_j is a node that directly connected to node n_j with a connection e_{ij}. The neighbourhood of node n_j is the set of all its neighbour, which can be written as $N_i = \{n_j : e_{ij}\}$. If two neighbours of a node are also connected with each other, which creates a triangle, these three nodes are considered as a micro cluster. The local clustering coefficient of a node is the ratio of the actual number of triangles within the neighbourhood of the node versus the maximum possible number of triangles [55]. Therefore, the local clustering coefficient can be defined as

$$C_i = \frac{2\left|\{e_{jk} : n_j, n_k \in N_i, e_{jk} \in E\}\right|}{k_i(k_i - 1)} \tag{2.4}$$

where k_i is the total number of neighbours for node n_i. The denominator $\frac{k_i(k_i-1)}{2}$ is the maximum possible number of connections in the neighbourhood N_i, while the numerator is the number of actual connections in the neighbourhood. The global clustering coefficient is the average of the local clustering coefficient of all the nodes.

Path length and efficiency

The shortest path length is another measure describing the connection distribution of the network. A path between two nodes m and n is a sequence of connections which connect the two nodes [56]. The length of a certain path is the number of connections in the path (in the case of unweighted network) or the sum of the connections weights in the path (in the case of weighted network). The shortest path length describes the topological distance between nodes in the network. In the context of neural network, it could indicate how fast the information is travelling between nodes. Efficiency is the reciprocal of the shortest path length between two nodes. As it is difficult to define the shortest path length in the network with many disconnected subnetworks, efficiency is usually applied to describe the topological distance of those disconnected nodes in this situation.

There are also other measurements characterizing specific topological structures, such as centrality, which measures how likely the node is a hub in the network. By investigating those topological properties, one could characterise the network topological structure. This research investigated the network density, global clustering coefficient, and mean efficiency of the functional connectivity.

2.4.2   Eigenspectrum of the network

A network $G = (V, E)$ can be represented as an adjacency matrix A, whose dimension equals to the number of nodes, and its entry (i, j) is the weight of connection between nodes i and j. In an unweighted network, (i, j) would be 1 is the two nodes are connected, otherwise (i, j) would be 0.

An eigenvector v of the adjacency matrix is a non-zero vector that satisfy:

$$Av = \lambda v \tag{2.5}$$

where λ is a scalar, which is called eigenvalue of the corresponding eigenvector. Linear algebra has proven that eigenvectors of a matrix contain its information fully [57]. The set of all the eigenvalues and corresponding eigenvectors of the matrix is called eigenspectrum, which includes much information of the network topological structure. The eigenvector corresponding to the largest eigenvalue, which is called prime eigenvector, carries significant information about the existing small module structure of the network. Eigenvectors, as a low dimensional projection of the network adjacency matrix, have been extensively applied in the network science. One of its most common application is network cluster detection. Research of Allefeld [58] has demonstrated that the values of eigenvalues indicate the size of each cluster, while the entries of the corresponding eigenvectors suggest the membership nodes. In the paper, they showed that all the eigenvalues larger than 1 indicate clusters of the network, and the cluster membership of the nodes can be learnt by observing the entries of the corresponding eigenvectors. There are also other clustering methods that combine the eigenspectrum with other clustering algorithm in order to get a better partition of the network [59]. In this research, the prime eigenvector was used as a low dimensional representation of the dynamical functional connectivity network. It captures the main structure of the network, and the fact that it only contains a part of network information makes it resistant from topological noise. Converting the network time series to prime eigenvector time series actually draw a trajectory in the prime eigenvector

space, which reveals the dynamics of the network.

2.4.3 Dynamical properties of network

Dynamical network is an extension of the complex network model, with the whole topological structure evolving over time, which can be represented as a time sequence of network snapshots. The neural network is a transient network as neural signals change in the scale of millisecond, which could generate distinctive topological structure in a short time, and that makes it necessary to study the dynamical details of the neural networks [52]. In the context of dynamical functional connectivity, the connections, which are the interaction of neural signals, evolve along with time and changes the topological structure of the network, while the nodes, which represent specific cortex areas, are usually unchanged during the whole session. By analysing the dynamical functional connectivity, the change of the neural activity as a function of time can be uncovered.

Different methods have been developed to investigate the dynamical network. One type of the methods focuses on the changes of each individual connections, in which the time series of network instances can be seen as a collection of time sequences of individual connection. However, tracking the history of every connection creates huge dimensionality, given that the evolvement of individual connections may not only be affected by its own historical snapshots, but also by the the history of other connections. Grindrod [60] proposed a simplification on this model, where the time sequences of individual connections were assumed to be Markovian and independent from time sequences of other connections. With these extra restrictions, the dimension of the network time series has been greatly

reduced. There are also methods which extend the clustering algorithms of static networks and apply them on dynamical networks by considering time as an additional dimension of network. In the work of Mattar et.al. [61], virtual links were defined between the same nodes on different temporal snapshots of the network. Each snapshot of the network is an instance of the static network, which can be seen as a slice in the network time series. By defining the connections between slices the dynamical connectivity becomes a 3-dimensional network, with two spatial dimensions and one additional temporal dimension. Then, the community detection methods of static networks can be applied to this 3-dimensional temporal-spatial networks. However, the performance of the static network algorithm on this 3D network would be largely affected by the way of defining the temporal links. Another way of investigating the network dynamics is to collapse the whole network into a lower dimensional representation, such as the specific topological measures like clustering coefficient or shortest path length. This model makes it easier to analyse the time series of the network representation [62, 63, 48, 64, 65, 66]. In this study, a new dynamical analysis method which reduces the dimensionality by projecting the network onto its prime eigenvector and makes use of the eigenvector representation was developed and applied on the EEG functional connectivity. This method revealed the meta-stable state dynamics of the functional connectivity evolution.

Chaos is an interesting phenomenon often observed in a nonlinear dynamical system. A chaotic system has a well defined dynamics but its sensitivity to the initial conditions result in that small disturbances would cause completely different future trajectories of the system [67]. Therefore, although the behaviour of chaotic systems are well defined, they are

somehow unpredictable in the long term [68]. Chaos phenomenon has been observed in many real world systems [69, 70, 71]. The brain has been proved to be manifest chaotic behaviour [72], thus reflecting this in the neural signal. The main evidence is from the research of neuron spike firing [73, 74]. It was found that the phase space which was expanded by the successive firing interval I_n and I_{n+1} showed the chaotic dynamics. Research of Schiff [75] has even managed to induce the chaotic firing of neural spikes by applying electrical stimulus. There are also reports of chaos from EEG studies [76, 77]. Chaotic patterns were also observed from EEG of patients who were anesthetized with sevoflurane [77]. This study made a primitive exploration of the chaotic property of dynamical functional connectivity, which will be shown in Chapter 6.

2.5 Conclusion

This literature review has introduced the behaviour research of visual-motor coordination, the neural functional connectivity analysis, and the complex network analysis. In the first section, tracking paradigm and anticipatory behaviour were introduced. In the second section, it has been shown that the neural coherence between different regions of cortex plays an important role in the visual-motor coordination, yet the overall network structure of the neural correlation has been seldom studied. This research studied both static topological and dynamical properties of the functional connectivity corresponding to the visual-motor coordination. The next chapter will discuss the behavioural analysis, which demonstrated that participants exhibited anticipatory behaviour in the tracking paradigm,

Chapter 3

Behavioural Experiments and Analysis

Contents

3.1   Introduction

This chapter introduces the behavioural analysis performed in this work. In order to investigate the visual-motor coordination and anticipatory behaviour of humans, behavioural experiment of tracking paradigm was performed in this work. Two different types of tracking paradigm were performed. In the full visibility tracking trials, participants took control of a

tracer with a haptic device and were asked to use the tracer to track a visual target on the display. The target moved in a circular trajectory at a constant speed. In the intermittent tracking trials, participants were asked to complete the same task as in the full visibility tracking trials, but the target became hidden and invisible in two regions on the display. In these target-invisible zones, participants were forced to anticipate the position of the target and were expected to show stronger anticipatory behaviour. There were 3 different levels of target speed in both types of tracking paradigm. Average phase difference between the tracer and the target were analysed. Anticipatory behaviour, which was indicated by positive mean phase difference (tracer preceded target), was found in the intermittent tracking trials.

It is widely believed that there is an anticipatory mechanism in the central neural system of animals and humans to compensate the delay in the visual-motor coordination [78, 79, 80, 81, 82, 83]. A number of studies in which the visual tracking experiment was applied to explore the anticipatory behaviour have been done [84, 85, 86, 87, 88]. When participants acted in anticipatory behaviour in the experiment, their motion preceded the target or acted before the cue in the experiments [5]. It has been reported that the speed of target is essential for the activation of the anticipatory behaviour [89]. When the speed of target is high, human behaviour would switch to a specific anticipatory behaviour mode which results in stronger anticipation of movement [23].

The behavioural analysis showed that the intermittent tracking is able to exhibit the anticipatory behaviour of humans. Two distinctive control modes of visual-motor coordination were found in the intermittent tracking

trials. These two different control modes corresponded to the target-visible zone and target-invisible zone, respectively, which means that participants kept switching their control modes depending on the visibility of the target in the intermittent tracking trails. It was also shown that high speed of target would result in stronger anticipatory behaviour than the low speed of target. This chapter first describes the experimental setup, then shows the analysis of the behaviour data.

3.2   Full visibility tracking paradigm

This research applied visual-motor tracking paradigm as the behaviour task to investigate the anticipatory behaviour of human movement. Participant was required to track a moving target on the display through upper limb motion. This paradigm was introduced in Ishida's work [23], while modifications have been made on it in this research. Two types of reference trials were designed and applied in this experiment in order to single out different components of visual-motor feedback loop. EEG signals were recorded for all the trials, and related analysis will be shown in the following chapters.

3.2.1   Methods

3.2.1.1   Tracking trial

In tracking trials two filled circles were shown on the display. The red one is the target while the green one is the tracer. The target moved along a circular orbital with a fixed speed, while the tracer was controlled by participant through a haptic device. The participant was instructed to
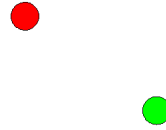
Figure 3.1: Screenshot of the experiment. The red circle is the target, while the green circle is the tracer controlled by the participant.

synchronise the trajectory of tracer with the target as accurate as possible. The screenshot from an actual experimental trial during the short break is shown in Figure 3.1. 3 levels of fixed angular speed were applied in tracking trial, which were 0.1Hz, 0.5Hz, 1.0Hz. Each participant took 20 tracking trials for every speed, and each trial lasted for 40 seconds. The order of tracking trial speed were pseudo-randomised. There was a 10-second short break between each trial, and a long break between every 12 trials. The long break was between 3-5 minutes, it was decided by each participant. During the 10-second short break, there was a countdown in the upper right corner of the screen to notify participant how many seconds left before the next trial. During every tracking trial, a score was displayed in the upper left corner of the screen. This purpose of the score was to keep the participant focusing on the task rather than encouraging the anticipatory behaviour, so it was calculated from the variance of the phase difference between the tracer and the target.
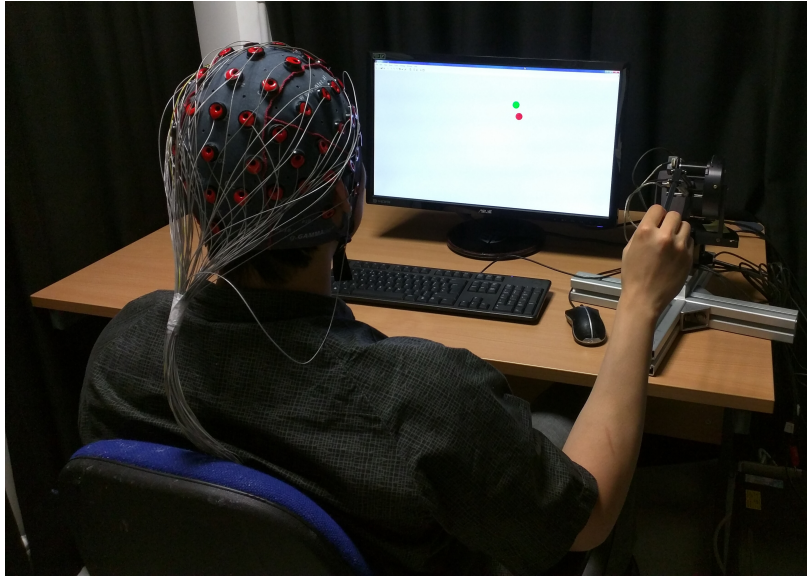
Figure 3.2: Participant was holding the haptic device and facing the screen with both target and tracer shown. Informed consent has been obtained from the participant for the publication of identifying images in an online open-access publication.

3.2.1.2 Reference trials

The visual-motor coordination engaged in the tracking trials is a complex process where multiple functions of brain are activated, such as the visual processing and the movement control of limbs. In order to separate the neural signals corresponding to different components of the visual-motor feedback loop, two reference trials were designed. In the motion only trial (MO), participants were instructed to move the tracer in a circular trajectory at a constant but arbitrary speed, while the target was not shown on the display. Therefore, participants did not perform tracking but simple circular movement. In the visual only trial (VO), participants did not take control of the tracer but were asked to passively observe a pre-recorded tracking trial with both target and tracer shown on the display. In VO trial, participant received exactly the same visual input as in

tracking trials, while participant did not perform any control or movement. Both MO and VO trials lasted for 40 seconds, and were performed by 20 times for every participant.

3.2.1.3 Behavioural data analysis

If participant was performing the anticipatory behaviour, the tracer controlled by the participant would precede the target and "lead" the motion, which resulted in a positive phase difference between the target and the tracer. Otherwise, the tracer should fluctuate around the target, which could result either positive or negative error. According to the work of Ishida [23], the phase differences of the tracking trials follow a Gaussian distribution, and the expectation of the distribution would be positive if the participant showed anticipatory behaviour. Therefore in this study, the phase differences between the target and tracer were fitted into a Gaussian distribution and the mean of the distribution was calculated. The same processes were performed for all the tracking trials, and statistical tests were performed to examine if the distribution mean was larger than 0. The overall result is shown in Figure 3.3, while the results of individual participants are shown in Figure 3.4~3.6.

3.2.2 Results

T-tests were performed on all the three speed levels of averaged participants mean phase difference with the null hypothesis that the mean phase is not significantly different from 0. Results of the t-tests showed that the mean phase differences of all the speed levels were significantly smaller than 0 ($p < 0.05$), which means that participants did not per-
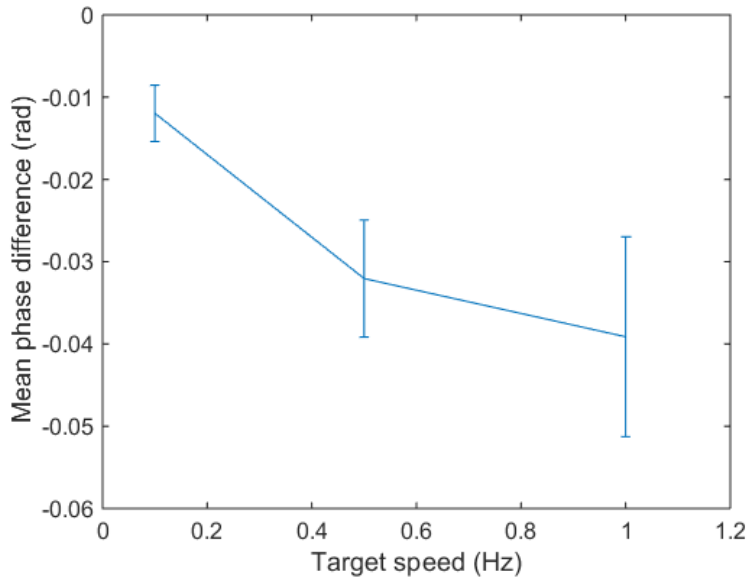
Figure 3.3: The averaged participants mean phase difference of the full visibility tracking trials. The horizontal axis represents the speed of the target in frequency, while the vertical axis represents the mean phase difference of different trials. Each error bar represents the standard error of the mean value.

form the anticipatory control of tracking. Also a decreasing tendency of the mean phase difference was observed, which indicates that participants' performances were largely affected by the task difficulty. However, looking at the individual trials, a huge participant variance can also be found. A common feature for all the participants is that the variance of the phase difference distribution (not shown) increases along with the target speed. The variance of the phase difference distribution can indicate the difficulty of the task. As the target speed increases, the variance becomes larger, which suggests that the difficulty of the trial increases with the speed. The t-test at the significant level $\alpha = 0.05$ has been done for each average phase difference of all the participants, 2 out of 14 participants showed at least 1 positive average phase difference among the 3 speed levels (Participant
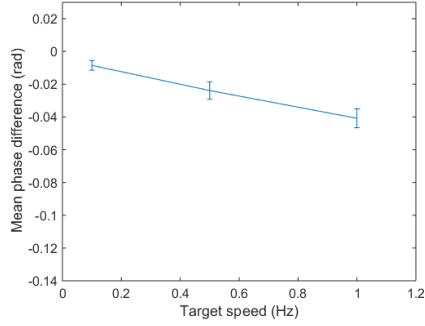
(a) Participant ID = dx
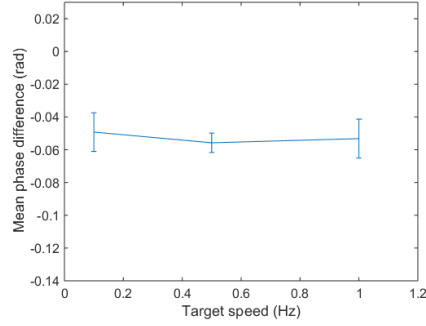
(b) Participant ID = gj
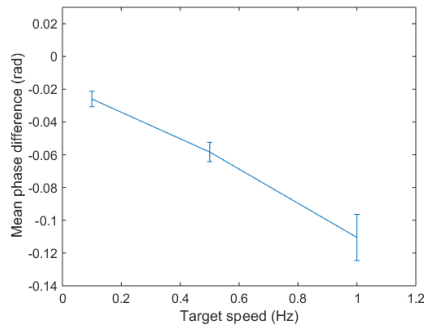
(c) Participant ID = ha
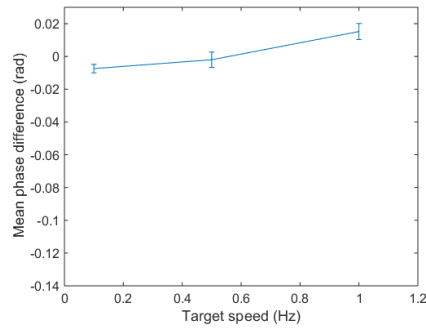
(d) Participant ID = hl
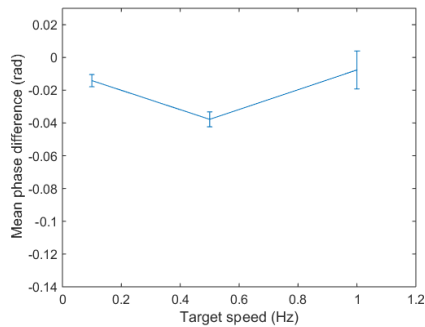
(e) Participant ID = lh
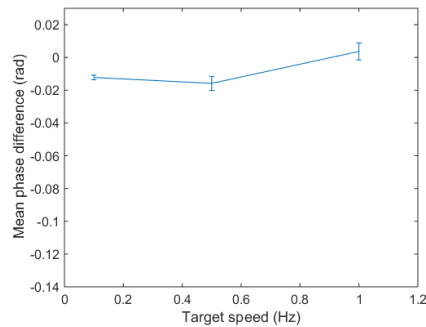
(f) Participant ID = lz

Figure 3.4: Behavioural data of individual participants (part 1). Each subfigure stands for the performance of one single participant, with the participant ID shown in the subtitle. Each error bar represents the standard error of the mean value. The horizontal axis represents the speed of the target in frequency, while the vertical axis represents the mean phase difference of different trials, and each central point represents a mean of 20 parallel trials.
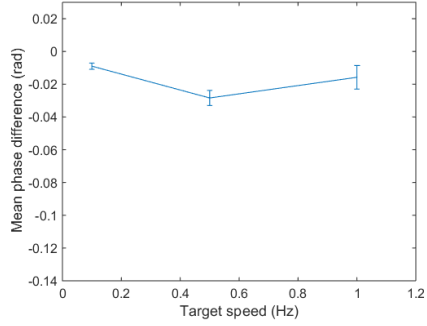
(a) Participant ID = oz
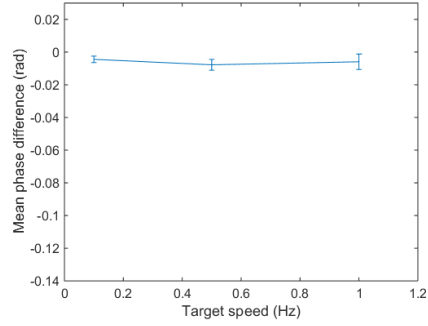
(b) Participant ID = sx
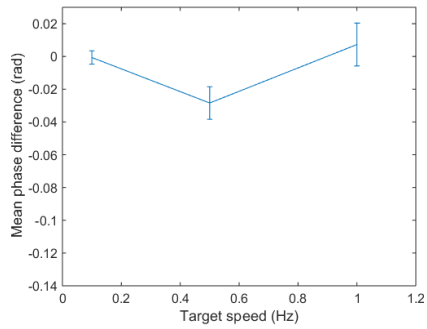
(c) Participant ID = wa
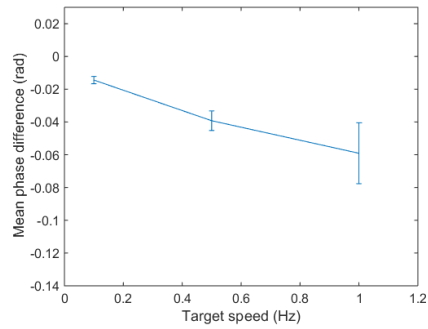
(d) Participant ID = yn
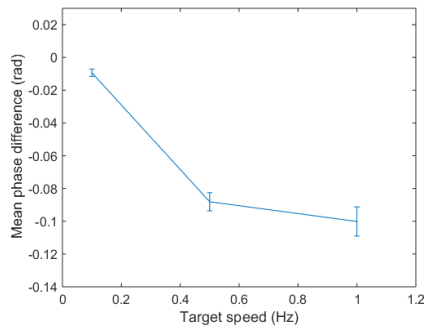
(e) Participant ID = zc
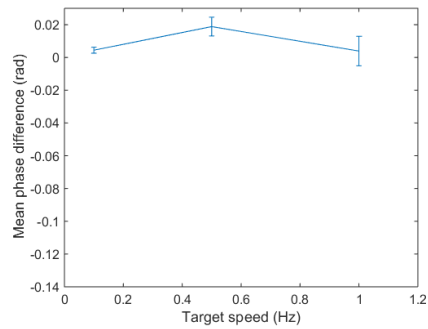
(f) Participant ID = zd

Figure 3.5: Behavioural data of individual participants (part 2). Each subfigure stands for the performance of one single participant, with the participant ID shown in the subtitle. Each error bar represents the standard error of the mean value. The horizontal axis represents the speed of the target in frequency, while the vertical axis represents the mean phase difference of different trials, and each central point represents a mean of 20 parallel trials.

(a) Participant ID = zh   (b) Participant ID = zj
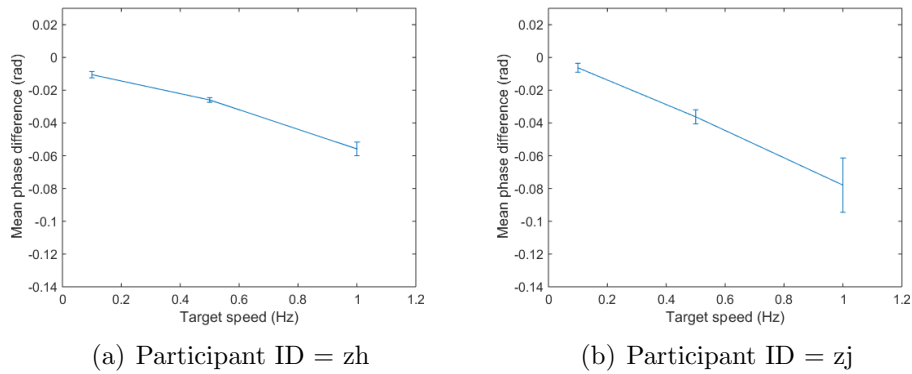
Figure 3.6: Behavioural data of individual participants (part 3). Each subfigure stands for the performance of one single participant, with the participant ID shown in the subtitle. Each error bar represents the standard error of the mean value. The horizontal axis represents the speed of the target in frequency, while the vertical axis represents the mean phase difference of different trials, and each central point represents a mean of 20 parallel trials.

ID = hl, zd), all the other participants showed negative average phase difference for all the speed levels. According to the different patterns of the average phase difference versus speed relation, the results of individual participant can be generally divided into two types. The first type can be represented by the example of Figure 3.4(c), which has monotonic decreasing average phase difference as the target speed increases. This type includes 6 out of 14 participants (participant ID = dx, ha, yn, zc, zh, zj). All the other participants (Participant ID = gj, hl, lh, lz, oz, sx, wa, zd) can be included into the other type, average phase difference of which did not show a monotonic decrease along with the speed levels. Among them, results of 6 participants (Participant ID = gj, lh, lz, oz, sx, wa) show the minimum at 0.5Hz.

3.2.3   Discussion

The overall averaged mean phase difference in Figure 3.3 shows negative mean phase differences and decreasing trend, suggesting the participants did not show the anticipatory behaviour in the full visibility tracking trials. From the individual results in Figure 3.4 to 3.6, it can be found that the performances of participants were quite variant. Participants performances can be classified as two types. In the first type (participant ID = dx, ha, yn, zc, zh, zj), the performances of participants show a monotonic decreasing curve. As discussed previously, it was assumed that the behaviour of participants would switch to the anticipatory mode as the speed of target increases. The monotonic decreasing indicates that the participant performance was only related to the difficulty of the trial, which is the target speed, and not affected by any other factor. Therefore participants belonging to this type did not exhibit anticipatory behaviour in the tracking trials. The other type of participants, whose performances were not monotonically decreasing, however, had other factors involving in their behaviour. As shown in the figures, some participants (Participant ID = gj, lh, lz, oz, sx, wa) had increased average phase difference when target speed went from 0.5Hz to 1Hz, which may imply that anticipatory control mode was activated in the high target speed trial although the anticipation was weak. It seems that participants were using a combined control mechanism, where passive feedback control mode and anticipatory mode effected alternately. When the participant switched to anticipatory behaviour mode, the phase difference had a larger probability to be positive, which would compensate for the increasing difficulty of the task. In order to demonstrate stronger anticipatory behaviour in the experiment, the fol-
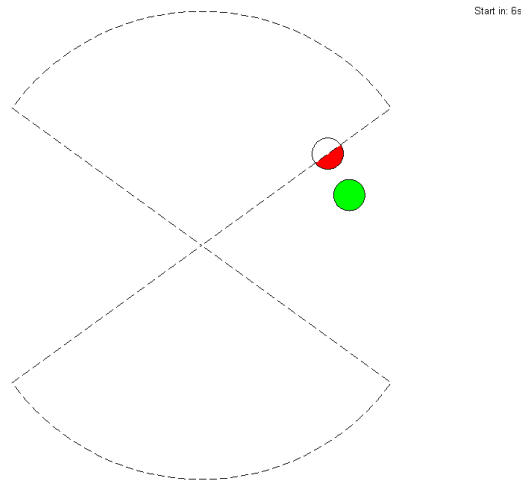
Figure 3.7: Screenshot of the refined experimental paradigm. The red circle is the target, while the green circle is the cursor controlled by the participant. Two dash sectors are the target-invisible zone. In the real experiment, there is no dash boundary, so the target-invisible part can not be seen.

lowing sections will explore different factors which could affect participant's behaviour mode, and experiment paradigm was refined.

3.3 Intermittent tracking paradigm

As participants did not show strong anticipatory behaviour in the previous experiment, the refined experiment paradigm was designed in order induce stronger evidence of anticipation. Several refinement were applied.

3.3.1 Method refinements

3.3.1.1 Changing the visibility of target

In the work of Hayashi [90], two target-invisible zones were added to the work, which made the behaviour of participants more anticipatory. In that

work, the phase difference distribution inside the target-invisible zone was positive-biased, which suggests that anticipatory behaviour was shown in this paradigm. In this research, the same target-invisible zone was applied in the refined paradigm. Two sectors, whose angles were both 0.6π, were horizontally symmetrically placed with each other. Their boundaries are shown as dash line in Figure 3.7. However, their boundaries were invisible in the actual experiment, so the two sectors were indistinguishable from the background. Inside the two sectors, the target was hidden behind the sectors so that it became invisible, while the tracer was not affected by these two sector regions. The target and tracer moved in the same rule as in the full visibility tracking trials. By introducing the target-invisible zone, it was expected that stronger anticipatory behaviour could be observed in the target-invisible zone. As the target was invisible, participants were forced to predict the position of the target in order to synchronise with it.

3.3.1.2 Introducing training session

The training effect of the tracking task was observed from the previous experiment. The performances of individual tracking trials showed improvements with time, even in the high target-speed trial. It implies that participants became more skillful on anticipatory behaviour through training. In order to get stronger anticipatory behaviour, 3 training sessions were introduced, which included 12 trials for each speed, 36 trials in total. The training sessions were exactly identical as the formal tracking trials.

3.3.1.3 Increasing the target speed

According to the work of Ishida [23], the anticipatory behaviour of participant becomes stronger when the speed of target increases. However, extreme high speed of target could be too difficult for humans to perform any accurate control. Therefore, it is necessary to explore the effect of target speed in the refined paradigm. Two sets of speed were tested, which were (0.1, 0.6, 1.1)Hz and (0.1, 0.7, 1.3)Hz. Experiments of both sets of speed were performed. It was found that most of the participants who had the (0.1, 0.7, 1.3) set failed to show anticipatory behaviour (5 out of 7), and showed a decreasing of the average phase difference in the high speed (6 out of 7). For the other set of speed, (0.1, 0.6, 1.1), however, all the participants showed anticipatory behaviour (6 out of 6), and the average phase difference of the most of participants were monotonically increasing as the function of the speed of target (5 out of 6). These results indicate that the reaction limit of participants lays between 1.1Hz and 1.3Hz. At that critical speed, the ability to perform anticipatory behaviour of humans reaches the peak, and the human anticipation mechanism is fully activated.

3.3.2 Results of refined behavioural experiment

The behavioural data of the 6 participants who performed the intermittent tracking trial with speed (0.1, 0.6, 1.1) were analysed. All of the participants received 3 training sessions, totally 12 trials for each speed before the formal session. Their overall averaged phase difference curve is shown in Figure 3.8, while the results of individual participants are shown in Figure 3.9.

From the averaged participants mean phase difference in Figure 3.8,
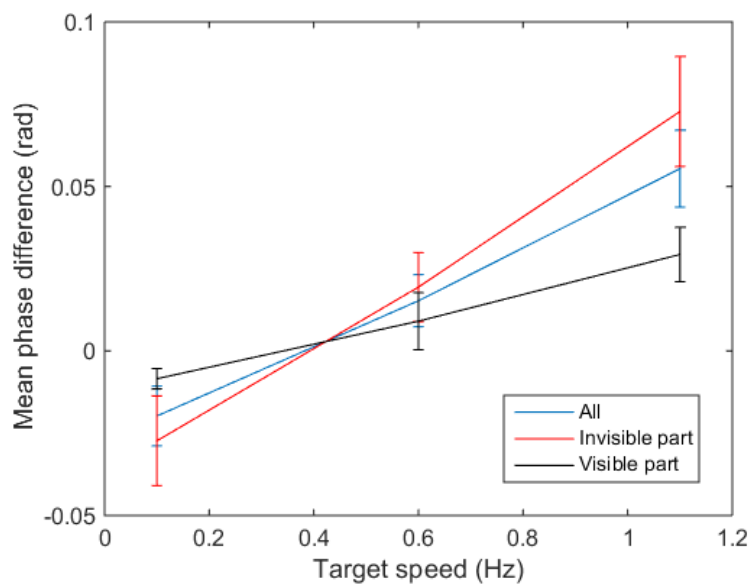
Figure 3.8: The averaged participants mean phase difference of the intermittent tracking trials from all the participants. Each error bar represents the standard error of the mean value. It is clear that the result shows an increasing tendency, and the high speed trials show significant positive average phase difference (t-test, $p < 0.05$), which suggests the anticipation behaviour.

it can be found that the mean phase differences of the whole trial (blue curve) of the high speed trials is significantly large than 0 (t-test, $p < 0.05$), which indicates that participants showed significant anticipatory behaviour in those trials. The curve of the mean phase differences of the whole trial (blue curve) also shows an increasing tendency of the participants performances in the intermittent tracking trials, which indicates that the anticipatory behavioural mode of participants has overcome the increasing level of difficulty.

The performances of individual participants in Figure 3.9 show similar picture as the overall result. Most of the participants showed a significant anticipatory mode in the high speed trials (t-test, $p < 0.05$), and the monotonic increasing average phase difference curve (5 out of 6). The phase difference data of the target-invisible zone and the target-visible zone were presented separately. It was found that participants showed stronger anticipatory behaviour in target-invisible zone than in target-visible zone in the high speed trial, as the average phase difference of target-invisible zone was usually higher than that in target-visible zone. In order to investigate this phenomenon in a further step, the phase difference distribution of target-visible zone and target-invisible have been plotted as Figure 3.10.

It was reported that the distribution of phase difference follows a Gaussian distribution by previous works [23, 12]. In the results, it can be observed that the distributions of phase difference fit into the Gaussian distribution shape. It can also be found that the distribution of target-invisible zone is less symmetric than the target-visible zone, especially for the case of high speed. This positive-biased distribution is the characteristic of the anticipatory behaviour, which suggests that intermittent tracking experiment
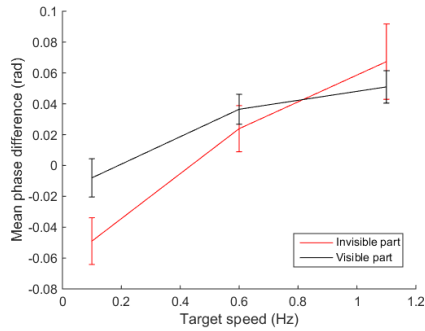
(a) Participant ID = bh
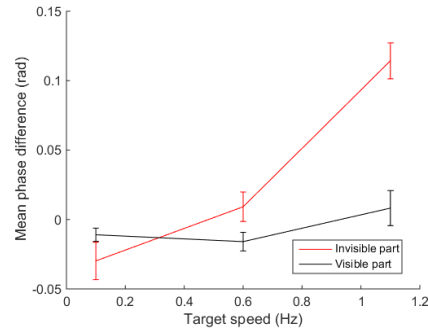
(b) Participant ID = cj
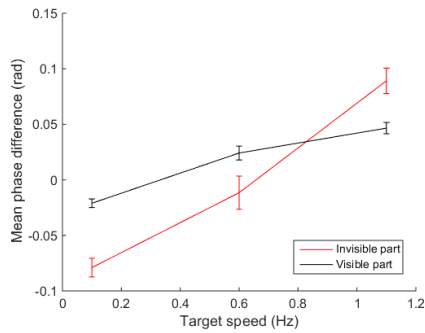
(c) Participant ID = ca
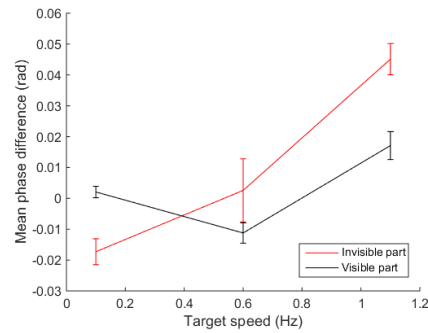
(d) Participant ID = hc
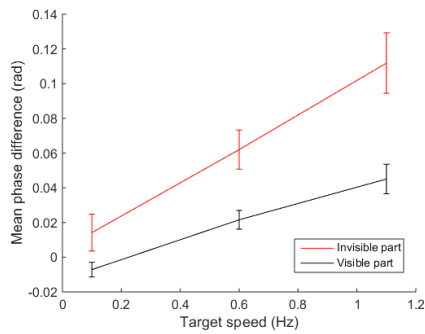
(e) Participant ID = sf
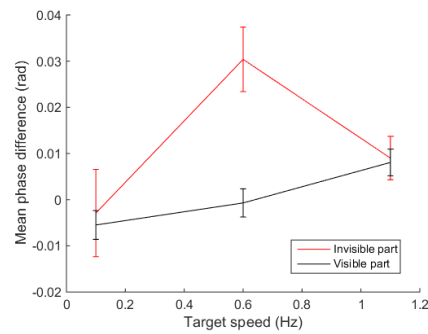
(f) Participant ID = ag

Figure 3.9: The averaged phase difference of individual participants in the intermittent tracking trials. Each participant had 20 trials for each target speed. Each error bar represents the standard error of the mean value. Most of the participants (5 out of 6) show the significant positive average phase difference in the high speed trials (t-test, $p < 0.05$), which suggests the anticipatory behaviours were demonstrated in those trials. For the clearance of display, the average phase difference of the whole trial (the blue curve in Figure 3.8) are not presented.
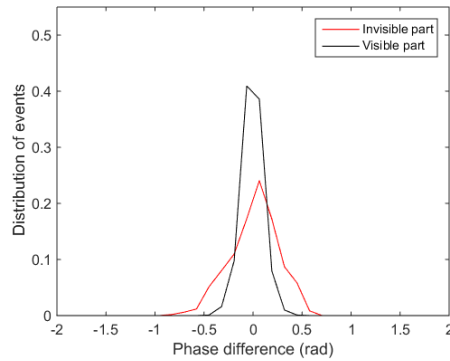
(a) Phase difference distribution (0.1Hz)
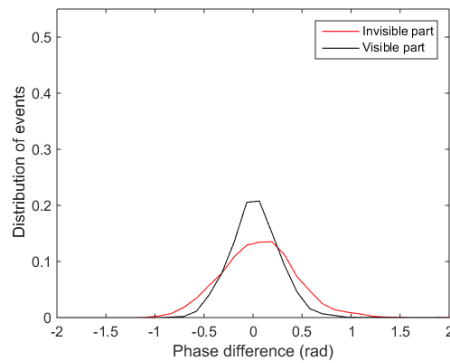
(b) Phase difference distribution (0.5Hz)
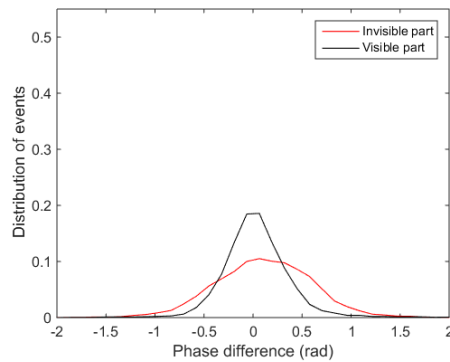
(c) Phase difference distribution (1.0Hz)

Figure 3.10: Phase difference distributions in target-visible part and in target-invisible part are shown separately in this figure. Subfigure (a), (b), and (c) show the distributions of each target speed, respectively. The distributions of one participant are shown here as an example (Participant ID = sf), but all the participants share the same tendency. It is clear that the phase difference distribution in target-invisible part is less symmetric than that in target-visible. The positive-biased distribution of target-invisible part indicates that participant performed anticipatory behaviour in this region.

did successfully stimulate the anticipatory behaviour of humans.

3.3.3 Discussion on refined behavioural experiment

From Figure 3.8, it can be found that participants exhibited anticipatory behaviour in the intermittent tracking paradigm. Remarkably, the average phase differences of the target-visible zone and the target-invisible zone in the high speed trials were significantly different from each other, which indicates two distinctive control modes of the motion. From Figure 3.10 it can be further learnt that participants performed very obvious anticipatory behaviour in the target-invisible zone, which is the main reason that participants had the overall positive average phase difference. The fact that different participant behaviour patterns corresponded to different target visibility regions may imply the transitions between different visual-motor control modes [90].

In the tracking task, it is very essential for brain to acquire kinetic information of the target, including both position and velocity. In the full visibility tracking trials, and the target-visible zone of the intermittent tracking trials, the kinetic information of the target could be easily acquired through visual input from the screen. However, with this visual information of the target, participant would only passively follow the target through a feedback control. The average phase difference between the tracer and the target would very likely be negative with this feedback control, because the visual perception takes time, and there will always be a time delay between the actual phase difference and the phase difference perceived as the visual feedback by the brain. When the visual information acquisition from the target was impeded in the target-invisible zone,

the other mode of visual-motor control, the anticipatory mode [23, 91, 92], becomes dominant. Without the access to the actual visual information of the target, participants were forced to estimate the position of the target, which made the control mechanism transform from the feedback control to the feedforward control. In this case, the time delay between the controller and the realtime input vanished, so participant was able to not only compensate the phase difference but also anticipate the position of target.

Observing the distinctive behaviour modes in the two zones, it can be learnt that participants kept transiting between these two control modes in the intermittent tracking trials. While it indicates that participants were forced to use the anticipatory mode control in the target-invisible zone, it also indicates that the anticipatory mode would become weak and give place to visual feedback mode again in the target-visible zone. It may imply that the inner prediction model of the target kinetics is contradicted with the direct visual input of the target kinetic information. This hypothesis will be further studied in future work.

While participants performed distinctive behaviour modes in the two difference zones, it is worth to note that the overall performance of participant in the intermittent tracking trial can not be seen as a simple sum up of the performances in the visible and invisible zone. The movement of the participant in the intermittent tracking trial is a continuous process with the changing visibility of the target. In the 1Hz trials, the target changed visibility every $0.2 \sim 0.3$ seconds. This rapid change of the target visibility is also an essential part of the paradigm, which could contribute to the participants' performances. In future work, the two target invisible zones of the intermittent tracking trial can be separated into four, and then the

overall performance will be compared with the results above, which would tell whether the change itself plays a role in the participants' behaviour.

These two different behaviour modes could also affect each other. It can be found that participants showed different performance in the target-visible zone of intermittent tracking trials and in the full visibility tracking trials. In the target-visible zone of intermittent tracking trials, participants showed significant anticipatory behaviour. From Figure 3.9, it can be observed that most of the participants (5 out of 6) showed positive average phase differences in the high target speed trial, and monotonic increasing curves of the average phase difference in the target-visible zone. Participants of full visibility tracking paradigm, however, did not show strong anticipatory behaviour even though the visibility of target was the same as previous case (Figure 3.4~3.6). It implies that the target-invisible zone did not just affect the participant's behaviour inside it but also affect the participant's behaviour outside it. In order to explain this phenomenon, consider the human anticipation in a more general sense. People will not perform anticipatory behaviour if the kinetics of the target is constant, because once the motion is synchronised with the target, no control is needed any more but passively keeping the velocity of the movement. Therefore, in order to make people have some variants to anticipate, the movement state of the target must change over time. In the full visibility tracking trials, the direction of target's velocity kept changing during the trials. In the intermittent tracking trials, the visibility of the target introduced another layer of the variability of the target movement, which is the change of the accessability of the target movement information. And the introduction of this extra layer of variability induced a quite strong anticipatory

behaviour. The different performances of these two tracking tasks with the same target visibility imply that more variability of the target movement would result in stronger anticipatory behaviour. Here the variability can be both changes of the target movement itself or changes of the accessability of the target movement information. In future work, more experiments will be performed to collect the evidences for this argument.

From Figure 3.8, it can be also observed that the average phase difference increased with the speed of target. Studies have shown that higher speed of target results in stronger anticipatory motion [23, 90]. This trend was clearly observed in the intermittent tracking trials in this study. The full visibility tracking trials also exhibit this trend for some degrees, although large participant variance made this trend hard to be observed.

From Figure 3.9, it can be observed that the participant variance was still large in the intermittent tracking paradigm. In the full visibility tracking experiment, there were anticipators as well as followers, which may suggest that some participants utilized the anticipatory control mode even with the full access to the visual information of target. It can be also found in Figure 3.9(f), that the participant did not show a monotonic curve for the average phase difference in the target-invisible zone. It may indicate that the high speed, 1.1Hz, is too difficult for that participant. But regardless of that, that participant still had positive average phase difference at the high speed level, which suggests that the participant still showed anticipatory behaviour.

3.4 Conclusion

In this chapter, the anticipatory behaviour of humans was investigated with the tracking paradigm. The full visibility tracking trials did not exhibit strong anticipatory behaviour in the performances of participants. In order to better demonstrate the anticipatory behaviour, intermittent tracking trials were performed, which showed strong anticipatory behaviour. In the intermittent tracking trials, two distinctive control modes of visual-motor coordination were found in the target-visible zone and target-invisible zone, respectively. In the target-visible zone, participants depended on visual feedback to control their motion, while in the target-invisible zone, participants performed anticipatory control mode behaviour. It was found that the control mode of participant behaviour would switch between the visual-feedback mode and the anticipatory mode in the intermittent tracking trials. In this research, it was also confirmed that higher target speed would result in stronger anticipatory behaviour in tracking paradigm.

Chapter 4

Eigenvector-based Dynamical Analysis Method

Contents

4.1 Introduction

Brain network is a fast-changing system within the scale of millisecond, which makes it essential to understand the transient details of the network. In order to extract the dynamical properties of the functional connectivity, an eigenvector-based dynamics analysis method was developed and tested with simulated synchrony network in this project. This chapter first describes the model simulating the phase synchrony network evolution, and then describes the dynamical analysis method. After that, the dynamical analysis method is applied on the simulated network, and the results are discussed.

The eigenspectrum is the set of all the eigenvectors and corresponding eigenvalues of the adjacency matrix or Laplacian matrix of the network, which has been extensively studied in the area of network theory [93]. The adjacent matrix of an undirected network is a self-adjoint matrix, as such it can be reconstructed from the eigenspectrum. The eigenspectrum carries all the information of the network. The relevance of an eigenvector is determined by its corresponding eigenvalue. The eigenvector corresponding to the biggest eigenvalue, which is called prime eigenvector, carries most information about the adjacency matrix, which makes it an ideal representation of the network. In this work, by replacing the adjacent matrix of each time snapshot with the corresponding prime eigenvector, the evolution of the network was represented with a reduced dimensionality.

The works described in this chapter are useful tools which are not only useful in the context of neural signal analysis but also can be applied to the

analysis of any other dynamical networks. The simulation model of synchrony network can be extended and modified to simulate networks with different properties. The eigenvector-based dynamical network analysis method provides an insight of the network evolution, which demonstrated a great potential to reveal the potential meta-stable states of the network dynamics. Chapter 6 will demonstrate the results of EEG dynamical functional connectivity with this method applied, which show a meta-stable state structure of the EEG functional connectivity network.

Time	t
Phase	$\phi_{m,t}$
Angular speed	ω
Instantaneous eigenvector	$\overrightarrow{\Phi}(t)$
Correlation matrix	C
Eigenvector of the correlation matrix	u_1, u_2, u_3
Row vector of the time window	v_m, v_n
Eigenvector of the refined adjacency matrix	$\overrightarrow{\Upsilon}(t)$

Table 4.1: The notations used in this chapter.

4.2 Simulated synchrony network model

In this work, a synchrony network simulating model was constructed with auto-regression (AR) model. Before simulating a complex phase synchrony network, let us first start with generating a simple sinusoidal signal with the AR model.

4.2.1 Generating synchronized time series

Assume an oscillator described by the exponent $e^{i(\omega t + \phi_0)}$, where ω is the angular speed and ϕ_0 is the initial phase of the oscillator. Defining the

phase variable

$$\phi_t = \omega t + \phi_0 \tag{4.1}$$

then we arrive at $e^{i\phi_t}$. ϕ_t is a linear function of time t, which makes it an ideal variable for auto regression. Assuming the time step stays the same during the whole time series, then:

$$e^{i\phi_{t+1}} = e^{i[(\phi_t - \phi_{t-1}) + \phi_t]} \tag{4.2}$$

from which an auto-regression relation of phase can be found. Therefore when a simple sinusoidal oscillator is standing alone, its phase time series can be generated by Equation (4.2).

When this oscillator n starts to synchronise with another oscillator m, the phase of oscillator m will start to affect the phase of oscillator n and a coupling term will be added to the auto regression equation. Eventually, the two oscillators will reach a synchronisation state. This study specifically focused on the phase-locking synchronization which is defined as a state for which the phase difference of two signals keeps the same for a certain time period [34]. Thus

$$\phi_{m,t_1} - \phi_{n,t_1} = \phi_{m,t_2} - \phi_{n,t_2} \tag{4.3}$$

Therefore, the coupling interaction can be defined to be proportional to the increment of phase difference:

$$a_{mn}[(\phi_{m,t} - \phi_{n,t}) - (\phi_{m,t-1} - \phi_{n,t-1})] \tag{4.4}$$

which is the coupling term acting on the oscillator n from m, and a is a coupling strength factor. Remarkably, the above equation can be rewrite

as

$$a_{mn}[(\phi_{m,t} - \phi_{m,t-1}) - (\phi_{n,t} - \phi_{n,t-1})] \tag{4.5}$$

or

$$a_{mn}(\delta\phi_{m,t} - \delta\phi_{n,t}) \tag{4.6}$$

where the $\delta\phi_{m,t}$ indicates the the phase increment of the oscillator m at time t. This form suggests another definition of the phase-locking synchrony, which is that the two oscillators have the same phase increment or the angular speed. This definition will be mentioned again in the following discussion. As a result, when two oscillators m and n interact with each other and proceed to a phase-locking state, the phase autoregressive equation of oscillator n becomes

$$\phi_{n,t+1} = [(\phi_{n,t} - \phi_{n,t-1}) + \phi_{n,t}] + a_{mn}[(\phi_{m,t} - \phi_{n,t}) - (\phi_{m,t-1} - \phi_{n,t-1})] \tag{4.7}$$

and its complex exponential form is

$$e^{i\phi_{n,t+1}} = e^{i[(\phi_{n,t} - \phi_{n,t-1}) + \phi_{n,t}] + ia_{mn}[(\phi_{m,t} - \phi_{n,t}) - (\phi_{m,t-1} - \phi_{n,t-1})]} \tag{4.8}$$

People may notice that Equation 4.7 has a form of the variational equation. However, this similarity is superficial, because ϕ_m and ϕ_n do not necessarily satisfy the inequality $\sup |\phi_{m,t} - \phi_{n,t}| < \delta$, which is a prior assumption of the variational equation.

This method is a very intuitive way to generate the pseudo data and only simple elements are considered. Other possible effects, such as the delay of the coupling, were not considered in this method. Nevertheless, this simulation setup would be good enough for testing our dynamical analysis

method. One well-known phase synchronization model is Kuramoto model [94], which is a non-linear model that describes the behaviour of a large group coupling oscillators. However, the nonlinearity of this model create extra difficulty to generate time series comparing to a linear coupling model. Remarkably, the coupling strength factor a can be defined as a matrix A, where each of its entry a_{mn} is the coupling strength acting on n from m. This way of definition provides more flexibility, which allows the coupling strength to be different for each oscillator pair, and the coupling can be asymmetric, which is $a_{mn} \neq a_{nm}$.

4.2.2 Generating small synchrony networks

The above simulation method was tested in two steps. First, a simple coupling oscillator pair were generated with this model, then the simulation model were used to generate a larger complex network with multiple clusters .

4.2.2.1 Two oscillators coupling

The proposed coupling was first examined on a simple case. In order to do that, two oscillators were defined, and a 3-second time series with 1kHz sampling rate was generated for each of them. They would be phase-locked with each other during $1 \sim 2$ second, and acted independently for the rest of the time. Their coupling strength was set to be symmetric for these two oscillators in this case. The following figures only show the real part of the complex exponential, which is the cosine wave of the phase.

From Figure 4.1, it can be found that the phase-locking was taking place between the 1st second and the 2nd second, and then the phase-locking
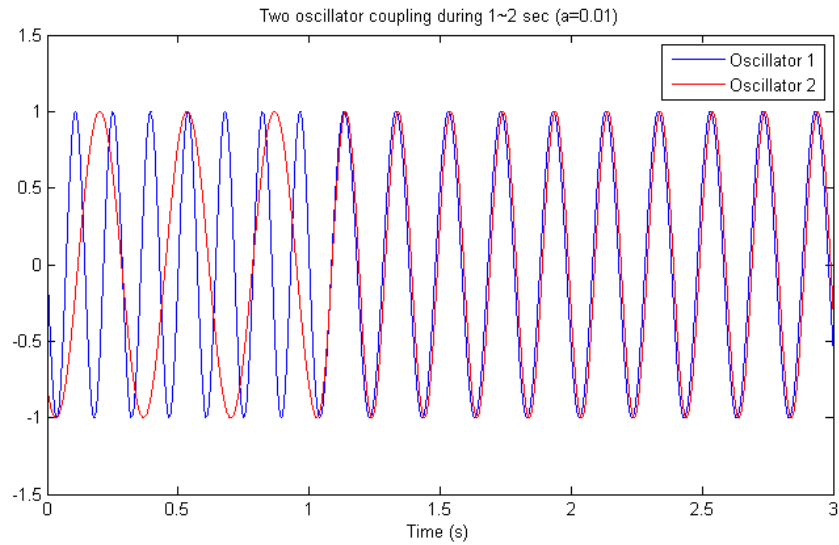
(a) Time series plot
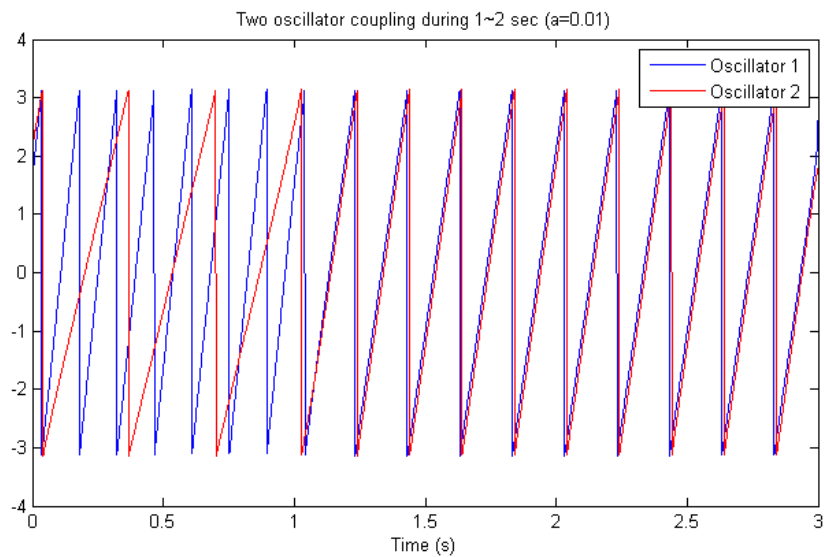
(b) Phase plot

Figure 4.1: The time series of two oscillators coupling between the 1st and 2nd second. Subgraph (a) shows the time series of the oscillator while subgraph (b) shows the phase of the oscillator. The initial frequency is 7Hz for oscillator 1 , and 3Hz for oscillator 2. The coupling strength a is 1 for both of them. It is clear that they became phase-locked with each other between the 1st and 2nd second, and then coupling kept on even after the 2nd second when the coupling force disappears.

kept going on even after 2 seconds. The reason for the everlasting phase-locking is that there was no spontaneous force to break this coupling in this buildup, so that the oscillator cannot get rid of phase-locking without outside interference. Figure 4.1(b) shows that both of the oscillators have transferred to a new frequency when phase-locking happened, which is a frequency between 3Hz and 7Hz. This result proves that this buildup can properly generate phase-locking time series.

The effect of the coupling strength was also explored, and a particular interesting case when $a = 1$ is discussed here. In Figure 4.2, the coupling strength a has been tuned to 1 from 0.01, then the performance of simulated oscillators was different from Figure 4.1. After 2 seconds, the two oscillators somehow managed to decouple with each other. This phenomenon only happens in the particular case when $a = 1$. When $0 < a < 1$, the two oscillators cannot decouple; when $a > 1$, the system becomes unpredictable because of the over-feedback.

To understand this phenomenon, revisit the auto regression equation. Rearrange Equation (4.7):

$$\phi_{n,t+1} - \phi_{n,t} = (\phi_{n,t} - \phi_{n,t-1}) + a\left[(\phi_{m,t} - \phi_{m,t-1}) - (\phi_{n,t} - \phi_{n,t-1})\right]$$

$$\phi_{n,t+1} - \phi_{n,t} = (1-a)(\phi_{n,t} - \phi_{n,t-1}) + a(\phi_{m,t} - \phi_{m,t-1}) \qquad (4.9)$$

$$\delta\phi_{n,t+1} = (1-a)\delta\phi_{n,t} + a\delta\phi_{m,t}$$

From Equation (4.9), it can be found that the coupling strength factor a actually acts as a weight to combine the intrinsic and extrinsic phase increment (or angular speed). When $a = 1$, Equation (4.9) can be reduced to

$$\phi_{n,t+1} - \phi_{n,t} = \phi_{m,t} - \phi_{m,t-1} \qquad (4.10)$$
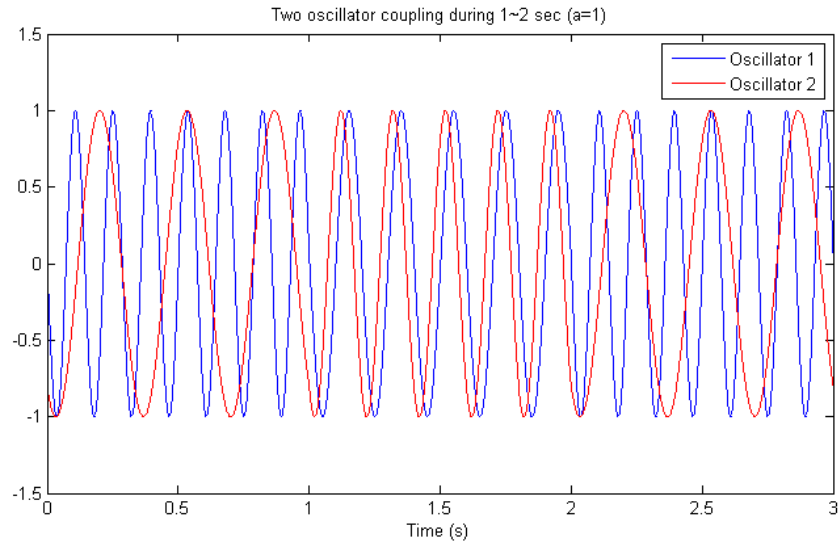
(a) Time series plot
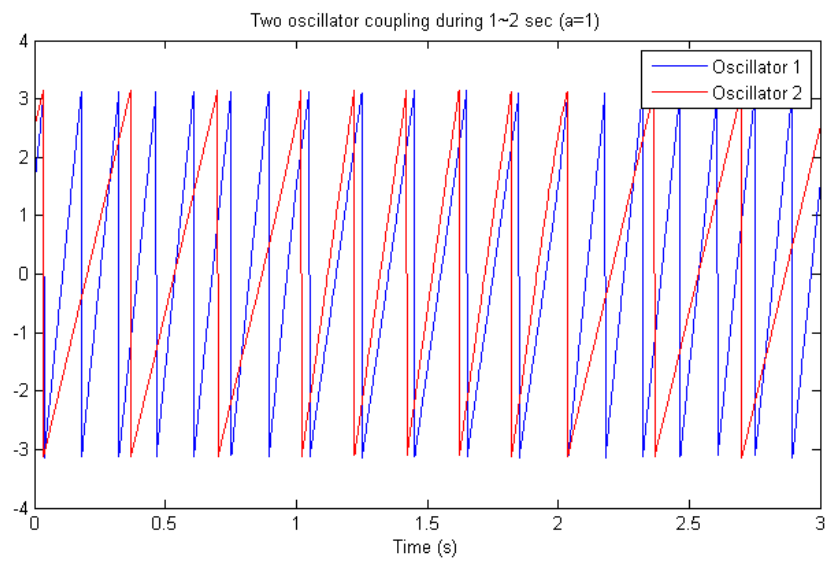
(b) Phase plot

Figure 4.2: Changing the coupling strength a that used to produce Figure 1 from 0.01 to 1 makes the two oscillators get rid of the phase-locking state. Subgraph (a) shows the time series of the oscillator while subgraph (b) shows the phase of the oscillator.
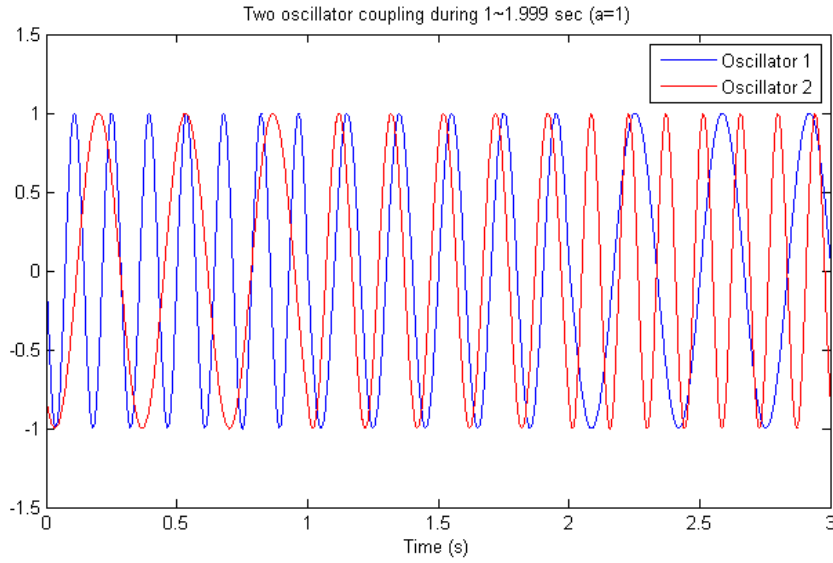
Figure 4.3: When the coupling time is 1-sample-point shorter, a switch of frequency between these two oscillators can be observed.

or it can be written as following:

$$\phi_{n,t+1} = \phi_{n,t} + \delta\phi_{m,t} \tag{4.11}$$

From this equations it can be concluded that, when $a = 1$, the two oscillators keep exchanging their angular speed, which creates a "fake" phase-locking because the "average speed" of them are the same but they are not phase-locked in each and every sample point. Then they stop exchanging the angular speed when the coupling disappears. If the coupling period is one-step shorter, a switch of frequency between the two oscillators should be observed. Figure 4.3 shows that the predication is correct. This exploration suggests that the effective range of coupling strength factor a should be $a \in [0, 1)$.

4.2.2.2   Complex network

With the knowledge learned from the two-oscillator case, the method was then used to simulate a larger network with cluster structure embedded. The simulated network consisted of three clusters, each cluster was a connected graph. Different clusters were connected by sparse connections if they were set to be coupled, otherwise they would be isolated from each other. For one cluster, the members were first connected together as a chain, in order to make sure that the cluster was a connected sub-network. Then all the rest potential edges within this cluster were included with a probability p_1. For the coupling between two clusters, all the potential inter-cluster edges were included with a probability p_2, and $p_1 > p_2$. The connections were symmetric and unweighted. During the whole simulation, the members within the same cluster kept phase-locked with each other. The evolution of clusters coupling is shown in Figure 4.4: In the 1st second, none of the cluster are coupled; In the 2nd second, Cluster 1 and 2 are coupled with each other; Finally in the 3rd second, Cluster 2 and 3 are coupled. The total length of the simulated time series was 3 seconds. The numbers of oscillators in each cluster were arbitrarily chosen. Cluster 1 includes 3 oscillators, cluster 2 includes 5 oscillators, while cluster 3 includes 7 oscillators. The initial frequency of the 3 clusters were 3Hz, 17Hz, and 7Hz, respectively. The initial phase for each oscillator was generated randomly.

The temporal evolution of oscillators are represented with the angular speed time series, which is shown in Figure 4.5. The clusters acted as expected: Cluster 1 and 2 synchronised from time point 1000 ms to 2000 ms, and Cluster 2 and 3 synchronised from time point 2000 ms to 3000 ms.
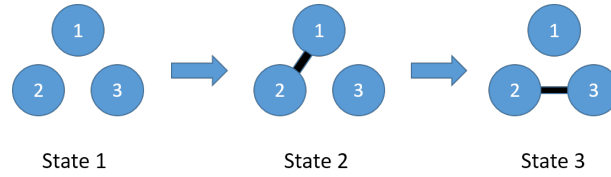
Figure 4.4: The pre-defined meta-stable state transition. Each circle stands for a cluster, and the black bar between the circles stands for the coupling correlation. There are 3 meta-stable states, and each of them lasts for 1 second, which makes a 3-second time series with 3 channels. The order of states in this figure is identical with the time order of the states in the time series.

Figure 4.6 shows the cosine signals of two oscillators from Cluster 1 and 2, respectively, and it can be observed that the two oscillator started to synchronise at 1000 and desynchronised at 2000.

The above simulation demonstrated that our simulation method is able to create the complex synchrony network with dynamical cluster structure embedded. In the next section, the eigenvector-based dynamical analysis will be introduced and then tested with the simulated time series.

4.3 Dynamical analysis method using prime eigenvector

This section describes a dynamical analysis method to recognise the meta-stable states of network evolution. This method will be tested on the simulated phase-synchrony networks in the next section. First, let us visit the instantaneous phase difference. By construction, the instantaneous phase differences have the following relation:

$$\Delta\phi_{13} = \Delta\phi_{12} + \Delta\phi_{23} \tag{4.12}$$
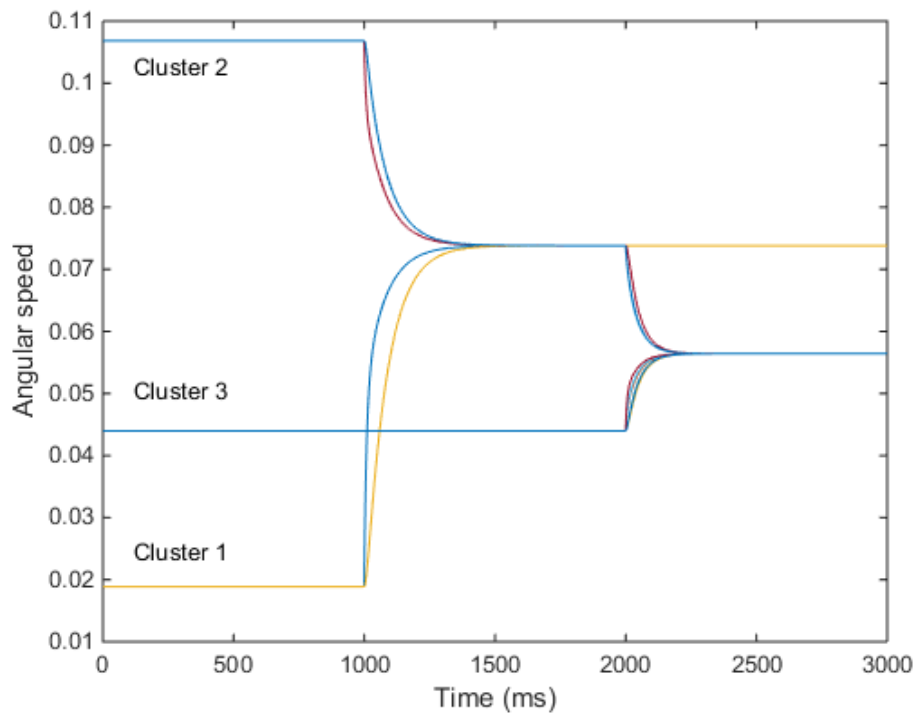
Figure 4.5: The angular speed evolution of the network. The network initiated with 3 clusters of different frequencies. Cluster 1 started to couple with Cluster 2 at time point 1000 ms and finally they merged together. At time point 2000 ms, Cluster 2 and Cluster 3 started to synchronise with each other. It can be observed that Cluster 2 decoupled with Cluster 1 and merged with Cluster 3.
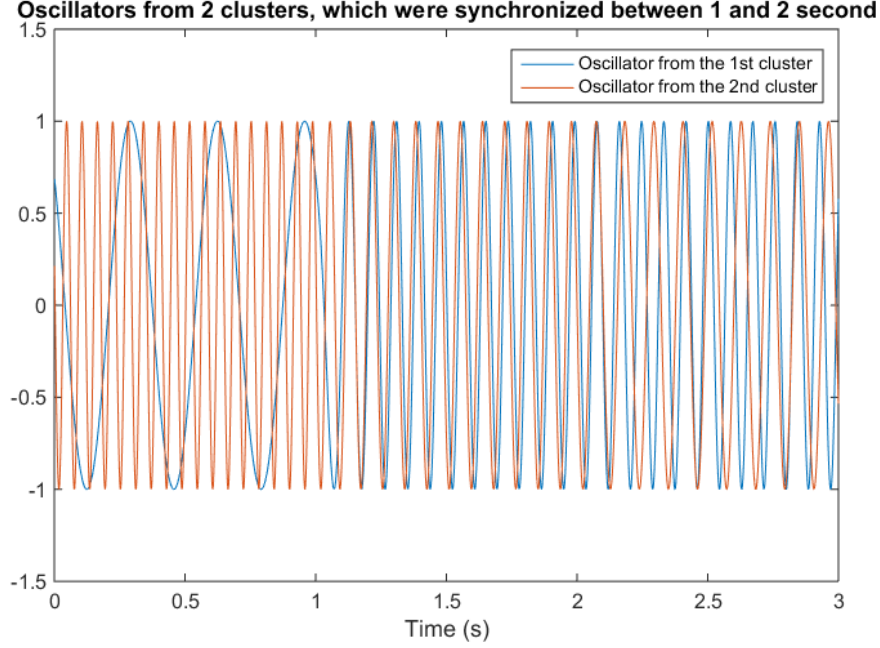
Figure 4.6: Two oscillators selected from the Cluster 1 and 2 respectively. It can be seen that the two oscillators were coupled between the 1st and 2nd second, which matches the states setting shown in Figure 4.4.

This property implies that the instantaneous phase adjacency matrix, whose entries are phase differences in complex form, only have one non-zero (real) eigenvalue with its corresponding eigenvector, which can be easily proved through Gaussian elimination. In fact, considering the fact that self-adjoint matrix can be written as the sum of eigenvector products weighted by the corresponding eigenvalue, the instantaneous phase adjacency matrix can be written as the product of its only eigenvector:

$$
\begin{bmatrix}
1 & e^{i\Delta\phi_{12}} & \cdots & e^{i\Delta\phi_{1n}} \\
e^{i\Delta\phi_{21}} & 1 & \cdots & e^{i\Delta\phi_{2n}} \\
\vdots & \vdots & \ddots & \vdots \\
e^{i\Delta\phi_{n1}} & e^{i\Delta\phi_{n2}} & \cdots & 1
\end{bmatrix}
=
\begin{bmatrix}
e^{i\phi_1} \\
e^{i\phi_2} \\
\vdots \\
e^{i\phi_n}
\end{bmatrix}
\begin{bmatrix}
e^{-i\phi_1} & e^{-i\phi_2} & \cdots & e^{-i\phi_n}
\end{bmatrix}
\quad (4.13)
$$

The eigenvector associated with the largest eigenvalue is called the prime eigenvector $\overrightarrow{\Phi}(t)$, where t in bracket indicates the corresponding time index of the time series. Then the above equation can be written as

$$
\begin{bmatrix}
1 & e^{i\Delta\phi_{12}} & \cdots & e^{i\Delta\phi_{1n}} \\
e^{i\Delta\phi_{21}} & 1 & \cdots & e^{i\Delta\phi_{2n}} \\
\vdots & \vdots & \ddots & \vdots \\
e^{i\Delta\phi_{n1}} & e^{i\Delta\phi_{n2}} & \cdots & 1
\end{bmatrix} = \overrightarrow{\Phi}\,\overrightarrow{\Phi}^{H} \tag{4.14}
$$

where $\overrightarrow{\Phi}^{H}$ is the conjugate transpose of $\overrightarrow{\Phi}$. It can be conjectured that the evolution of $\overrightarrow{\Phi}(t)$ in time represents a trajectory in a N-dimensional (probably noisy) dynamical system with a set of at least M attractors given by the stable phase vectors $\overrightarrow{\Phi}^{1}$, $\overrightarrow{\Phi}^{2}$, ..., $\overrightarrow{\Phi}^{M}$, to be found experimentally. It can be also assumed that each attractor would correspond to an eigenvector of an underlying structural connectivity matrix S. With a large enough set of such eigenvectors, and estimating the corresponding eigenvalues by dwell time, thus S could be approximately reconstructed. For this picture to be true, even approximately, the system must display a number of testable features:

- The system must spend most of its time close to one of the attractors. Thus, the inner product $\langle \overrightarrow{\Phi}(t), \overrightarrow{\Phi}(t+1)\rangle \simeq 1$

- Occasionally the system will undergo longer excursions away from the attractor, possibly moving into another attractor's basin. For a brief while, self-correlation will decrease $\langle \overrightarrow{\Phi}(t), \overrightarrow{\Phi}(t+1)\rangle \ll 1$

- In the latter case it will quickly return to the proximity of (the same, or another) attractor.

Therefore, in the following analysis on simulations, the inner-products between prime eigenvectors would be investigated. It is expected to be observed that high plateaus separated by sharp decreases on the time series of successive inner-product time series $\langle \overrightarrow{\Phi}(t), \overrightarrow{\Phi}(t+1) \rangle$. Also the correlation matrix C is defined, whose entry $c_{ij} = \langle \overrightarrow{\Phi}(i), \overrightarrow{\Phi}(j) \rangle$, and expected to show block structure in the matrix, as the eigenvectors sharing the same meta-stable state would have high inner-product.

4.4   Results of simulated network model

Two simulations were setup for testing the eigenvector analysis method. In the first simulation, only 3 oscillators were included in the network. In the second one, the 3 oscillators were expanded into 3 synchronous clusters, which created a network with larger scale. The evolutional interaction between oscillators/clusters followed the demonstration of Figure 4.4, which was the same as the network simulated in the previous sections.

The successive eigenvectors inner product time series $\langle \overrightarrow{\Phi}(t), \overrightarrow{\Phi}(t+1) \rangle$ and correlation matrix C are shown in Figure 4.7 and 4.8, which however shows the patterns which are different from the expectations. In Figure 4.7(a), it can be observed that the structure of plateaus is separated by the sharp decreases. However, in the expectation, the decreases should correspond to the shift of oscillator synchrony states, therefore two decreases should happen at time point 1000 ms and 2000 ms, respectively. The decreases in Figure 4.7(a) looks randomly placed. In the larger network case (Figure 4.8(a)), inner-product keeps an extreme high value during almost the whole time series. Except about 20 points in the boundary (beginning

64
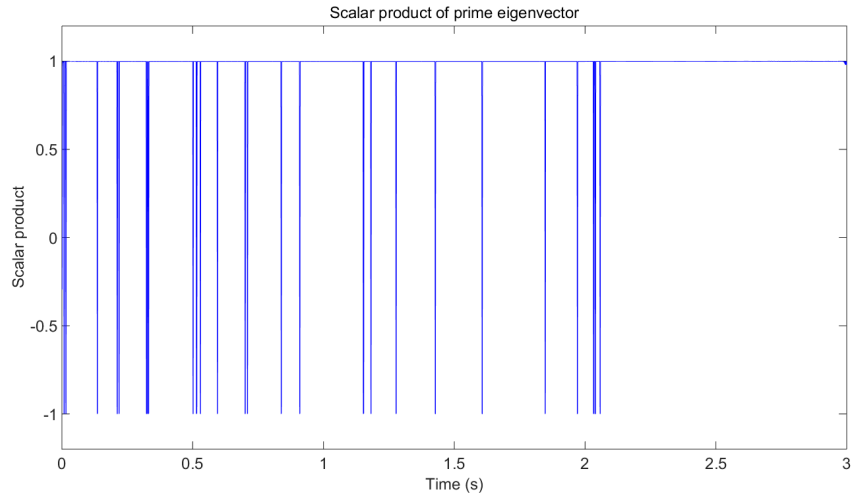
(a) Successive inner-product of 3-oscillator data
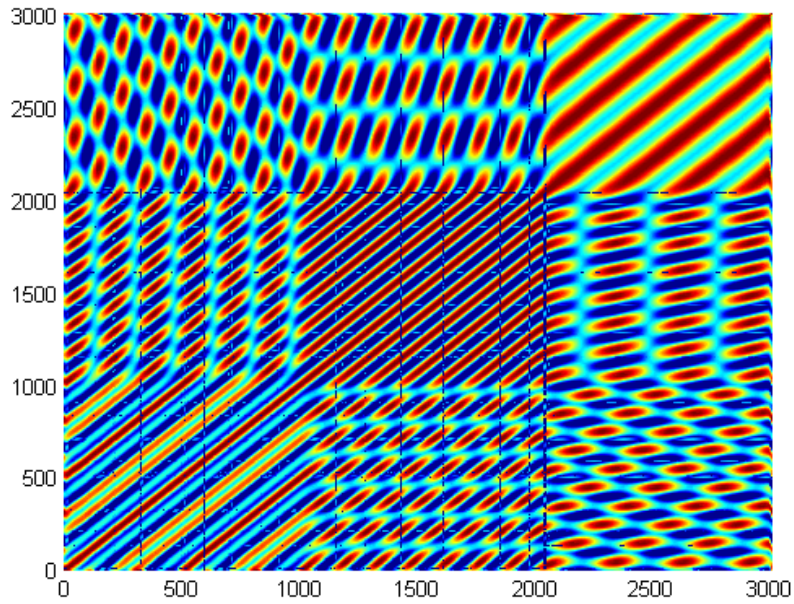
(b) Correlation matrix of 3-oscillator data

Figure 4.7: Subgraph (a) shows the inner-product time series of successive prime eigenvector, while subgraph (b) shows correlation matrix C of the 3-oscillator simulation data, whose entry $c_{ij} = \langle \overrightarrow{\Phi}(i), \overrightarrow{\Phi}(j) \rangle$. The index of the axis in subgraph (b) show the time in millisecond. Plateaus separated by sharp decreases can be observed in the time series of inner-product. However, the decreases don't correspond to the shift of oscillator synchrony states. The correlation matrix doesn't show the block structure as expected, alternatively shows a strip pattern.

65
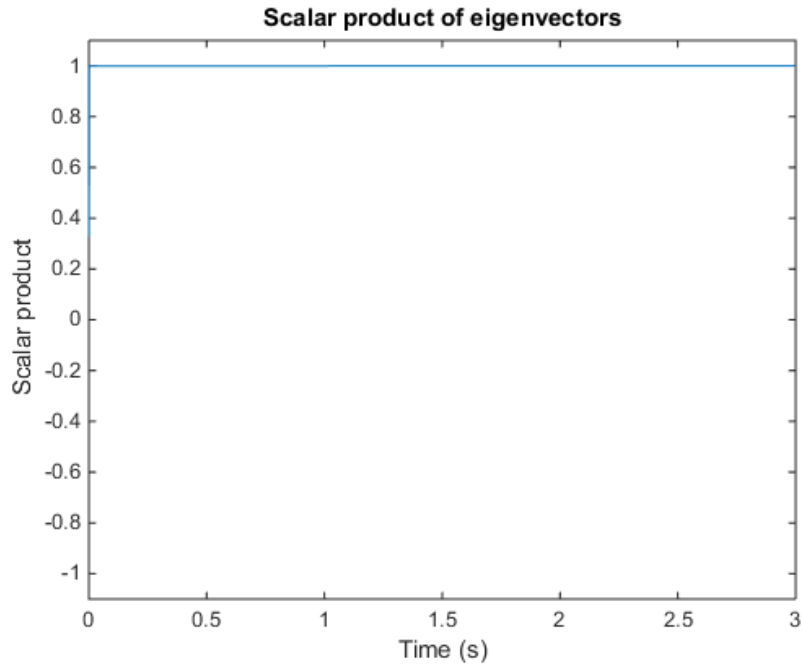
(a) Successive inner-product of 3-cluster data
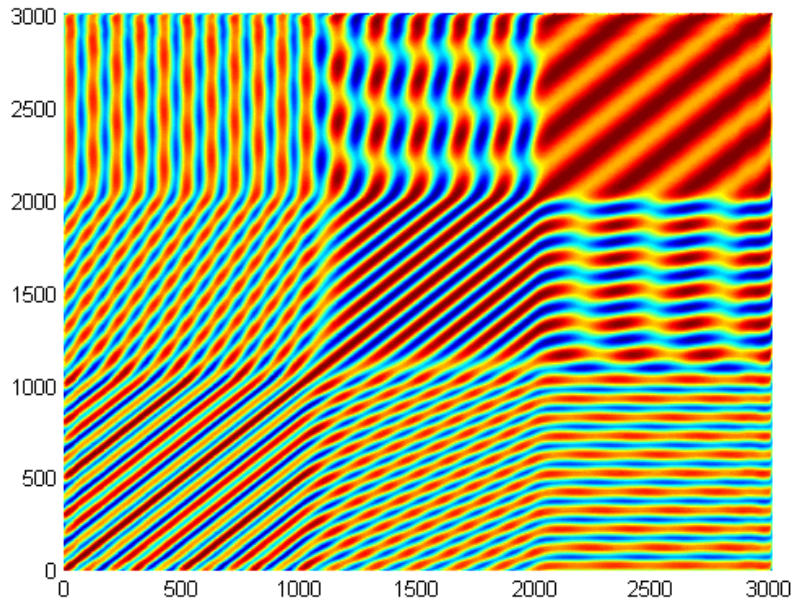
(b) Correlation matrix of 3-cluster data

Figure 4.8: Subgraph (a) shows the inner-product time series of successive prime eigenvector, while subgraph (b) shows correlation matrix C of the 3-oscillator simulation data, whose entry $c_{ij} = \langle \overrightarrow{\Phi}(i), \overrightarrow{\Phi}(j) \rangle$. The index of the axis in subgraph (b) show the time in millisecond. The time series of inner-product keeps a high value during almost the whole time series. Except about 20 points in the boundary (beginning and ending), all other points are > 0.99. The same stripe pattern as 3-oscillator case can be observed in the correlation matrix.

and ending), all other points in the time series are > 0.99. The correlation matrix from both simulation show a similar strip pattern (Figure 4.7(b) and 4.8(b)), which looks like a wave interference pattern. It indicates that this pattern may be related to the periodicity of the time series of phase. In the following two sections, discussion and further investigation would be made on the inner product time series and correlation matrix, respectively. Both analytical derivation and simulation would be done in order to explain the patterns shown in the simulated results.

4.5 Discussion on the inner product

4.5.1 Simulations with controlled condition

In order to further investigate the property of eigenvector inner product time series, a series of simulations with controlled condition were performed. Figure 4.9 shows four conditions simulated: 2 oscillators in Figure 4.9(a), 3 oscillators in Figure 4.9(b), and 4 oscillators in Figure 4.9(c) and 4.9(d). At the starting point, all oscillators in Figure 4.9(a), 4.9(b) and 4.9(c) were isolated, which means there was no connection in the network. In Figure 4.9(d), 4 oscillators were grouped into 2 clusters at the starting point, with 2 oscillators in each cluster. For all the simulations, a connection was established between two oscillators at discrete time 1.

In Figure 4.9, the sharp decreases can only be observed in the 2-oscillator and 3-oscillator cases, while no sharp decrease is found in either of the 4-oscillator simulations. From that, it can be concluded that the density of the sharp decreases is related to the number of oscillators in the system, more oscillators in the system would make fewer sharp decreases in the

(a) 2-oscillator system

(b) 3-oscillator system

(c) 4-oscillator system without cluster

(d) 4-oscillator system with 2 clusters, each cluster includes 2 members
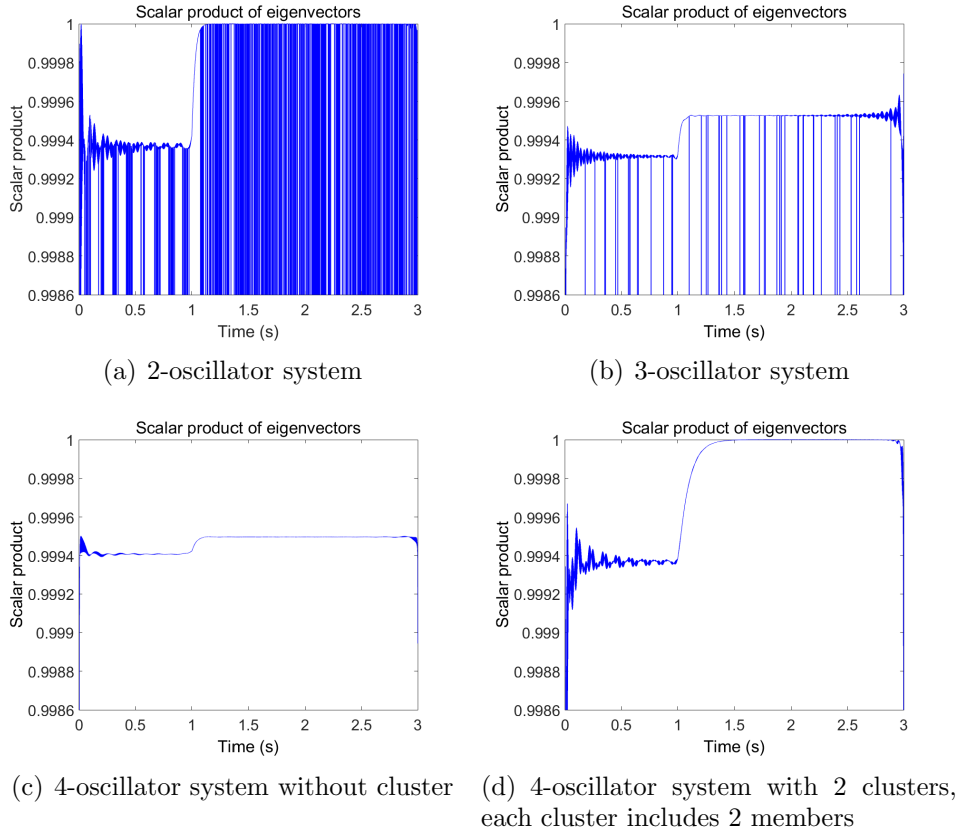
Figure 4.9: Scalar product of systems with different setups. (a) 2-oscillator system; (b) 3-oscillator system; (c) 4-oscillator system without cluster; (d) 4-oscillator system with 2 clusters, each cluster includes 2 members. For all the systems, there is no coupling in the 1st second, and oscillator 1 and 2 are coupled in the 2nd second, then no connection changes in the 3rd second. The artefact in the beginning and ending results from Hilbert transformation. It can be seen that more oscillators the system has, the less spikes there are in the scalar product. Another observation is that there is a step increasing at 1 second, when oscillator 1 and 2 started to couple with each other. It seems that the scalar product reflects the overall synchronization level of the system. Details will be discussed in the following section.

inner product time series. Also, it seems that those decreases are placed randomly in the time series and not related to the changes of synchrony states of the system.

In the simulations, a synchronisation event was set at time point 1 sec, and an increase of the baseline at 1 sec can be observed from all the four subfigures of Figure 4.9. It was also observed that the increases at 1 sec are quite large in Figure 4.9(a) and 4.9(d), and the increase in Figure 4.9(b) is slightly larger than that in Figure 4.9(c). These observations imply that the inner product of successive eigenvectors is related to the overall synchrony level of the whole system. In order to examine if that is true, let us look at the prime eigenvector in details: the n-dimensional eigenvector at time t would be

$$\Phi_t = \{e^{i\phi_{1,t}}, e^{i\phi_{2,t}}, \cdots, e^{i\phi_{n,t}}\} \tag{4.15}$$

and the eigenvector at time $t + 1$ would be

$$\Phi_{t+1} = \{e^{i\phi_{1,t+1}}, e^{i\phi_{2,t+1}}, \cdots, e^{i\phi_{n,t+1}}\} \tag{4.16}$$

Consider the case when all the oscillators are synchronised with each other, which means that all the oscillators share the same phase increment, as they have the same frequency. That is

$$\phi_{m,t+1} = \phi_{m,t} + \omega, m \in \{1, 2, 3, \cdots, n\} \tag{4.17}$$

where ω is one-step phase increment. Then v_t and v_{t+1} would have the following relation:

$$\Phi_{t+1} = \Phi_t \cdot e^{i\omega} \tag{4.18}$$

Then the inner product becomes

$$\Phi_{t+1} \cdot \Phi_t = e^{i\omega}\Phi_t^2 \tag{4.19}$$

where the absolute value reaches 1 when all oscillators in the system are synchronised. What's more, the real part of the inner product would also be quite large and reach its maximum in an all-synchronised situation, as the increment ω would have a very small value when the sample rate is high. For example, a 3Hz oscillator with sample rate of 1kHz has a step-increment $\omega \approx 0.01885$, whose cosine approximately equals 1. As the eigenvector Φ_t is normalized, whose square equals 1, the real part of the scalar product $Re\{\Phi_{t+1} \cdot \Phi_t\} = Re\{e^{i\omega}\} \approx 1$.

The above discussion is made on the case when all the oscillators are synchronised. In that case, the degree of freedom (DOF) of the system is 1, which is the only phase increment ω. Now assume that there is one independent oscillator in the system, which makes the DOF of the system equal to 2. Then Equation (4.18) would alternatively be

$$\Phi_{t+1} = \Phi_t \begin{bmatrix} e^{i\omega} & 0 & \cdots & 0 & 0 \\ 0 & e^{i\omega} & \cdots & 0 & 0 \\ \vdots & \vdots & \ddots & \vdots & \vdots \\ 0 & 0 & \cdots & e^{i\omega} & 0 \\ 0 & 0 & \cdots & 0 & e^{i\omega_i} \end{bmatrix} \tag{4.20}$$

where ω_i is the phase increment of the independent oscillator. This equation

can be rewrite as

$$\Phi_{t+1} = \Phi_t \left(\begin{bmatrix} e^{i\omega} & 0 & \cdots & 0 & 0 \\ 0 & e^{i\omega} & \cdots & 0 & 0 \\ \vdots & \vdots & \ddots & \vdots & \vdots \\ 0 & 0 & \cdots & e^{i\omega} & 0 \\ 0 & 0 & \cdots & 0 & e^{i\omega} \end{bmatrix} + \begin{bmatrix} 0 & 0 & \cdots & 0 & 0 \\ 0 & 0 & \cdots & 0 & 0 \\ \vdots & \vdots & \ddots & \vdots & \vdots \\ 0 & 0 & \cdots & 0 & 0 \\ 0 & 0 & \cdots & 0 & e^{i\omega_i} - e^{i\omega} \end{bmatrix} \right)$$

$$\tag{4.21}$$

$$\Phi_{t+1} = \Phi_t \cdot e^{i\omega} + \zeta \tag{4.22}$$

where ζ is the product between Φ_t and the second matrix at the right hand side of Equation (4.21). ζ would be a vector with all but one entries equal to zero, so there is a large angular separation between ζ and Φ_t, which also increases the angular separation between Φ_{t+1} and Φ_t. Therefore the inner product in this case would be smaller than the all-synchronised case. From the above equations, it can be found that the more DOF the system has, the smaller inner product becomes.

In order to further demonstrate the above conclusion, a simulation with a "stage" setting for the 4-oscillator system was performed: In the 1st second, no phase-locking coupling; In the 2nd second, oscillator 1 is coupled with oscillator 2; In the 3rd second, all of oscillator 1, 2, and 3 are coupled with each other; And in the 4th second, all of the 4 oscillators are coupled with each other. The inner product time series is shown as Figure 4.10. A "stage" increasing of the inner product can be observed. The oscillation in the inner product time series results from the distortion of Hilbert transform. Figure 4.11 shows the result of using simulated phase data directly without using the Hilbert transform, and no oscillation is presented in the
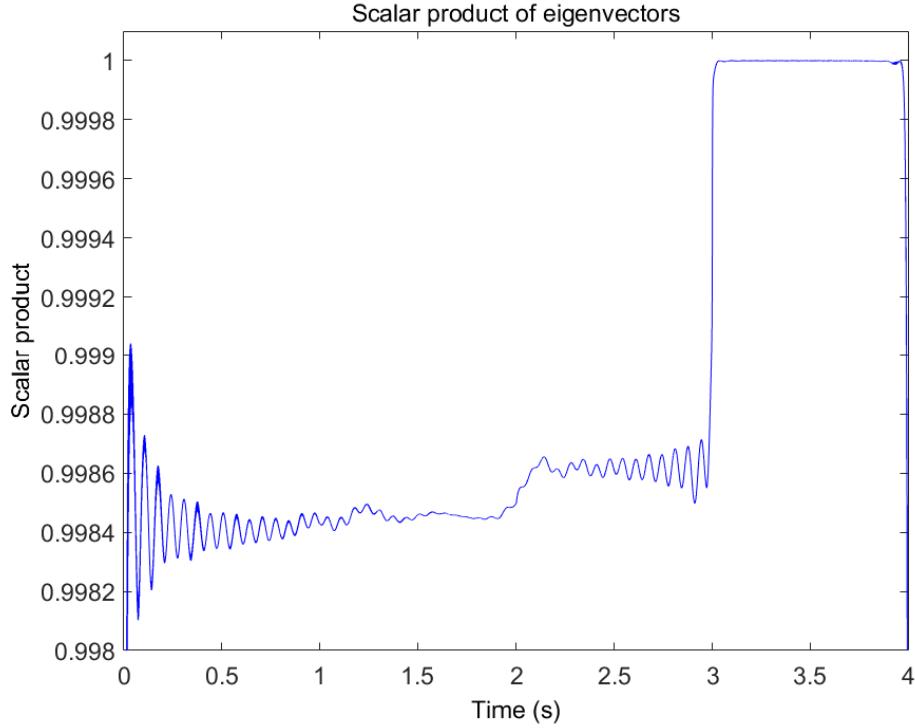
Figure 4.10: Stage increasing scalar product. The frequency of the 4 oscillators are: 1Hz, 5Hz, 10Hz, and 15Hz.

figure.

4.5.2 Effect of noise

In order to better characterise the inner product time series, the noise was also introduced and its effect on the inner products was investigated. The noise was directly added on the phase because any modification affected on the amplitude of the oscillation would be ignored during the analysis. A small noise was added on the phase, then Equation (4.7) becomes

$$\phi_{n,t+1} = [(\phi_{n,t} - \phi_{n,t-1}) + \phi_{n,t}] + a[(\phi_{m,t} - \phi_{n,t}) - (\phi_{m,t-1} - \phi_{n,t-1})] + \nu \quad (4.23)$$
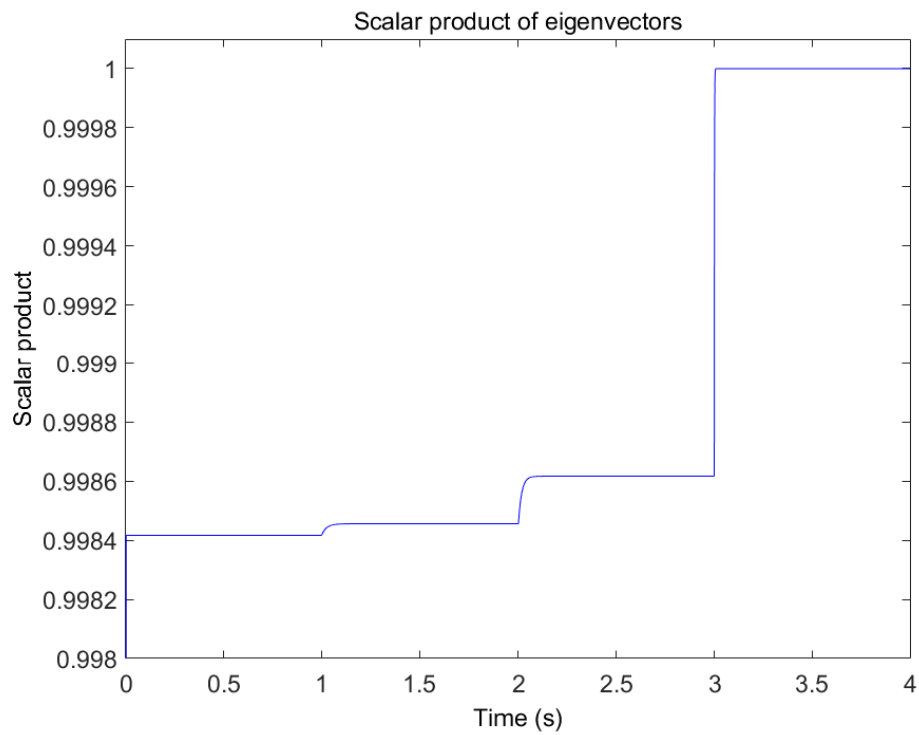
Figure 4.11: The scalar product of eigenvectors, calculated directly from the simulated phase data instead of applying Hilbert transform. There is no oscillation in the figure, which indicates it is a distortion resulted from Hilbert transform.

where ν is uniformly sampled from $[-0.0005, 0.0005]$. As it has been shown that the overall synchronisation level of system affects the inner product, the noise effects were compared on systems with different level of synchronisation. A 4-oscillator system with no initial interaction was set up, and four 3-second time series with different situations were generated. In the first case, all the 4 oscillator were synchronised with each other at 1 second, which should show a large increase of inner product. In the second case, instead of 4, only 3 of them were synchronous at the same time point. For both cases, a noisy and a noise-free sample were generated, respectively. The inner product time series of the simulation are shown in Figure 4.12. From the Figure 4.12(a) and 4.12(c), 3 cases, which are degree of freedom equals 1, 2 and 4, can be observed. It seems that the noise effect of DOF=2 and DOF=4 are not significantly different, as we can not find obvious boundary in Figure 4.12(c). However, obvious boundary can be found in Figure 4.12(a), which indicates that noise has little effect on the highly synchronised system. Oscillators which are strongly synchronised could neutralise the independent identical distributed noise through synchrony forces. Also it was found that the noise would not effect the density of sharp decreases on the inner product time series.
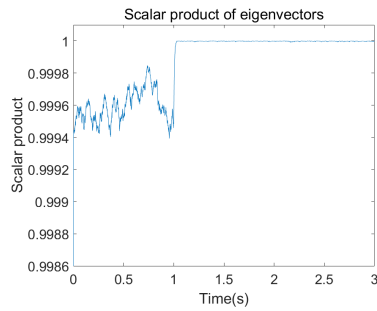
(a) 4 oscillators synchronized in the 1 second
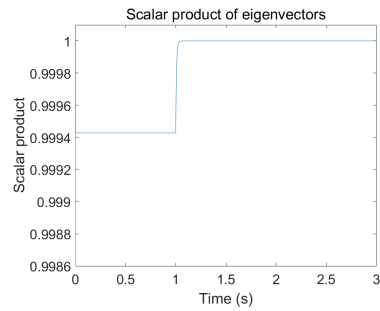
(b) 4 oscillators synchronized in the 1 second, without noise
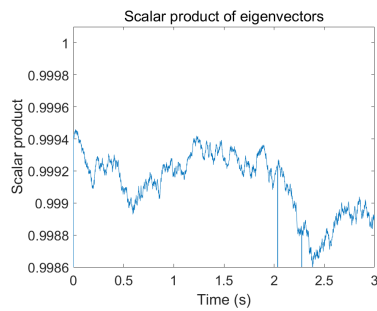
(c) 3 oscillators synchronized in the 1 second, 1 still move freely
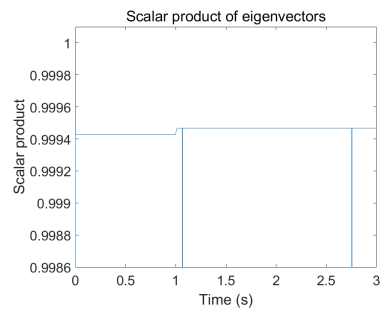
(d) 3 oscillators synchronized in the 1 second, 1 still move freely, without noise

Figure 4.12: The prime eigenvector inner product of a 4-oscillator system with noise. In subfigure (a) and (b), all the oscillators were coupled with each other at time point 1 sec, which brought a big increase on inner product. The increase was still observable with noise added. However, in subfigure (c) and (d), where only 3 out of 4 oscillator were coupled and 1 was left out, the small increase of the inner product was overwhelmed by the noise.

4.6 Discussion on correlation matrix of eigenvectors

4.6.1 Eigenvalues of correlation matrix

The definition of complex adjacency has given the eigenvector correlation matrix some interesting properties. One of them is that the number of non-zero eigenvalues of correlation matrix always equal to the number of oscillators in the system, this conclusion can be proven as following. Without loss of generality, let us assume the number of oscillators in the system is 3. Then, the eigenvector correlation matrix C has entry at ith row and jth column

$$C_{ij} = \Phi(i) \cdot \Phi(j) = e^{i(\phi_{1,i}-\phi_{1,j})} + e^{i(\phi_{2,i}-\phi_{2,j})} + e^{i(\phi_{3,i}-\phi_{3,j})} \qquad (4.24)$$

where $\Phi(i)$ and $\Phi(j)$ are the prime eigenvectors at time point i and j, respectively. This equation indicates that every entry of C can be decomposed into the sum of 3 components, which also means that the whole matrix can be decomposed in the same way. Define vectors u_1, u_2, u_3 as

$$u_1 = \left(e^{i\phi_{1,1}}, e^{i\phi_{1,2}}, e^{i\phi_{1,3}}, \cdots, e^{i\phi_{1,L}}\right)^T \qquad (4.25)$$

$$u_2 = \left(e^{i\phi_{2,1}}, e^{i\phi_{2,2}}, e^{i\phi_{2,3}}, \cdots, e^{i\phi_{2,L}}\right)^T \qquad (4.26)$$

$$u_3 = \left(e^{i\phi_{3,1}}, e^{i\phi_{3,2}}, e^{i\phi_{3,3}}, \cdots, e^{i\phi_{3,L}}\right)^T \qquad (4.27)$$

The first sub-note of ϕ refers to the index of vector, while the second sub-note refers to the time index. L is the length of time series. By definition, vector u_1, u_2, and u_3 are the time series of oscillator 1, 2 and 3. In the

following discussion, I will show that these three vectors u_1, u_2, and u_3 are the three eigenvectors of the correlation matrix C. Substitute u_1, u_2, and u_3 into Equation (4.24):

$$C = u_1 u_1^* + u_2 u_2^* + u_3 u_3^* \qquad (4.28)$$

where the star on the shoulder refers to conjugate transpose. Here a fact should be pointed out that self-adjoint matrix can be decomposed as a sum of products of its eigenvector which is weighted by the eigenvalue. That is, for a self-adjoint matrix A, it satisfies the following equation:

$$A = \sum_{n=1}^{R} \lambda_n v_n v_n^* \qquad (4.29)$$

where λ_n and v_n are corresponding eigenvalue and eigenvectors, and R is the rank of matrix A. Recognising the similarity between Equation (4.28) and (4.29), it can be concluded that u_1, u_2, and u_3 are three eigenvectors of C, and the corresponding eigenvalues can be derived by normalize them. Given that correlation matrix C can be fully constructed by u_1, u_2, and u_3, it is proven that there is only 3 non-zero eigenvalues for C. This conclusion can be easily generalized to that the number of non-zero eigenvalues of C equals the number of oscillators in the system.

4.6.2 Parallel stripes of correlation matrix

This section will focus on the stripe pattern observed on the correlation matrix. Figures 4.7(b) and 4.8(b) show the parallel stripes in the diagonal blocks. I am going to demonstrate that this pattern results from the wave overlapping in this section. Consider the case that only 2 synchronous

clusters in the oscillator system, all the oscillators within one cluster are perfectly synchronised so that they share the same phase increment. Revisit Equation (4.24), it can be learnt that in the equation all the synchronised oscillators could merge into one term. For 2-cluster system, we can only write two terms:

$$C_{ij} = Ae^{i(\phi_{1,i} - \phi_{1,j})} + Be^{i(\phi_{2,i} - \phi_{2,j})} \qquad (4.30)$$

where A and B are the number of members for two cluster respectively. For convenience, let us note $\alpha = \phi_{1,i} - \phi_{1,j}$ and $\beta = \phi_{2,i} - \phi_{2,j}$, then Equation (4.30) becomes

$$C_{ij} = Ae^{i\alpha} + Be^{i\beta} \qquad (4.31)$$

based on this, we can derive

$$
\begin{aligned}
C_{ij} &= Ae^{i\alpha} + Be^{i\beta} \\
&= Ae^{i(\frac{\alpha+\beta}{2} + \frac{\alpha-\beta}{2})} + Be^{i(\frac{\alpha+\beta}{2} - \frac{\alpha-\beta}{2})} \\
&= e^{i\frac{\alpha+\beta}{2}}(Ae^{i\frac{\alpha-\beta}{2}} + Be^{-i\frac{\alpha-\beta}{2}})
\end{aligned}
\qquad (4.32)
$$

If we look along the direction parallel to the diagonal, α and β are constant according to their definition because the time lag $i - j$ is unchanged along this direction. Then C_{ij} is a constant as well. So the synchronous modes are reflected by parallel stripes in the direction parallel to the diagonal.

Now let us look along the direction orthogonal to the diagonal. In this direction the sum of two time index is constant, which is $i + j = L$, where

L is a constant. Then α and β becomes

$$\alpha = \phi_{1,i} - \phi_{1,j} = \omega_1 i - \omega_1 j = 2\omega_1 t - \omega_1 L \tag{4.33}$$

$$\beta = \phi_{2,i} - \phi_{2,j} = \omega_2 i - \omega_2 j = 2\omega_2 t - \omega_2 L \tag{4.34}$$

where ω_1 and ω_2 are the phase increments of the two clusters, and we simply replace i with t in the last step. Therefore α and β can be viewed as a simple harmonic phase along time t. The pattern depends on the value of A and B. For the special case that $A = B$,

$$C_{ij} = 2A e^{i\frac{\alpha+\beta}{2}} Re\{e^{i\frac{\alpha-\beta}{2}}\} \tag{4.35}$$

which makes the pattern a wave package, with the cosine function as the envelop. For the case $A \gg B$,

$$C_{ij} = A e^{i\frac{\alpha+\beta}{2}} e^{i\frac{\alpha-\beta}{2}} = A e^{i\alpha} \tag{4.36}$$

which indicates that the pattern becomes a simple harmonic wave.

So far only the two synchronized clusters case have been discussed. For more clusters, more complicated pattern will be expected. However, the conclusion still hold that there will be stripes parallel with the direction of diagonal.

4.7 Refined dynamical analysis method

The discussion so far has shown that the instantaneous phase matrix can only measure the overall synchronization level of the network, while the

dynamical cluster structure remains unclear. In order to reveal the cluster changes, I propose a different way which is based on the complex instantaneous adjacency matrix. The simulation results suggest that this new method could reveal the changes of meta-stable states of network cluster structure.

4.7.1   Reconstruct the functional connectivity

First, let us revisit the complex instantaneous adjacency matrix shown in Equation (4.13). From this equation, it can be learnt that the evolution trend of oscillators can not be understood from the complex instantaneous adjacency matrix, as it only contains instantaneous phase difference. Therefore, some moving time window techniques would be needed to include the information of oscillator evolutions from multiple instantaneous matrix. For experimental systems, it can be more practical to measure synchronisations not by the instantaneous phase difference, which can oscillate instantaneously randomly, but by the average angular speed, which can filter this random oscillations. By definition, the phase-locking synchrony is a state that phase difference of two signals keeps the same for a certain time period, which is

$$\phi_{m,t_1} - \phi_{n,t_1} = \phi_{m,t_2} - \phi_{n,t_2} \tag{4.37}$$

and it can be rewrite as

$$\phi_{m,t_1} - \phi_{m,t_2} = \phi_{n,t_1} - \phi_{n,t_2}$$
$$\dot{\phi}_{m,t_1} = \dot{\phi}_{n,t_1} \tag{4.38}$$

which is true when $t_1 - t_2 \to 0$. The above equations have shown that phase-locking synchrony can be measured by comparing how close the phase speed of two signals are. Therefore the new method first calculates the angular speed of the oscillators, than a time window is applied on the angular speed as following:

$$
\begin{bmatrix} e^{i\dot{\phi}_{1,t_1}} \\ e^{i\dot{\phi}_{2,t_1}} \\ \vdots \\ e^{i\dot{\phi}_{n,t_1}} \end{bmatrix} \begin{bmatrix} e^{i\dot{\phi}_{1,t_2}} \\ e^{i\dot{\phi}_{2,t_2}} \\ \vdots \\ e^{i\dot{\phi}_{n,t_2}} \end{bmatrix} \cdots \begin{bmatrix} e^{i\dot{\phi}_{1,t_w}} \\ e^{i\dot{\phi}_{2,t_w}} \\ \vdots \\ e^{i\dot{\phi}_{n,t_w}} \end{bmatrix} \rightarrow \begin{bmatrix} e^{i\dot{\phi}_{1,t_1}} & e^{i\dot{\phi}_{1,t_2}} & \cdots & e^{i\dot{\phi}_{1,t_w}} \\ e^{i\dot{\phi}_{2,t_1}} & e^{i\dot{\phi}_{2,t_2}} & \cdots & e^{i\dot{\phi}_{2,t_w}} \\ \vdots & \vdots & \ddots & \vdots \\ e^{i\dot{\phi}_{n,t_1}} & e^{i\dot{\phi}_{n,t_2}} & \cdots & e^{i\dot{\phi}_{n,t_w}} \end{bmatrix} \tag{4.39}
$$

where t_w is the time window width. Within each time window, the row vectors represent the phase trajectories of corresponding EEG channel. Instead of taking average of the time window, the Euclidean distance between each row vector is calculated, as shown in the following equation:

$$
d_{mn} = \|\overrightarrow{v_m} - \overrightarrow{v_n}\|_2 \tag{4.40}
$$

where v_m and v_n stand for the row vectors for channel m and n respectively:

$$
\begin{aligned} \overrightarrow{v_m} &= (e^{i\dot{\phi}_{m,t_1}}, e^{i\dot{\phi}_{m,t_2}}, \cdots, e^{i\dot{\phi}_{m,t_w}}) \\ \overrightarrow{v_n} &= (e^{i\dot{\phi}_{n,t_1}}, e^{i\dot{\phi}_{n,t_2}}, \cdots, e^{i\dot{\phi}_{n,t_w}}) \end{aligned} \tag{4.41}
$$

The 2-norm of vector difference represents the Euclidean distance between those two vectors. The distance d_{mn} therefore can be used as the phase-locking value (PLV) between node m and n. Comparing to the moving window averaging, this way to define phase-locking value preserves all the instantaneous information of the phase time series. By calculating this

distance-based PLV for all channel pairs, an adjacency matrix is obtained, which describing the phase-locking functional connectivity within this time window. After that, a threshold was applied on the adjacency matrix to determine if certain channel pair is phase-locked. Let us define the prime eigenvector of the binary adjacency matrix as $\overrightarrow{\Upsilon}(t)$, where t denotes time window index. By studying the inner product of the successive prime eigenvector $\langle\overrightarrow{\Upsilon}(t),\overrightarrow{\Upsilon}(t+1)\rangle$, the evolution of the network can be revealed.

4.7.2 Simulation results

This new method was tested with the simulated oscillator data. Figure 4.13 shows the angular speed trajectory of the simulated network. The network started with 4 clusters, and there were several merging and separations between these clusters. Let us name the four clusters as cluster 1 to cluster 4 from bottom up. At time point 500, clusters 1 and 2, clusters 3 and 4 merged together. At time point 1000, clusters 3 and 4 stopped interacting with each other, while a connection established between clusters 2 and 3. This connection made clusters 1, 2 and 3 started merging (as the connection between clusters 1 and 2 remained). At time point 1500, clusters 1 and 2 stopped interacting with each other, while clusters 3 and 4 started synchronisation. Finally, it can be seen that clusters 2, 3 and 4 merged into a super cluster while cluster 1 stood out from others. The inner product time series of prime eigenvectors are shown as Figure 4.14. It can be found that inner product decreases at every time point of cluster structure changing, although the decreasing is small. It can be observed that there are multiple decreases around one change point. That could result from the delay between the starting and finishing of the synchroni-
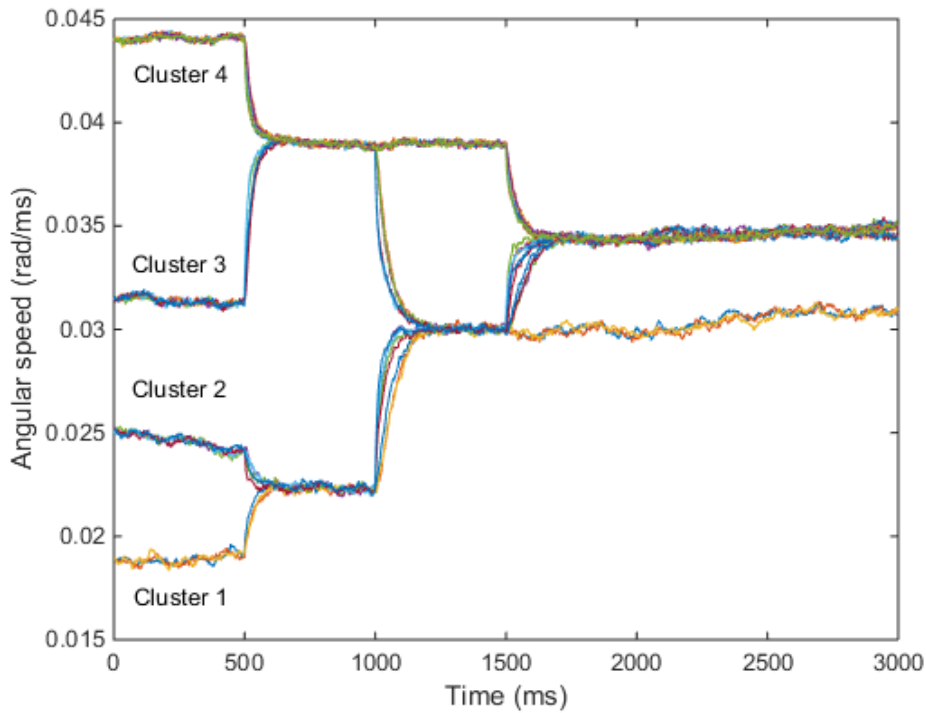
Figure 4.13: The angular speed time series of the oscillators, demonstrating the evolution of the system. At time point 500, clusters 1 and 2, and clusters 3 and 4 were synchronised. At time point 1000, cluster 3 went out of synchrony with cluster 4, but started to synchronise with cluster 2 instead. At time point 1500, clusters 1 and 2 went out of synchrony, while cluster 3 and 4 resume synchrony.

sation. Also the correlation matrix C is shown in Figure 4.15. A very clear block structure can be observed in the figure, each block on the diagonal suggests a meta-stable state. By this new method, the changes of network structures can be detected.

The following chapters will show that the functional connectivity network of EEG was constructed and analysed with the new method proposed in this chapter.
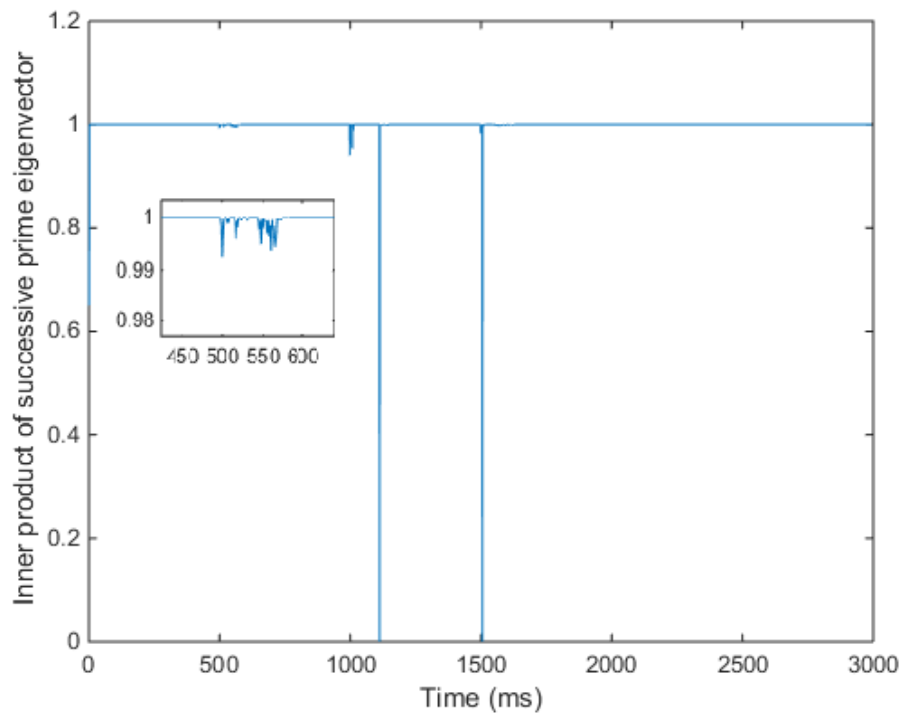
Figure 4.14: The inner product time series of successive prime eigenvectors. The small subfigure enlarges the decreases around time point 500. It can be seen that one or more decreases took place at the time point when the network structure changed. When the changes happened, it took time that the clusters newly connected reached synchronisation, which probably results in multiple decreases.
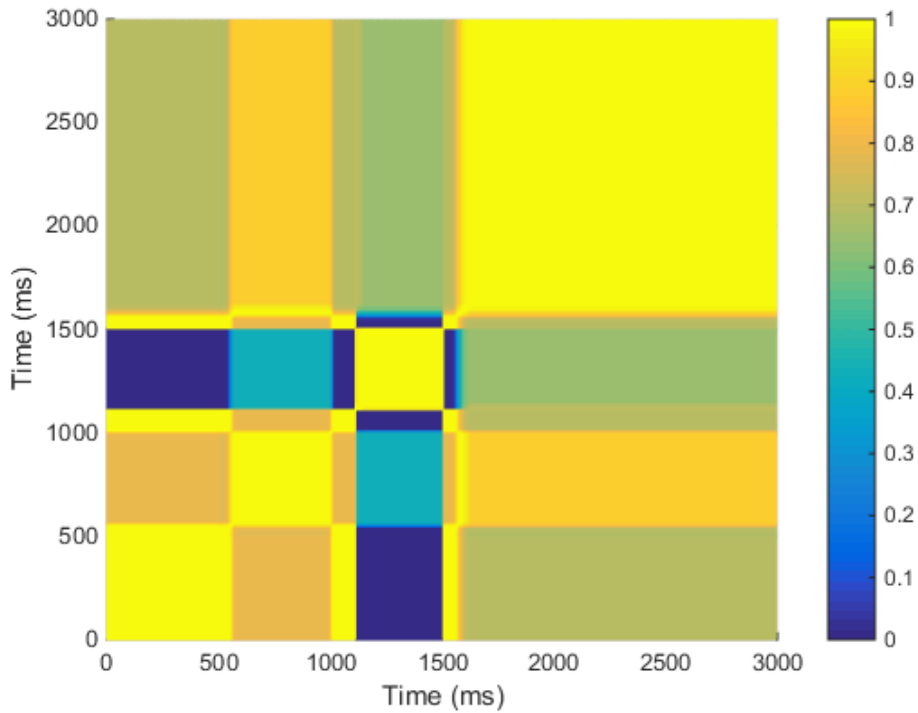
Figure 4.15: The correlation matrix C, whose entry c_{ij} is the inner product between prime eigenvector at time i and time j. The matrix shows an obvious block structure. As the prime eigenvectors within the same meta-stable state have similar direction, their inner product should be a very high value. Therefore, the high value blocks along the diagonal correspond to the meta-stable states of the system.

Chapter 5

Static Topological Properties
of Functional Connectivity

Contents

5.1 Introduction

In the last chapter, an eigenvector-based analysis method was developed and tested with a simulated dynamical network model. The following two chapters will show that this method can be applied on the functional connectivity network configured from EEG. This chapter focus on analysing the topological properties of the time-averaged static network, the next chapter will explore the dynamics of the evolutional network.

When brain engages certain activity, the collaboration of different regions of brain would generate a certain pattern of correlated neural activities. By observing these correlated neural activities, the correlation between regions can be measured and an abstract network based on those correlation can be defined, which is called functional connectivity network. The nodes of the functional connectivity network usually represent different spacial locations of the brain cortex, while the links are constructed based on the correlations between the neural signals of nodes. The topological structure of the functional connectivity network includes the information of the corresponding neural activities. Thanks to the network theory, many measurements have been developed to describe those topological structure of the network [52]. These topological properties give an insight into the corresponding neural activity, and further into the neural mechanism of related behaviour.

The EEG analysis of this study focused on the difference between the full visibility tracking (Tra) trials and two reference trials, motion only (MO) and visual only (VO) (See Section 3.2.1.2). For tracking trial, the 1Hz trial was selected as it has the highest target speed, which requires the most intensive involvement of the visual-motor neural circuits. The two reference trials, MO and VO, as discussed in Section 3.2.1.2, represent two different visual-motor cognitive states. By comparing the Tra trials with MO and VO trials, it was expected that the neural features corresponding to the different parts of visual-motor control can be separated. In this chapter, the functional connectivity network of EEG was constructed with phase-locking value, as described in Section 4.7. Three topological properties, network density, clustering coefficient, and the average efficiency,

of the time-averaged functional connectivity network were investigated. It was found that all these topological properties showed significant difference between different experimental conditions, which suggests that different visual-motor coordination states have different topological structures of the functional connectivity. As a further step, the overall topological structure of functional connectivity links in the alpha and gamma band were investigated. The results indicated that the significant differences in topological properties are related to different topological structures of functional connectivity links. These analyses have revealed that open and closed visual-motor loops would result in different topological structure of the static functional connectivity network.

5.2 Methods

The previous chapter has introduced the functional connectivity defined on the PLVs which were calculated from the instantaneous angular speed vector (see Section 4.7). This chapter will show the investigation of the topological properties of the EEG functional connectivity which was defined with the same method.

5.2.1 EEG acquisition and pre-processing

Electroencephalography (EEG) was recorded through the whole session of experiment with 1kHz sampling rate. 32 electrodes (F3, F1, Fz, F2, F4, FC5, FC3, FC1, FC2, FC4, FC6, C5, C3, C1, Cz, C2, C4, C6, CP3, CP1, CPZ, CP2, CP4, P3, P1, PZ, P2, P4, PO3, POz, PO4, Oz) plus 1 reference electrode (FCz) and 1 ground electrode (AFZ) (g.tec) were

applied in the experiment. The electrodes were connected to 2 g.BSamp 16-channel amplifiers (g.tec). Each amplifier output the signals to an A/D board (CONTEC CO., Ltd) to digitalise the signals, then the digital signals were sent to a PC with xPC-Target running (The MathWorks, Inc). A haptic arm with two encoders, corresponding to X and Y coordinates of the tracer, respectively, was used for participants to control the tracer. The signals of two encoders went to a counter board (CONTEC CO., Ltd), which integrated the angle changes and gave the current position of the tracer. Outputs of the counter board would also be sent to the target PC. This target PC would synchronise the EEG signals and behaviour signals, then sent them to the main PC through an ethernet cable with User Datagram Protocol (UDP). The programme running on the main PC was based on MATLAB and Simulink (The MathWorks, Inc), the programme read and recorded data received from target PC, and played the animation on the screen. A detailed description of the EEG acquisition system is presented in the appendix.

MATLAB and EEGLAB (Swartz Center for Computational Neuroscience, La Jolla, CA) were used to process EEG data. First of all, each dataset was fed into a broad band-pass filtering (0.1-50Hz, all the filtering process in this study applied EEGLAB embedded FIR filter), then the filtered time series were cut into trials according to time stamps. Then an independent component analysis (ICA) was performed on the data in order to remove eye blinking and other artefacts, which was implemented with EEGLAB embedded function ("runica"). The independent components (ICs) recognized as artefacts were selected through visual inspection. There are toolboxes for EEGLAB that automatically perform IC rejection,

which have been tried but failed to give satisfying result. In the manual selection process, the ICs with random occurred stand-alone peaks which had a source from the frontal (blink pattern) and high frequency jitters (electromyographic pattern) would be considered as artefacts. The whole trial would be rejected if more than 50% ICs were recognized as artefacts. After ICA pruning, the data were processed with Laplacian operator through CSD toolbox [95, 96, 97]. This processing was aimed to avoid the phase synchronisation resulted from both electrodes sharing a common source.

5.2.2 Phase-locking synchrony connectivity

Narrow band-pass filtering was done on the pre-processed data to reduce the frequency components so that phases of the signals can be defined. 4 frequency bands were selected, which are 8-12Hz, 18-22Hz, 26-30Hz, 38-42Hz [98, 32]. After that, Hilbert transform was applied to extract the phase from time series. Here the phase was noted in the complex exponential form because it's easier to deal with the period in complex space. Then the first order differentiation was performed on the phase time series to get the instant angular speed. Following Equation (4.39), a moving time window (width = 40ms, step = 5ms) was then applied on the angular speed time series. For each channel, the segment of time series within the time window corresponded to each row vector. The Euclidean distances between each row vector were calculated as shown in Equation (4.40). Then an adjacency matrix was constructed for each time window, whose entries were PLVs defined by the distances between row vectors. After that, a threshold was applied on the adjacency matrix to binarize it. The threshold was determined through visual inspection. As phase-locking is defined

by the constant phase difference, I have reviewed the raw time series of phase, and calculated the phase locking value for the signals pairs which were found to be phase-locked in the raw time series. Figure 5.1 shows a segment of angular speed time series from the actual EEG data, which further demonstrate the selection of the threshold. The two arrow pairs in the figure indicate two example segments of phase-locking. The segments of channel F1 (blue triangles in the figure) and FZ (yellow triangles in the figure) between the magenta arrow pairs are very close to each other during this certain period of time, so they are identified as phase-locked during this period of time. The segments of channel P1 (purple hexagon) and PZ (green hexagon) between red arrows provide another example of the phase-locking channel pairs. P1-PZ channel pair has very close spatial distance on the scalp, and so does F1-FZ pair, which suggests these two channel pairs are very likely to become phase-locked. With a large number of samples having been reviewed and calculated, the proper threshold (4×10^{-4}) for the binary functional connectivity matrix was determined. At this stage, a time series of binarised adjacency matrix was obtained, which represents the evolving functional connectivity of brain signal.

5.2.3 Static property analysis

Three topological properties, network density, mean efficiency and cluster coefficient [52] were calculated for each time window, then the time averaging were performed on the topological property time series. Instead of mean path length, the mean efficiency was calculated. The mean efficiency is defined in Section 2.4, which is the averaging of the reciprocal of the shortest path length for node pairs. The reason for using efficiency
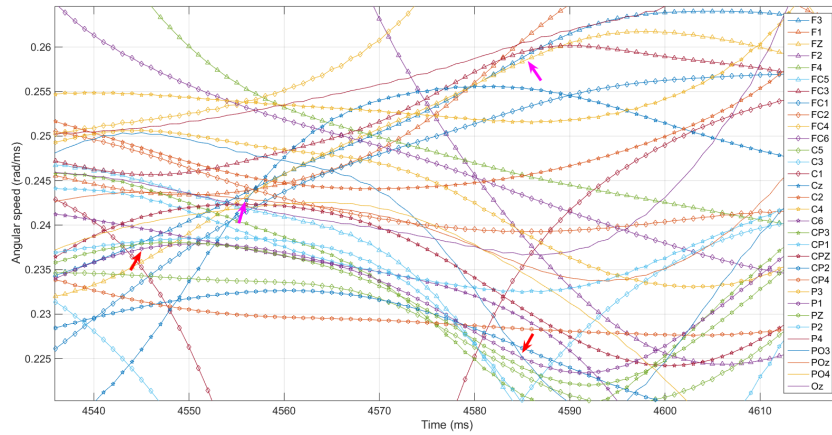
Figure 5.1: A segment of angular speed time series, where each curve stands for one EEG channel. The legend shows the location of each electrode in 10-20 system. By definition, phase-locking synchrony means angular speed of two signals are equal or very close in a certain time period. Therefore in the figure, two signals are in a phase-locking synchrony state if they are very close to each other during that certain time period. Two arrow pairs give two example of phase-locking synchrony. Channel P1 (purple hexagon) and PZ (green hexagon) are synchronized between two red arrows, as they are very close to each other during this period. Channel F3 (blue triangle) and FZ (yellow triangle) between two magenta arrows give another example of synchronisation. We searched for this case and calculated their PLV value to determine our threshold.

rather than path length is that the unweighted networks of the EEG functional connectivity were very sparse, with many disconnected nodes, while the shortest path length is not well defined for the isolated nodes. Efficiency is a generalized metric that describes the same characteristic of networks as shortest path length while it can be applied on disconnected networks. Statistical comparisons between the three conditions were performed on the time-averaged topological properties of all 12 participants, the results of which are shown in Table 5.1 and Figure 5.2. In order to directly assess the structure of the functional connectivity, the time-averaged functional connectivity (a single network calculated from the dynamical

network series) was defined, the connections of which were weighted with their averaged appearing probabilities. First, the recurrence probability of each connection was estimated within each individual trials. Then the probability networks of all the trials from the same experimental condition were averaged, which made a single representation of functional connectivity for every condition. In order to demonstrate the network structure in Figure 5.3, a threshold has been applied on the averaged network for the visualisation purpose. Consistent with findings of topological properties (which will be discussed later), it was found that the network density of VO in the alpha band and MO in the gamma band grow faster as a function of the threshold than other conditions. Therefore the threshold was chosen in a way that could demonstrate the most differences between the two conditions and others.

5.3 Results

The time-averaged topological properties of the functional connectivity network have been systematically compared between three different conditions: tracking condition (Tra), motion only condition (MO), and visual only condition (VO). Three topological properties, connection density, mean efficiency, and global clustering coefficient, were calculated for each trial. Efficiency is defined as the reciprocal of shortest path length. It is a generalization of shortest path length which can be used on disconnected graph. The efficiency was calculated instead of shortest path length in this research to characterize the network. These calculation were performed for 4 different frequency bands of the EEG signal, 8-12Hz, 18-22Hz, 26-30Hz,

and 38-42Hz [98, 32]. The statistical test was performed on the datasets of all the 12 participants. It was found that all the three topological properties were highly correlated with each other. For a certain condition pair, the results of statistical tests for all the three topological properties would be the same. The statistical significance of all the comparisons is summarized in Table 5.1. Figure 5.2 shows the histogram of the three topological properties. Both Wilcoxon signed-rank test and ANOVA were performed on the data and gave consistent results for the significant differences between conditions.

Frequency band	Tra vs. MO	Tra vs. VO	MO vs. VO
8-12Hz	0	1	1
18-22Hz	1	1	1
26-30Hz	0	1	1
38-42Hz	1	0	1

Table 5.1: Results of statistical comparison of topological properties. Wilcoxon signed-rank test was used to exam the significance. 1 means that the alternative hypothesis has been accepted, indicating there is a significant difference between these two conditions, while 0 means there is no significant difference between these two condition. For all those showing significance, $p < 0.005$.

In 8-12Hz and 26-30Hz band, VO trial showed significantly higher density, higher clustering coefficient, and higher efficiency (lower mean path length) than Tra and MO trials. In 38-42Hz band, MO trial showed significantly higher density, higher clustering coefficient, and higher efficiency (lower mean path length) than Tra and VO trials. In 18-22Hz band, all three conditions showed significant difference from each other.

Besides the statistical difference, the topological structure of the networks in the alpha and gamma band were directly assessed, which are shown in Figure 5.3. The representative network of each condition was
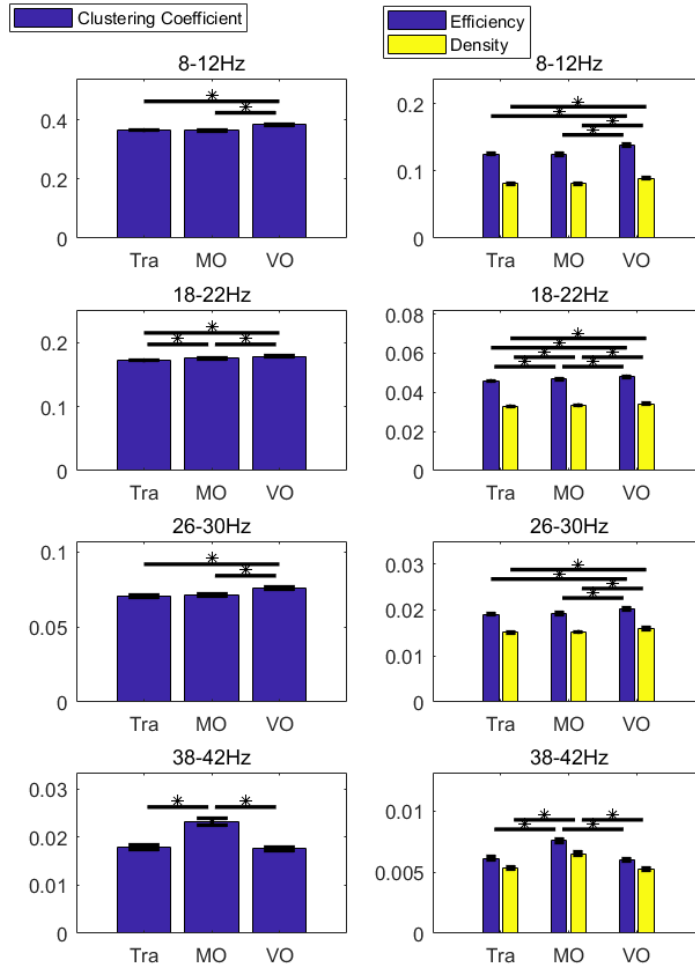
Figure 5.2: This figure shows the histogram of three statistical topological properties of functional connectivity network. Each row represents the measurement in a frequency band, while the left column shows clustering coefficient of the connectivity, and right column shows mean efficiency (average reciprocal of least path length) and network density. Each error bar represents the standard error of the mean value. The horizontal bars with star indicate pairs showing significant difference.

95
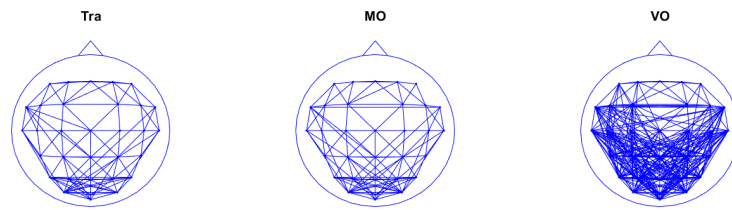
(a) Functional connectivity of the alpha band (8-12Hz)
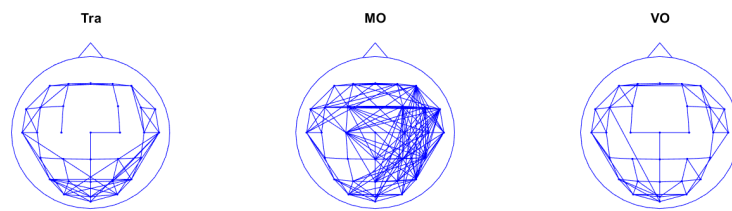
(b) Functional connectivity of the gamma band (38-42Hz)

Figure 5.3: A comparison of functional connectivity structure in the alpha (Subfigure a) and gamma (Subfigure b) band between each condition. The probability of each link was estimated for each trial, then the trial-wise averaging was performed, which generated a single representative network for every condition. For the purpose of better demonstration, a threshold was applied on the averaged network and it was tuned in the way so that different features of network structure can be clearly shown.

an average of all trials of the same condition, and it was a weighted network. Here only the strong links in the networks are shown to illustrate the topological structure discriminating different conditions.

It is obvious that there is one condition significantly different from the other two conditions in each frequency band. In 8-12Hz band, VO trial had much denser connections in the occipital part of the scalp. In 38-42Hz band, MO trial had more connections than Tra and VO trial on the right hemisphere and occipital part. In the networks with lower density, it can be found that the connectivity structures are similar to the lattice network. It could result from the neighbouring effect of electrodes. Two electrodes may receive the signal from a common source, which then creates the same component for both channels, and that would finally result in that this channel pair has higher phase-locking value.

5.4 Discussion

Table 5.1 and Figure 5.2 provide an overview of the topological properties, which made different conditions stand out in different frequency bands. In the alpha band (8-12Hz), VO was significantly different from the other two conditions in all the topological properties, which indicates that the alpha band neural activity is related to the motor control. In the gamma band (38-42Hz), MO was significantly different from the other two conditions in term of all topological properties, which indicates that gamma band activity is related to the visual tracking behaviour. The topological structures of the representative networks were also found to be different between conditions in both alpha and gamma band, which are shown in Figure

5.3. The beta band (18-22Hz and 26-30Hz) showed significant difference in statistical topological properties between conditions but no significant difference of the functional connectivity network structure was found in the representative networks (not shown). Figure 5.2 and Figure 5.3 show that Tra condition had a lower density of connections in both alpha and gamma bands, while VO in the alpha band and MO in the gamma band had a higher connection density. Considering VO condition in the alpha band and MO condition in the gamma band as two baseline conditions of the open visual-motor loop, it can be concluded that closing of the loop during tracking task led to desynchronisation in both frequency bands. Desynchronisation of neural signal can be related to movement onset, which is called event-related desynchronisation (ERD) [98], and it is believed to be related to motion control. After the stimulus, a series of time-locked events take place but those events are not synchronous with each other, which result in the desynchronisation of EEG. The inter-channel desynchronisation found in this research may result from the same mechanism: the real-time visual-motor coordination requests intensive communication to establish the fine control, and the neural signal of the communication could be asynchronous due to the random nature of the disturbance in participant's motion. Therefore, the time averaged synchrony measurement showed lower value of synchrony.

Figure 5.3 shows that there was a difference of representative network topological structures between conditions in both alpha and gamma band. In the alpha band, VO shows higher density of connections than the other two conditions, where the differences are mainly in the occipital region and the back part of central region. A study from Rilk et. al. reported

that visual-motor coordination task would result in a decrease of oscillatory power of central and occipital regions in the alpha and low beta band, while the the interregional coherence between central region and occipital region would increase [7]. It should be noticed that the baseline used for comparison in that study was the rest state of participants. In this study, however, visual-motor coordination state was compared with visual only state and motion only state. In other words, this experimental design isolated motor control from the overall visual-motor feedback loop. Therefore, differences of connections shown in Figure 5.3 are specifically related to the motion control activity. This result implies that the motion control in the visual-motor coordination loop is related to the back part of central region and the occipital region. It should be pointed out that the rear part of the occipital region in Tra and MO of the alpha band has less density difference from the VO. It indicates that this rear part of the occipital region may not be related specifically to the motor control.

In the gamma band (38-42Hz) of Figure 5.3, MO showed different network structures and topological properties from the other two conditions. In order to interpret this difference, let us revisit the behaviour conditions. In MO condition, participants were asked to perform a circular motion of the tracer while the target was not shown. In VO condition, participants passively watched a pre-recorded tracking trial with both target and tracer shown on the display. As the VO trials exhibited the exactly same visual input as Tra trials, it can be concluded that the differences of functional connectivity structures in the gamma band resulted from the different visual inputs from the display. There are two possible explanations of the gamma band neural activity. One explanation is that participants applied differ-

ent attention on the moving object(s) which generated different gamma band connectivity networks. A number of studies have demonstrated the visual attention is related to the gamma oscillatory [99, 100, 101]. In Tra and VO trials, multiple moving objects were shown on the display, which could be more likely to catch participants' attention than showing a single, under-controlled moving object. Another possible explanation is that the different intention of participants resulted in the differences of functional connectivity in the gamma band. As the participants were watching both target and tracer, either with control (in Tra trials) or without control (in VO trials), participants would start to visually measure the distance of the two objects and activate the relative brain connectivities. In our future work, the attention of participants will be measured during the behavioural experiment in order to resolve this issue.

5.5 Conclusion

In this chapter the topological properties of static functional connectivity network were explored, which showed that the topological properties of EEG functional connectivity differ between open and closed visual-motor loop. The results suggest that the alpha and gamma bands in the brain signals are related to motor control and visual feedback, respectively. In the alpha band, the desynchronisation between central and occipital region of cortex was observed when participants engaging motion control. In the gamma band, the desynchronisation was also found while participant were minimizing distance between target and tracer. The overall structures of the phase-locking connections in the network was also investigated

by observing the representative network of each condition. It showed that the significant difference in statistical topological properties is related to different spacial structure of the functional connectivity.

From the above analysis in this chapter, it was shown that the lower frequency band of the EEG signal is related to the movement, while the higher frequency band of EEG is related to the precise visual feedback and control. These results established a baseline which shows that the static functional connectivity structure is related to the visual-motor coordination, and different visual-motor coordination states can be distinguished by the topological properties of the functional connectivity network. The next chapter will turn the focus on the dynamical properties of the functional connectivity networks, which were extracted with the eigenvector-based method introduced in the previous chapter.

Chapter 6

Dynamical Properties of Functional Connectivity

Contents

6.1   Introduction

While in the previous chapter, it has been demonstrated that open and closed visual-motor loops are distinguished by the static topological properties of the functional connectivity, this chapter focuses on the network

evolution by investigating the dynamical properties of the functional connectivity. In order to extract the evolution information of the network, the eigenvector-based method developed in Chapter 4 was applied on the EEG functional connectivity network. This chapter shows that the evolution of the functional connectivity network is based on a serial transitions between different meta-stable states. Those meta-stable states imply an attractor structure of the network dynamics. By comparing the transition frequencies and the meta-stable states duration distribution of different conditions, it was shown that the dynamical properties of the functional connectivity network can differentiate the open and closed visual-motor coordination loops.

In this chapter, the attractor structure of the neural network dynamics will be studied with the eigenvector-based dynamical analysis method. This analysis will show that the successive prime eigenvector inner product time series depicts a natural partition of the meta-stable states of the network evolution. It will also demonstrate how the network transits between those different meta-stable states. In this chapter, two dynamical properties, the meta-stable state transition probability as well as the distribution of meta-stable state duration, will be compared between different conditions. It will also be shown that these results indicate an interrelation with the static topological properties of the functional connectivity.

At the end of this chapter, the exploration of Lyapunov exponent of the network density time series will be introduced. Lyapunov exponent is a measurement describing the separation rate of a dynamical system's trajectory in the phase space. This measurement implies the predictability of the dynamical system with noise, and is usually used to investigate

103

chaos phenomenon in nonlinear dynamical systems [68]. Many studies of neuroscience and psychology [75, 102, 73, 74, 77, 76] have suggested that the dynamical process of a brain network is chaotic. In this chapter, a primitive investigation of Lyapunov exponent will be described, which was applied on the network density time series of the functional connectivity in the alpha and gamma band. This analysis alone is not enough to provide a concrete conclusion on the chaotic property of the functional connectivity evolution, but it showed interesting results and is worthy to report in this thesis. The results showed consistence with the results of topological properties analysis, as VO in the alpha band and MO in the gamma band had significantly larger network density than other conditions in the same frequency band. The chaotic property of the functional connectivity network will be further studied in future work.

6.2 Attractors and Meta-stable state transitions

First of all, the eigenvector-based dynamical analysis method was applied on the function connectivity of EEG to investigate the dynamics of the prime eigenvector. This analysis revealed the attractor structure and meta-stable state dynamics of the functional connectivity.

6.2.1 Methods

In the last chapter (Section 5.2.1 and Section 5.2.2), the functional connectivity network of the brain signal has been generated with the method described in Section 4.7. Following the path of Section 4.7, this chapter

applies the eigenvector analysis on the functional connectivity network. The discussion in Chapter 4 assumed that several attractors exist in the trajectory of the prime eigenvectors, while two eigenvectors have very similar direction if both of them are close to the same attractor, which means $\langle \overrightarrow{\Upsilon}(m), \overrightarrow{\Upsilon}(n) \rangle \simeq 1$, otherwise $\langle \overrightarrow{\Upsilon}(m), \overrightarrow{\Upsilon}(n) \rangle \ll 1$ if they are in the basin of different attractors. Therefore, a plot of $\langle \overrightarrow{\Upsilon}(t), \overrightarrow{\Upsilon}(t+1) \rangle$ as a function of time will be composed of stable long plateaus which are close to one, punctuated by short transient decreases. The set of the average values of $\overrightarrow{\Upsilon}(t)$ over each stable period would be the attractors. They do not need to be orthogonal to each other. In Section 4.7 it has been shown that this assumption describes the correct picture of the simulated networks, and in this chapter the same method is applied on the EEG data while the similar pattern as Figure 4.14 is expected.

To test these conjectures, the prime eigenvector for each time window was calculated from the time series of binary adjacency matrix, generating a time series of prime eigenvectors $| \overrightarrow{\Upsilon}(t) |$. Then the inner product time series of successive prime eigenvectors were calculated for every trial. In Figure 6.2.2, time series of an example trial is shown. This figure indicates that the inner products tend to be either 0 or 1. The inner products distribution of the same trial is shown in Figure 6.1 (b). From the result, it was found that the distribution of a single trial follow a bimodel distribution with most of the events fell into either 0 or 1. This is compatible with the noisy attractor dynamics in the assumption. As described early, $\langle \overrightarrow{\Upsilon}(m), \overrightarrow{\Upsilon}(n) \rangle \ll 1$ suggests a transit a transition between meta-stable states while $\langle \overrightarrow{\Upsilon}(m), \overrightarrow{\Upsilon}(n) \rangle \simeq 1$ can be viewed as holding the same state during that time window. Therefore, the number of 0 in the inner product

time series suggests the number of transitions happened in the state space, and more transitions between meta-stable states implies relatively unstable. In order to identify the transition frequency, the number of events, where the inner product of eigenvectors were < 0.01 and > 0.99 were counted. Events that < 0.01 can be interpreted as prime eigenvector transits between states, and events that > 0.99 stand for the situation where prime eigenvector stays in the same state. The normalized frequency of the two events, < 0.01 and > 0.99 (these two events will be simply noted as 0 and 1 in the following text) from each experimental conditions were compared by Wilcoxon signed-rank test and ANOVA, results of which are shown in Figure 6.3.

In order to further demonstrate the temporal cluster structure and the attractors in eigenvector space, the inner products of prime eigenvectors from all the time windows in the same trial were calculated, and that makes a correlation matrix C, each entry of which is the inner product of eigenvectors from the corresponding two time windows. That is $C_{mn} = \langle \overrightarrow{\Upsilon}(m), \overrightarrow{\Upsilon}(n) \rangle$. In the purpose of better demonstration, only a segment of the whole matrix is shown in Figure 6.2, which are the inner product correlation matrix of a 3-second segment.

6.2.2 Results

While Figure 6.1 shows the bimodel distribution of the successive prime eigenvector inner product, Figure 6.2 shows the inner product matrix C of a time series segment of the trial in Figure 6.1, which shows a block structure. The blocks of high value suggest the prime eigenvectors with the similar directions, which can be seen as temporal clusters of the eigenvector
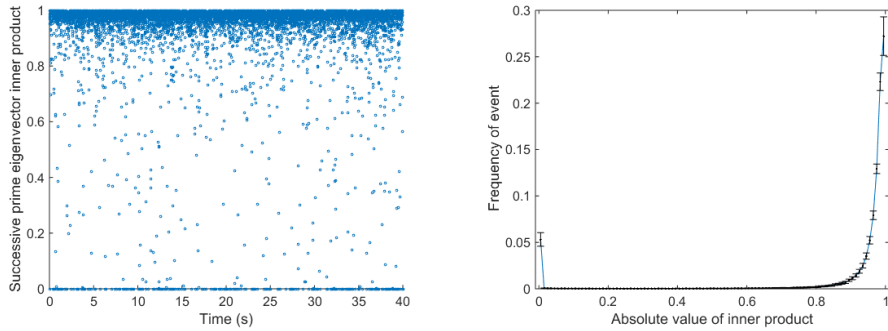
(a) Time series of successive prime eigenvector inner product

(b) Distribution of successive prime eigenvector inner product

Figure 6.1: (a) An example time series of successive prime eigenvector inner product. The figure shows the data from a single tracking trial in the alpha band. (b) Distribution of successive prime eigenvector inner product (Tra, alpha band). It is obvious that the distribution follows bimodal distribution with most of the event counts fall in 0 and 1.

trajectory. Remarkably, the high value blocks on the diagonal stand for the meta-stable states. Figure 6.2 proves that it would be possible to identify attractors in the prime eigenvector space experimentally, and the EEG functional connectivity network has a meta-stable dynamics.

The significance tests were performed on the normalized frequency of the two events between different conditions (Figure 6.3). As discussed in previous section, the inner products with small values represent the transitions of the functional connectivity. Figure 6.3 shows that in the alpha band, there are more inner products close to 1 than those close to 0, and 1 count in VO condition is significantly larger than that of Tra and MO, while 0 count is significantly smaller. This result suggests that the alpha band functional connectivity has more transitions when participants perform motion control. In the beta band (18-22Hz and 26-30Hz), a significant difference of number of transitions between Tra and VO condition was found. However, MO doesn't show significance when comparing to
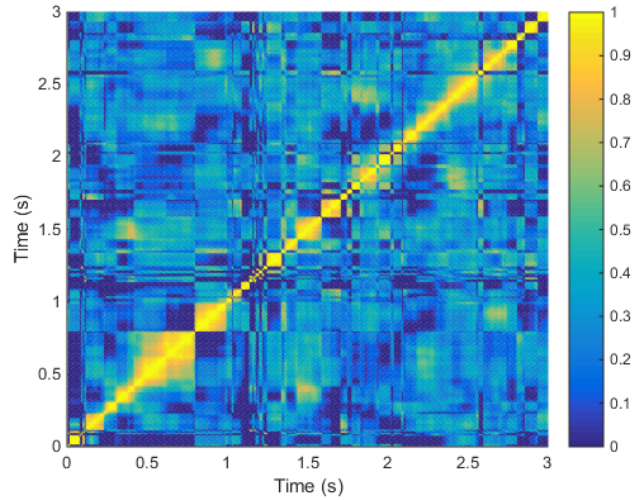
Figure 6.2: The inner product correlation matrix C of a short segment from an experiment trial which used to produce Figure 6.1. A segment (from 0s to 3s) was selected from the eigenvector time series $| \overrightarrow{\Upsilon}(t) |$ and then the inner product was calculated for every possible pair in the segment, so that each entry C_{mn} in the matrix is the inner product of the corresponding two eigenvectors, which is $C_{mn} = \langle \overrightarrow{\Upsilon}(m), \overrightarrow{\Upsilon}(n) \rangle$. It can be observed from the figure that there is a block structure. A segment of eigenvector time series having high inner product with another segment makes a block of high value in the matrix. It can be learnt that each block refers to a temporal cluster, or an attractor in the eigenvector space. This structure suggests a natural state partition of the eigenvector dynamics, from which the meta-stable states can be defined.

either Tra or VO condition. Also the p-value between Tra and VO was very close to the threshold (0.05). Therefore it is hard to conclude how the beta band functional connectivity relates to the visual-motor coordination. In the gamma band, MO condition has significantly higher transition frequency than the other two conditions, which suggests that the functional connectivity has fewer transitions and is relatively stable when participants perform tracking rather than simple circular movement. Comparing the results of Figure 6.3 and Figure 5.2, it is interesting to find that the condition pairs showing significant difference in the topological properties were also significantly different in the dynamical properties.

6.2.3 Discussion

In this chapter the method from Chapter 4 was applied on the EEG data. Comparing the inner product time series of simulated data and EEG data in Figure 4.14 and Figure 6.1 (a), respectively, it can be observed that both inner product time series have plateaus of high values separated by transit sharp decreases, which is a structure of meta-stable dynamics. The plateaus of high values represent the meta-stable states in which the eigenvector stays near one attractor, and the sharp decreases represent the moments that eigenvector made those transitions from one attractor to another. It is not surprising that the inner product time series of EEG data is more noisy than that of simulated data, as the results of EEG show a wider range of high values, around $0.8 \sim 0.9$, and more transitions, than the results of simulated data. Except the main structure of the meta-stability which has been captured by this analysis, the biological system has much more complicated details within it.
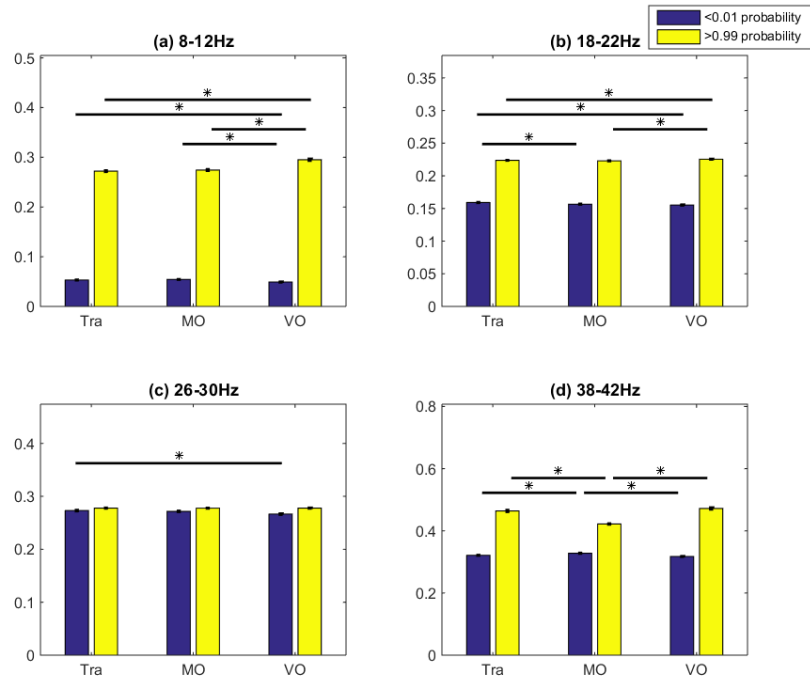
Figure 6.3: Comparison of probability of events that $d < 0.01$ and $d > 0.99$, where d is the successive prime eigenvector inner product. Each error bar represents the standard error of the mean value. Subfigure (a) shows the result of the alpha band (8-12Hz); Subfigure (b) shows the result of the low beta band (18-22Hz); Subfigure (c) shows the result of the high beta band (26-30Hz); and Subfigure (d) shows the result of the gamma band (38-42Hz). The horizontal bar with star indicates the pair that is significantly different (Wilcoxon signed-rank test, $\alpha = 0.025$). These results are highly consistent with the results of topological properties (Comparing to Table 5.1 and Figure 5.2).

From the analysis of eigenvectors, the attractor structure was discovered in the prime eigenvector space. Figure 6.2 gives a glance at the eigenvector trajectory, which shows the existence of the attractors in the eigenvector space. Blocks of high values can be found in Figure 6.2. Each block can be seen as a temporal cluster of those eigenvectors from different time instances. The centres of the clusters should be highly correlated with the attractors. The similar block structure can be found in Figure 4.15 from Chapter 4. The attractors suggest different topological connections of the network, which can be called "meta-networks" of the functional connectivity. The results showed that the network evolves in a way that transits from one meta-structure to another. Therefore, it can be concluded that there is an attractor structure in the evolution of EEG functional connectivity which results in a meta-stable dynamics of the network. The attractors provide a natural partition of the brain states. The concept of defining state space on the brain signal analysis has been proposed a long time ago. Lehmann and his colleges have proposed the concept of EEG microstates, which is based on different EEG power spatial distribution patterns [103, 104, 105, 106, 107, 108]. There are also other methods based on the clustering of network topological properties [109, 110]. Eigenvector is a representation of the instantaneous network which preserves the majority of network structure, so it provides a better way of defining brain signal state space. By clustering the eigenvectors of the whole trajectory, one should be able to identify the individual attractors and, from those attractors, the "meta-networks" of the EEG functional connectivity can be reconstructed.

By performing inner products among successive eigenvectors, it can

be learnt how much the network has changed between the two successive instances, in other words, how smooth the network evolves. Distribution with more events in 1 and less events in 0 means that prime eigenvector is less likely to jump between attractors, suggesting a relative stable network which is more likely to preserve its structure during the evolution. From the results (Figure 6.3), it can be learnt that VO is more stable than Tra and MO trials in the alpha band while MO is more variable than Tra and VO in the gamma band. It can also be found that network in lower frequency is always more stable than high frequency. The reason for this could be that phase-locking synchrony changes slower in low frequency band, which makes the functional connectivity based on the phase synchrony evolves slower as well. Comparing Figure 6.3 with Figure 5.2 and Table 5.1, it can be found that the pairs showing significant difference in the transition frequency of meta-stable states also showed significant difference in the topological properties. It indicates that there is an interrelation between the network dynamics and static properties of functional connectivity.

6.3 Distribution of meta-stable state durations

In order to further investigate the stability of functional connectivity network evolution, the distribution of meta-stable state duration was studied.

6.3.1 Methods

The stability of the meta-stable dynamics was studied by investigating the distribution of meta-stable state duration. The distribution of meta-stable state duration was calculated for every condition. As discussed in the previous section, the meta-stable states were defined as the inner products > 0.99. In every frequency band, all the trials of the same experimental conditions were counted and generated a single distribution for the meta-stable state duration. It was found that the duration distribution of individual trial was exponential. Therefore, the duration distribution was plotted in semi-log coordinates and linear fitted. The slopes of the fitted line were statistically compared with analysis of covariance (ANCOVA) at the level of $\alpha = 0.005$.

6.3.2 Results

Figure 6.4 shows that the in the alpha (8-12Hz) band, slope of VO is significantly larger than Tra and MO. In the low beta (18-22Hz) band, slope of VO and Tra are significantly different, while MO is in the middle of them and does not show significant difference from either of Tra or VO. The distribution of the high beta (38-40Hz) band and the gamma (38-42Hz) band show similar pattern, as it can be observed from the figures that MO has smaller slope than Tra and VO, while Tra and VO are very close to each other. In the high beta band, MO is significantly different from Tra and VO, but in the gamma band no significant difference was found. It could result from that in the gamma band all the meta-stable states tend to be short, which produces this small variance. It was also found that the significantly different pairs in Figure 6.4 also showed significant difference in Figure

(a) 8-12Hz

(b) 18-22Hz

(c) 26-30Hz

(d) 38-40Gz
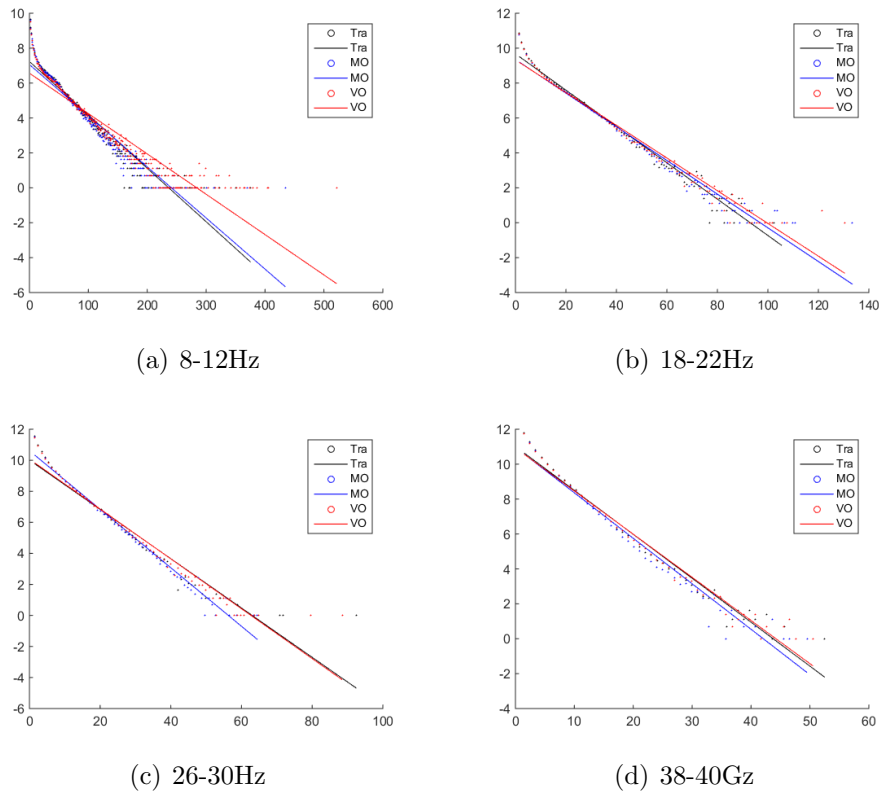
Figure 6.4: The semi-log plot of distribution of meta-stable state duration. Subfigure (a) shows the result of the alpha band (8-12Hz); Subfigure (b) shows the result of the low beta band (18-22Hz); Subfigure (c) shows the result of the high beta band (26-30Hz); and Subfigure (d) shows the result of the gamma band (38-42Hz). The horizontal axis refers to the length of meta-stable states, while the vertical axis refers to the logarithm of number of events. The scatter plot of the distribution was linear fitted. In the alpha (8-12Hz) band, the slope of VO is significantly larger than Tra and MO. In the low beta (18-22Hz) band, the slope of VO and Tra are significantly different, while MO is in the middle of them and does not show significant difference from either of Tra or VO. The distribution of the high beta (38-40Hz) band and the gamma (38-42Hz) band show similar pattern, as it can be observed from the figures that MO has smaller slope than Tra and VO, while Tra and VO are very close to each other. In the high beta band, MO is significantly different from Tra and VO, but in the gamma band no significant difference was found. It could result from that in the gamma band all the meta-stable states tend to be short, which makes small variance. It was observed that longer meta-stable states are more common in low frequency band.

6.3. In the alpha band, for example, VO condition has larger slope, which means it has more and longer meta-stable state segments. From Figure 6.3, it can be learnt that VO has less transitions of meta-stable states than the other two conditions. The same trend can be observed in other frequency bands. As more transitions of the network evolution are likely to cut the meta-stable states into shorter pieces, the condition with fewer transitions found in the inner product time series would have larger slope for the duration distribution. A general trend observed from the results was that longer meta-stable states are more common in low frequency band. This is a consequence of the difference in transition frequency between different frequency bands, as more transitions would make the meta-stable states shorter.

6.3.3 Discussion

The investigation of the duration distribution provides another measurement of the network stability. Larger (flatter) slope suggests there are longer meta-stable states in the prime eigenvector trajectory, which indicates that the network evolves in a smoother way. As shown in the previous section, Section 6.3.2, the meta-stable state duration distribution is largely affected by the number of transitions. These results enhanced the conclusion of the network stability made from the transition frequency analysis. In the alpha band, VO has longer meta-stable states, which suggests that the network is more stable when participants do not perform motion control. In the high beta band and gamma band, MO has shorter meta-stable states, which suggests that the functional connectivity networks of these frequency bands are less stable when participants perform simple move-

ments, while the network becomes more stable when participants perform tracking task, which evolves more complicated visual-motor coordination control. The low beta band, like its result of meta-stable state transitions frequency, only showed one significant pair Tra-VO with MO in the between of them, and p-value of Tra-VO was also quite close to 0.05. These make it hard to lead to any conclusion.

6.4 Lyapunov exponent

Lyapunov exponent is a characteristic measuring the separation rate of the trajectory of a dynamical system¡£ It is usually used to investigate the chaos phenomenon in dynamical systems [68]. The alpha and gamma band showed significant difference between conditions in both topological and meta-stable state dynamical analyses. Therefore as an exploration, the Lyapunov exponent of the network density time series was investigated for the alpha and gamma band. The results are interestingly consistent with all the other static topological and dynamical analysis discussed before. Although this primitive analysis itself is not enough for making conclusion of the chaotic property of the network evolution, it is worthy to report this analysis in this thesis.

6.4.1 Methods

Suppose two trajectories of the system in the phase space have a initial separation δZ_0 at time point 0, and their divergence rate is give by

$$|\delta Z_t| \simeq e^{\lambda t}|\delta Z_0| \tag{6.1}$$

where λ is the Lyapunov exponent. A negative Lyapunov exponent suggests a stable system, which is attracted to a stable fixed point or a limit cycle. A Lyapunov exponent equalling to 0 suggests the dynamical system trajectory has a marginal equilibrium, and could be in the presence of a bifurcation. In those two cases, the dynamical system is not chaotic. If the Lyapunov exponent is positive, however, the dynamical system would be sensitive to small perturbations, and it is considered to be chaotic, the larger the Lyapunov exponent is, the more sensitive the system is to the initial conditions.

In order to investigate the divergence of the system, firstly the phase space needs to be defined. The delay method was used to define the phase space. It was considered a time-delay of 3 successive points in the time series. The time series of the network density was projected into the time-delay phase space, which generated a 3-dimensional trajectory in that phase space. Lyapunov exponent is defined on an infinite trajectory in the phase space, which is usually not true for experimental data. Wolf's algorithm [111, 112, 113, 114] provides an approximate estimation of the Lyapunov exponent. Starting from the beginning of the trajectory, let x_0 be the state being investigated. A "partner" state y_0 would be selected on the trajectory, which should be close enough to x_0, so a threshold of distance and angle was applied. The distance between x_0 and y_0 can be measured, which is noted as δZ_0. Then let both x_0 and y_0 evolve together for a few steps, and we have x_t and y_t. The distance between x_t and y_t can be noted as δZ_t. Using Equation (6.1), the local Lyapunov exponent λ can be calculated. Iterate the same procedures through the whole trajectory in the state space and average all the local Lyapunov exponent, we could get
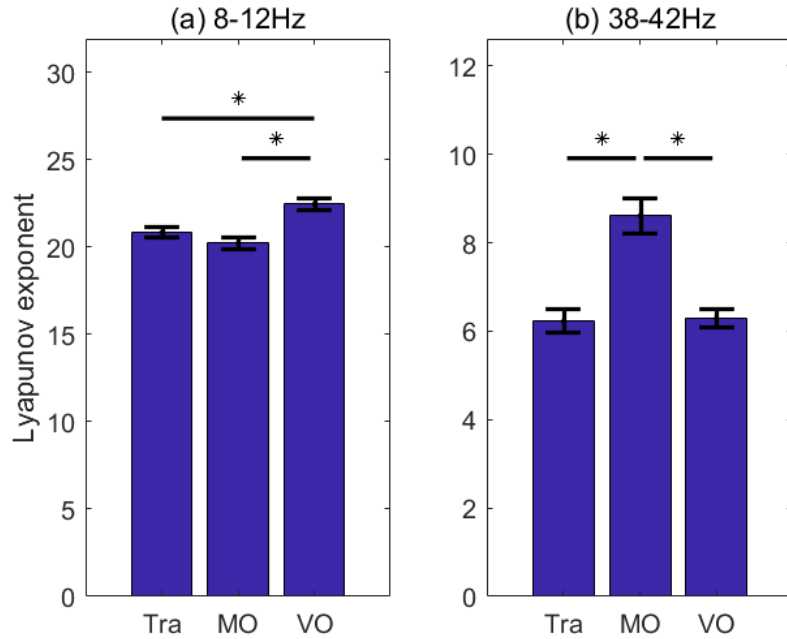
Figure 6.5: Average Lyapunov exponent of the alpha (Subfigure (a)) and gamma band (Subfigure (b)). Each error bar represents the standard error of the mean value. The calculation applied Wolf's algorithm [111, 112, 113, 114], while the dimension of the time-delay phase space was 3. It can be observed that the results are consistent with the analysis of topological properties.

the global Lyapunov exponent. The results are shown in Figure 6.5.

6.4.2 Results

It can be seen that the Lyapunov exponent of VO condition is significantly higher than Tra and MO in the alpha band. In the gamma band, the MO condition has significantly higher Lyapunov exponent than the other two conditions. Comparing with the results shown in Figure 6.3, it can be found that VO condition showed significant differences in both transition probability and Lyapunov exponent in the alpha band, while MO condition showed significant difference from the other conditions in both

transition probability and Lyapunov exponent in the gamma band. It was also interesting to find the consistence of the network density between its time averaging and dynamical property when comparing Figure 6.5 with Figure 5.2. The figures show that the condition with larger time-averaged network density also has larger Lyapunov exponent of the network density trajectory.

6.4.3 Discussion

Comparing Figure 6.5 with Figure 5.2, it can be seen that the results of Lyapunov exponent and average density are quite similar. The consistence between the time-averaged property and the dynamical property could result from that the distribution with larger average value also has larger variance, given the lower bounds of all the distributions are the same (like distribution of network density, where the lower bound is fixed to 0). Therefore, the system that has larger average value and larger variance would have larger divergence in its evolution. However, it may also imply that the network density has different dynamics in different conditions that conversely result in different distribution. In future works, the chaotic dynamics of the network properties will be further investigated.

It should be remarked that the "stability" discussed in this section is different from the stability discussed in the previous sections. In the previous section, the stability was based on the transition frequencies between meta-stable states, as more transitions suggest relative unstable system. In prospect of chaotic system, however, a system is "unstable" if it is sensitive to perturbations. A very "unstable" system would have large Lyapunov exponent and its trajectory would be sensitive to small perturbations. Also,

the stability was measured with different network properties. The meta-stable state discussed in previous sections is a representation of the network cluster structure, while Lyapunov exponent in this section was performed on the time series of network density, which is an overall network measurement which is not necessarily corresponding to different cluster structure. For example, two networks that have two non-overlapped clusters, respectively, may have the same average density. In the alpha band, VO has larger Lyapunov exponent, which suggests it is more chaotic. In the context of inner-product count, VO are significantly more stable than the other two condition. It suggests an interesting structure: although the evolution of the network is less likely to transit between different meta-stable states and keep the network structure, but looking at the network density time series, it is more likely to be perturbed by small fluctuations. In the gamma band, MO shows significantly larger Lyapunov exponent, while it also show higher transition counts. It suggests that MO condition has more transitions between states as well as more sensitive to disturbances.

6.5   Conclusion

In this study, the eigenvector-based dynamical analysis has revealed the attractor structure of the network evolution. The analysis of successive prime eigenvector inner product time series showed that the functional connectivity network would transit between different attractors, which provides a natural partition of the meta-stable states. In the inner product time series, 0 suggests orthogonal successive prime eigenvector, which implies the transition between states, while 1 suggests parallel successive prime

eigenvector, indicating the two eigenvectors belong to the same meta-stable state. The time series of successive prime eigenvector inner product showed a pattern with plateaus of high values which were separated by the sudden decreases of low values (as shown in Figure 6.1). From this pattern, it can be learnt that the plateaus represents the meta-stable states while the low values of inner product indicate transitions between meta-stable states. The number of transitions was compared between different conditions. It was found that in the alpha band, the functional connectivity network of VO trials had less transitions than the Tra, while in the gamma band, the functional connectivity network of MO trials had more transitions than the Tra. Those pairs which showed significant difference in dynamical property were also significantly different in topological properties, which implies an underlying connection between the meta-stable state transitions and the time-averaged topological properties of the functional connectivity. As a further step, the distribution of meta-stable state duration was investigated. Those distributions were exponential, therefore the slopes of their semi-log linear fittings were compared between conditions. The results were consistent with their transition frequencies, as more transitions result in more and shorter fragments of meta-stable states, while fewer transitions result in longer meta-stable states. It suggested that the functional connectivity network in the alpha band is more stable when participants do not perform motion controls, while in the gamma band, the network is more stable when participants performed tracking, which require control of higher precision and heavier load of visual input precession.

Lyapunov exponents of the time series for the network density in the alpha and gamma band were also explored in this work. The results showed

consistence with the topological properties analysis. In the alpha band, the Lyapunov exponent of VO network density trajectory was significantly larger than that of Tra and MO, which suggests that the network density time series evolution of VO was more diverge than other trials. In the gamma band, the Lyapunov exponent of MO network density was significant larger than that of Tra and VO trials as well, which suggests that the network density time series of MO evolves in a more sensitive and chaotic way than other trials. This is a very primitive exploration of chaotic property of functional connectivity network evolution. In future works, further investigation will be done to uncover the chaotic dynamics of the neural network.

Chapter 7

Conclusion and Future Works

Contents

7.1 Conclusion

The human visual-motor coordination is an essential motion control mechanism. This project has explored anticipatory behaviour of humans as well as neural features of visual-motor coordination. In this work, two types of tracking paradigm were applied in behaviour experiment to investigate the anticipatory behaviour of humans. In the full visibility tracking trials, participants showed large variance on their performance and exhibited little anticipatory behaviour. Then the refined intermittent tracking paradigm were performed. Although still affected by the participants variance, the intermittent tracking trials exhibited strong anticipatory behaviour of participators. Two distinctive control modes were found in the intermittent tracking trials, and these two control modes were dominant in the target-visible zone and target-invisible zone, respectively. In the target-visible zone, the visual feedback mode was dominant where partic-

ipants passively followed the target. In the target-invisible zone, instead of depending on the visual feedback, participants performed anticipatory control on the tracer. It was also observed that higher target speed would result in stronger anticipatory behaviour in the tracking paradigm.

For the behavioural analysis, this work explored the anticipatory behaviour in the visual-motor coordination. This work demonstrated the strong anticipatory behaviour of humans with the intermittent tracking paradigm. In the target-visible zone and target-invisible zone, participants used different control mechanisms. The passive visual feedback control mode depends on the viability of the target, so this control mechanism is limited in the target-visible zone. When the target became invisible, participants were forced to use anticipatory control mode. This work also confirmed that higher target speed would result in stronger anticipatory behaviour, which was reported in the previous papers [89, 23].

In the neural signal analysis, the functional connectivity features of visual-motor coordination of humans was investigated. Both static topological properties and the dynamical properties of the functional connectivity network were analysed. It was found that the functional connectivity networks in the alpha and gamma band have significant differences that can distinguish different states of visual-motor coordination loops. In the alpha band, functional connectivity of VO trials had much higher network density, and consequently higher clustering coefficient and average efficiency, than Tra and MO trials, which suggests that motion would result in desynchronisation of the phase-locking networks in the alpha band. In the gamma band, functional connectivity of MO had higher network density, and consequently higher clustering coefficient and average efficiency,

than Tra and VO trials, which suggests that desynchronisation would take place when participants perform a precise visual feedback motion control. In this project, an eigenvector-based dynamical analysis method was developed and tested on a simulated network model. With this new dynamical method, the attractor structure in the prime eigenvector space was discovered, which enables the identification of the meta-stable states by investigating the successive prime eigenvectors inner product time series. Low inner product (close to 0) between successive prime eigenvectors indicates a transition between meta-stable states, while high inner product (close to 1) indicates that the network stayed in the same meta-stable state during this instance. Then, the transition probability of each trial was statistically analysed, the results of which, interestingly, showed consistency with the topological properties: In the alpha band, VO trials had less transitions than Tra and MO trials, while in the gamma band, MO trials had more transitions than Tra and VO trials. This consistency may imply a relation between the network dynamics and its topological properties of the time-averaged static network. Further, the stability of the meta-stable state transition was studied by investigating the distribution of meta-stable state duration. The duration distribution of individual trials was exponential, therefore the linear fitting was applied on the semi-log plot of duration distributions and their slopes were compared. It was found that the distribution of meta-stable state duration is largely affected by the number of transitions, for that more transitions are likely to chop the meta-stable states into smaller pieces and result in shorter meta-stable states, while fewer transitions result in longer meta-stable states. To sum up, both static and dynamical neural features corresponding to different visual-motor co-

ordination states were found in this work.

A number of contributions have been made by this work. A new dynamical analysis method was developed and applied on the neural signal in this work. This method projects the network onto the prime eigenvector of the adjacency matrix, which reduces the dimension and make it easier to represent the network dynamics without losing too much information of the network. This method was proven to be valid with both simulation network model and neural functional connectivity network. In Chapter 4, a simulation synchronous network model was developed to test the eigenvector-based dynamical analysis method. The results showed that the structure changes of the simulated network was captured by the successive prime eigenvectors inner product time series. In Chapter 6, this dynamical method was applied on the functional connectivity of EEG and revealed the meta-stable state dynamics of the functional connectivity networks. An overall picture of prime eigenvectors showed the attractor structure of the prime eigenvector trajectory. Both analysis of simulated network and analysis of EEG functional connectivity suggested that this eigenvector-based dynamical analysis method is capable to uncover the dynamical structure of the network evolution. This eigenvector-based dynamical analysis is not limited to the analysis of neural network, but also can be applied on the analysis of other dynamical networks. This method shows a great potential to uncover the structural changes of the network.

This work also revealed the neural functional connectivity network properties corresponding to the visual-motor coordination. By comparing the tracking paradigm trials with specifically designed reference trials, the neural patterns corresponding to different visual-motor cognitive states can

be identified. In the MO trials, participants performed the same circular movement as Tra trials, but the target was not shown on the display, which made the participants had a different intention of control. In the VO trials, participants only passively observed the pre-recorded Tra trials, without performing any control process. By comparing the functional connectivity network of Tra with MO and VO, respectively, the network differences corresponding to the intention of control and movement was identified separately. Interestingly, it was found that the neural patterns corresponding to the two different parts of the visual-motor coordination, the movement and intention of control, corresponded to the alpha band and gamma band of EEG, respectively. In the alpha band, both topological properties of the static network and dynamical properties of meta-stable state transition were found to be different during the VO trials and the other two conditions. All the three topological properties, mean network density, mean cluster coefficient, and mean efficiency, were significantly different while performing the Tra and VO trials, which indicates that performing motion control would result in desynchronization between different cortex regions, and consequently creating fewer links in the synchrony network. The analysis of eigenvector inner product in the alpha band suggested that the functional connectivity network becomes less stable when participants perform motion control. Similarly in the gamma band, both topological properties and dynamical properties were shown to perform different results in the MO and the other two conditions. The topological properties analysis suggested desynchronization happened when participants were intended to perform the tracking. The eigenvector inner product of the gamma band showed that the functional connectivity network was

127

sparser but more stable when participants performed tracking rather than simple circular movement. The discovery of these functional connectivity differences could help future studies understand the neural mechanism of visual-motor coordination. The results also suggest that the topological properties and the network dynamics have an underlying connection.

7.2 Future works

In Chapter 3, only the behavioural analysis of the anticipatory behaviour was shown, while the neural signal feature related to the anticipatory behaviour was not investigated. Future works will investigate and compare the functional connectivity networks between trials with different target speeds, which could hopefully reveal how the different levels of target speed affect the control mode of visual-motion coordination. It would be also quite interesting to investigate the difference between the functional connectivity networks of target-visible zone and target-invisible zone, which would illustrate the functional connectivity signatures corresponding to the two distinctive control modes.

It was also interesting to notice the different performances of participants in the target-visible zone of intermittent tracking trials and in the full visibility tracking trials. As discussed, this difference of performances could imply that the anticipatory behaviour is affected by the viability of the target, including changes of the target movement or changes of target movement information accessability. More viability would lead to stronger anticipatory behaviour. In future works, different forms of behavioural tasks will be performed in order to investigate how different forms of tar-

get viability would affect the anticipatory behaviour. The viability and its effect of the anticipatory behaviour will also be quantitatively analysed.

In Chapter 4, it was demonstrated that the prime eigenvector could show the dynamics of the network. However, the dynamics revealed by this eigenvector-based dynamical analysis might be incomplete. A paper of Allefeld [58] described a clustering method based on the eigenspectrum, which used similar techniques of the eigenvector. In that paper, they calculated the eigenvalues and corresponding eigenvectors of the adjacency matrix, and claimed that each eigenvalue larger than a given threshold (they derived a particular threshold here, which is 1) suggests one cluster in the network, and more interestingly, the entries of the corresponding eigenvector indicate the membership of nodes. It could suggest that the prime eigenvector only describes the largest cluster in the network. Therefore, it would be worth using the spectral analysis for finding the other smaller clusters in the EEG networks. In order to recover all the information of the network, defining the spectral gap on the eigenspectrum and investigating all the eigenvectors corresponding to the eigenvalues larger than the spectral gap could be necessary. However, as it can be learnt from the network density, the functional connectivity obtained is very sparse, which means there could only be 1 or 2 clusters in the network. It could be possible that the prime eigenvector recover the most of information of the functional connectivity if the functional connectivity only have one connected cluster in the most of the time instance. In future works, the spectral gap will be investigated and the multiple eigenvector method will be developed to analyse network dynamics. Also the sparsity of the functional connectivity will be examined in order to understand how much information the prime

129

eigenvector could recover.

This research has shown the existence of attractor structure in the prime eigenvector space of the functional connectivity network. Each attractor suggests a certain network connection pattern, and the trajectory of prime eigenvectors suggests that the functional connectivity network evolves in a way that transit between the different attractors. Therefore, revealing these attractors would further recover the underlying pattern of the network evolution. In future works, I would apply clustering method on the prime eigenvector trajectory and identify the attractors by looking for the cluster centre of each cluster. In this way, each attractor will be represented as an averaged "eigenvector". It can be considered that these attractors are the eigenvectors of an underlying network which represents the overall dynamics of the functional connectivity network evolution, and these underlying network could be rebuilt with those attractor eigenvectors. Therefore, a unique underlying network can be extracted for every experimental condition. By comparing them, further details of the function connectivity dynamics could be revealed.

Appendix A

EEG Acquisition System and Validation

A.1 Introduction

In this study, there was a demand to synchronise the behavioural data and EEG data. Therefore, an EEG acquisition system was developed for that purpose and as a part of original work of this project. This chapter is presented to describe this system, and show the evidence that this system is able to successfully collect EEG data. In this system, there are two computers, the host PC and the xPC-Target. Both behavioural data streams and EEG data streams were sent to the second computer, which is named xPC-Target (The MathWorks, Inc). The xPC-Target registered the two stream with the same time stamp, and then sent the combined data streams to the main computer, which is referred as the host PC in the following text. In order to show that this extra layer of signal processing would not affect the EEG signals, evidence is shown in this chapter, which suggests that the recorded EEG data have the features reflecting the participants' behaviour. This system can be served as an universal experimental platform which is compatible for all the behavioural paradigms having a request for behavioural-neural signal synchronisation. This chapter first describes the system, then followed by the description of EEG pre-processing and validation.

A.2 System setup

A.2.1 Hardware system

The hardware of the EEG acquisition system included two computers, two A/D modules (AD 12-16 (PCI), CONTEC CO., Ltd), a counter board
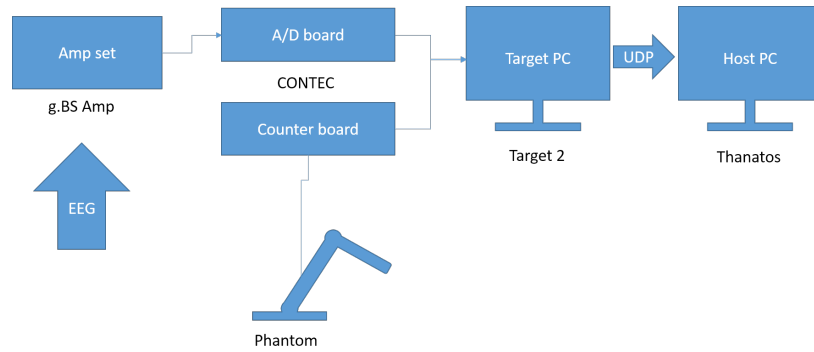
Figure A.1: Experiment hardware system layout
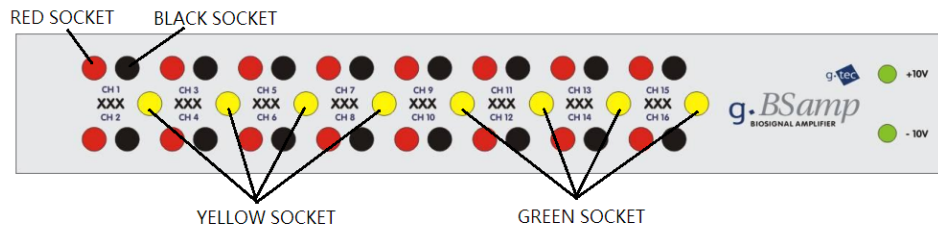
Figure A.2: g.BSamp front side sockets and LEDs. Figure copied from user manual of the product [115].

(CNT32-8M (PCI), CONTEC CO., Ltd), two amplifiers (g.BSamp biosignal amplifier, g.tec) with accessories (cables and electrodes), and a haptic device. The connection layout of the system is shown in Figure A.1. Each amplifier had 16 EEG recording channels, two amplifiers made total 32 EEG channels. Each A/D module had 16 channels as well, therefore each amplifier had a corresponding A/D module. A haptic arm with two encoders, corresponding to X and Y coordinates of the tracer, respectively, was used for participant to control the tracer. An orbicular handle made by 3D printing was fixed in the end of the haptic device in order to make the participant easier to hold. The EEG data streams from the amplifiers were sent to A/D modules for digitalisation, while the behavioural data streams from the encoders of the haptic device were sent to the counter board. The counter board integrated the angle changes and gave the current position of the tracer. Then both of the streams were collected by the xPC-Target, with the operation system of xPC-Target ver. 5.1 (MathWork), in order to register them with synchronised time stamp. Finally, the synchronised data streams were sent to the host PC by user datagram protocol (UDP) packages.

The front and rear panel of the amplifier are shown in Figure A.2 and A.3. 16 red sockets and 16 black sockets are the signal sockets and reference
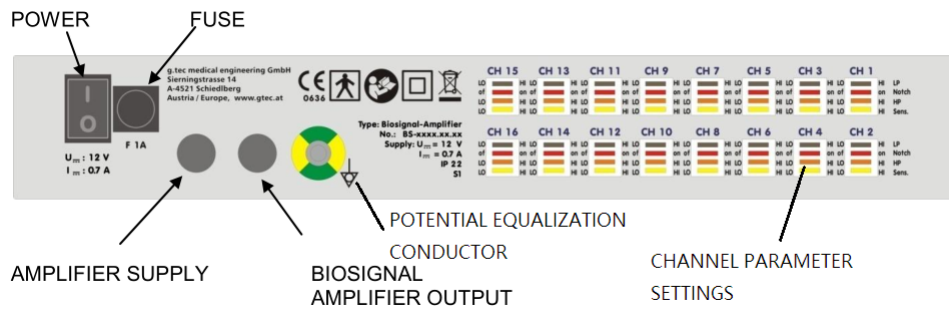
Figure A.3: g.BSamp rear view. Figure copied from user manual of the product [115].
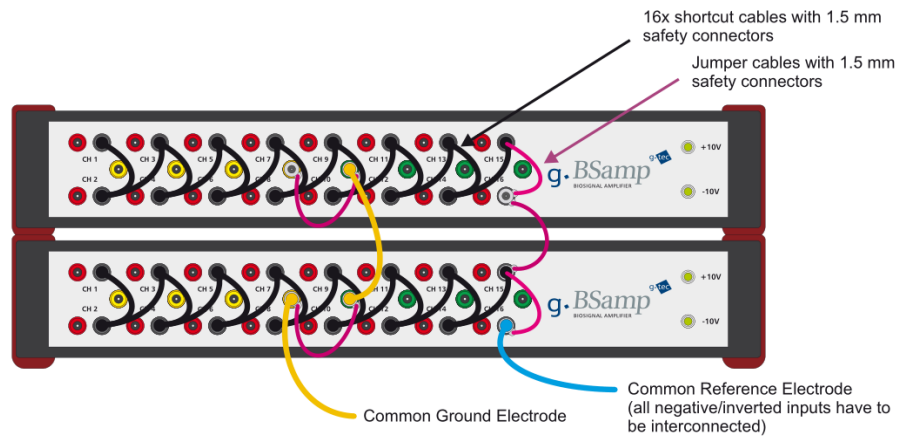
Figure A.4: Configuration for two amplifiers. Figure copied from user manual of the product [115].

sockets, respectively. They are one-to-one corresponded with each other. 8 ground sockets are located in the middle of the front panel, 4 in green and 4 in yellow. The ground sockets with the same colour are connected inside the amplifier, while the ones with different colours are disconnected. During the experiment, reference and ground sockets of two amplifiers were connected as the configuration shown in Figure A.4. All the 16 reference sockets of one amplifier were connected with the shortcut cable, while reference sockets of two amplifiers were connected with the pink jumper cable. 8 ground sockets of one amplifier were connected with the pink jumper cable, while the ground sockets of two amplifiers were connected with the yellow jumper cable. Therefore, the two-amplifier system shared the same ground and reference source.

On the rear side of the amplifier, there is a metal contact bar which is marked as potential equalization conductor in Figure A.3. The two conductors of the two amplifiers were connected during the experiment. On the rear side of the amplifier, there are also 16 channel parameter settings, corresponding to the 16 channels. The 4 parameters of each channel are: "LP" for low pass filter, "Notch" for notch filter at 50Hz, "HI" for high pass filter, and "Sens" for sensitivity. The settings used in this research are: low pass-low; notch filter-on, high pass-low; and sensitivity-low.

A.2.2 Software system

All the data recording and processing during the experiment sessions were completed with programmes of Matlab Simulink (The MathWorks, Inc) environment. The software system has two parts. One part ran on the xPC-Target. This part of programme has 2 functions: First, it calculates the coordinates of tracer from the angles of haptic device encoders; Second, it synchronises the EEG and tracer coordinates data streams and packs the data to send to the host PC. The other part of the software ran on the host PC. This part of programme unpacks the data stream and write the data into files. It also displays the animation of target and tracer.

A.2.3 Data recording configurations

This experiment utilized the 10-20 system for electrode location. 32 electrodes (F3, F1, Fz, F2, F4, FC5, FC3, FC1, FC2, FC4, FC6, C5, C3, C1, Cz, C2, C4, C6, CP3, CP1, CPZ, CP2, CP4, P3, P1, PZ, P2, P4, PO3, POz, PO4, Oz) plus 1 reference electrode (FCz) and 1 ground electrode (AFZ) (g.tec) were applied in the experiment. The behavioural data streams (which were sent to the host PC) included 3 channels, which corresponding to the 3 spatial coordinates, X, Y, and Z, while Z coordinate was unused in this paradigm. Therefore, the combined data streams have

35 channels. These synchronised data streams were sent to the host PC though UDP pack, and written into the file in real time. The sample rate for both EEG and behavioural channels were 1kHz.

A.2.4 Amplifier trouble shooting

During the research, one amplifier showed noisy output and was suspected to be malfunction. A series of systematic tests were performed for trouble shooting. During the trouble shooting, the channel parameter settings kept the same as described in Section A.2.1. The tests were carried out with a signal generator (g.SIGgen, g.tec) which generated the sinusoid signal. First, no shortcut cable or jumper cable was connected on the suspected amplifier. Every channel of the suspected amplifier was tested with the signal generator, and all of the channels showed normal response. Second, all the reference sockets of the suspected amplifier were connected with shortcut cable as Figure A.4, and all the channels were tested with the same fashion. Still all the channels of the suspected amplifier showed normal response. In the next step, the suspected amplifier was connected with 16 EEG electrodes, 1 reference electrode, and 1 ground electrode. The reference and ground sockets of the suspected amplifier were connected together as Figure A.4. All the electrodes, including the reference and the ground electrode, were drowned in a cup of electrolyte solution, in order to simulate the experimental condition in a low impedance environment. The cup was made of plastic, and placed about ten centimetres away from the amplifiers. When we moved our hands near the cup, output signals fluctuated corresponding with our hand movements. Moving electrodes inside the water also generated corresponding fluctuation in the output signals. The same test was performed on the other amplifier, which showed that the output signals of the other amplifier were not affected by any movements. As the final step, all the downstream equipments were replaced and the same test was performed on both amplifiers, which gave the same result. Therefore, the suspected amplifier was malfunction and became extreme vulnerable to the outside disturbance. The report of the above tests was sent to the producer, and the faulty amplifier was replaced later.

A.3 Validation of EEG data

In this section, evidence that show EEG data have the features reflecting the participants' behaviour will be presented in order to validate the recorded EEG data.
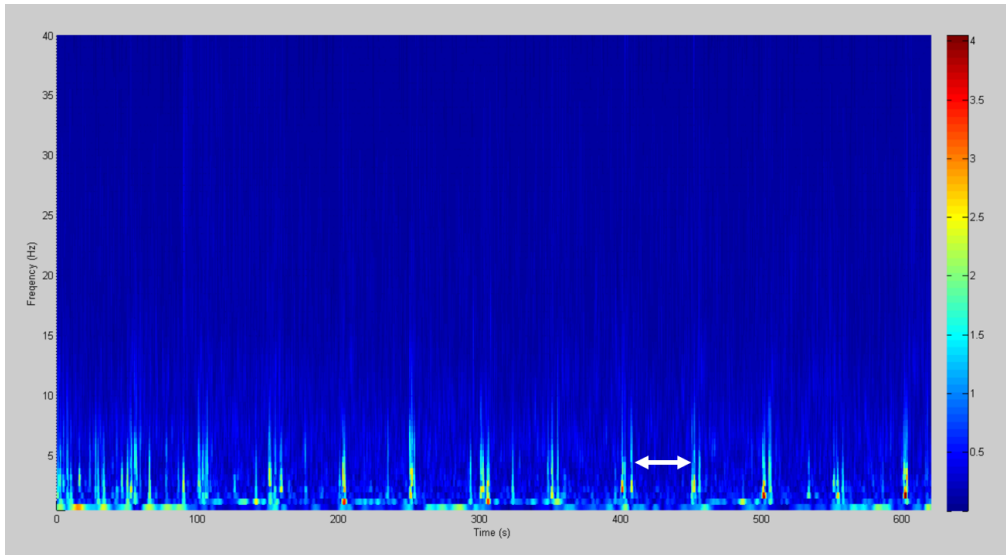
Figure A.5: The time-frequency transform of a single channel in wide-band filtered data. The white double arrow indicates the time duration of a tracking trial. It can be observed that there are 12 tracking trial in this figure. And the durations of the high power around 5Hz are about 10 seconds, which correspond to the experiment setting very well.

A.3.1 Temporal-frequency spectrum

First, the temporal-frequency spectrum of the EEG data was investigated. Continuous wavelet transform (CWT) was applied on the broadband (0.1-50Hz) filtered EEG data of a tracking session (including 12 tracking trials and corresponding short break). The mother wavelet employed in this CWT was Morlet wavelet, which takes the form of the following:

$$\psi(x) = e^{-x^2}\cos(\pi\sqrt{\frac{2}{ln2}}x) \tag{A.1}$$

The result is shown in Figure A.5.

It is very clear that the whole spectrum is separated by some low frequency (centred at about 5Hz) components with high power. The time intervals between the low frequency components correspond accurately to the time of tracking trials. The white double arrow in the figure marks the time duration of a tracking trial. The width of the low frequency components is also identical with the time duration of the 10-second short break period. Those observations suggest that these low frequency peaks appeared in the rest periods of the experiment, and disappeared during the tracking trials, which is a clear difference of the brain signals between the tracking state and the rest state. These components are very likely to be
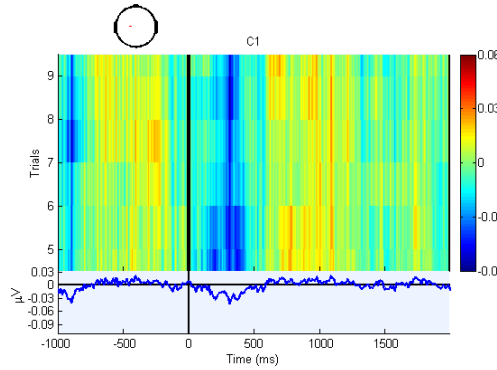
(a) ERP in tracking trial
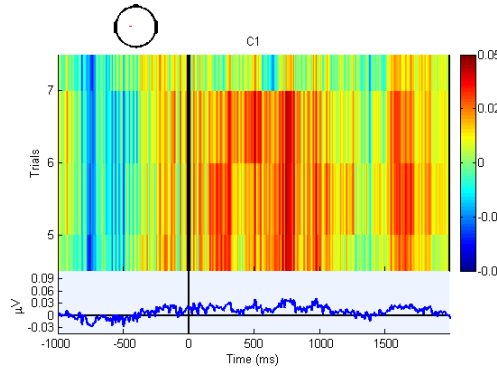
(b) No ERP found in visual only reference trial

Figure A.6: Comparison of event related potential between tracking trial and visual only trial (No movement conducted trial). It is obvious that there is a drop of potential in tracking trial at the time point approximately 400ms, which was not found in visual only trial.

the rest state alpha rhythm.

A.3.2 Event-related desynchronization

The event-related potential (ERP) is a widely recognized symbol for movement [116][117], which is a phenomenon in which the evoked potential appears after the onset of movement. ERP of tracking trials and visual only trials was explored and the results were compared between tracking trials and visual only trials. Each session of tracking trials and visual only trials included 12 trials. As the start time of each trial was the onset of movement in the tracking condition, this time point was chosen to be the 0 point in ERP analysis, while the time range was set from -1s to 2s. The baseline of ERP was calculated from the average of EEG within $[-1, 0]$. It was expected to observe an event-related desynchronization (ERD) in the
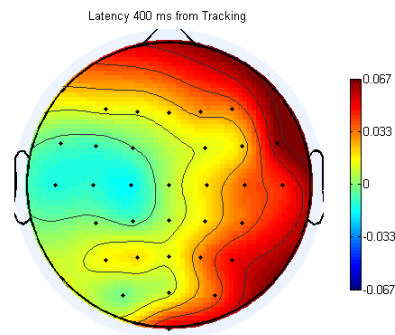
(a) 2-D scalp potential map at 400ms (Tracking trial)
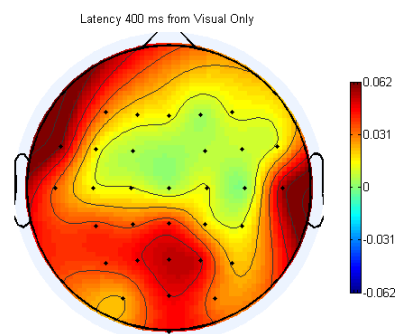
(b) 2-D scalp potential map at 400ms (Visual only trial)

Figure A.7: Comparison of 2-D scalp map at 400ms between tracking trial and visual only trail. It is clear that there is a low potential near the left sensory-motor cortex in tracking trial, as the participant is right-handed. This is corresponding to the drop at 400ms in Figure. The same pattern is not found in visual only trial.

400ms [98]. Figure A.6 shows the results of ERP analysis. It is obvious that a desynchronisation took place at the 400ms in tracking trials, while it was not found in visual only trials. Figure A.7 shows the 2-D scalp ERD plot at 400ms. As the participant is right-handed, it was found that the ERD appeared in the left sensory-motor cortex region when the participant performed tracking task, while the same ERD region was not fount when participant performed visual only trial. The ERD region in Figure A.7 is corresponding to the drop of potential in Figure A.6.

A.3.3 EEG signal averaging

It is well-known that the periodic changing of image contrast causes a corresponding potential change on visual cortex neurons [118]. In this experiment, it is possible that these visual cortex neurons showed the same rhyme as the period of target movement as well. Therefore as a further step of validation, the averaged EEG data of the visual cortex were investigated. Four channels were selected as the sources of the visual cortex EEG signals. These channels were PO3, POz, PO4, and Oz. The EEG time series of these four channels were averaged, generating a single visual cortex signal representation of one trial. And then the visual cortex signal representation of all the 0.1Hz tracking trials were averaged. The same process was done on 0.5Hz tracking trials and 1.0Hz tracking trials. The averaged time series are shown as Figure A.8. It is clear that the signals of 0.5Hz and 1.0Hz trials change corresponding to the frequency of target movement. This phenomenon was not found in the result of 0.1Hz trials. An explanation for no corresponding periodic change in 0.1Hz trials is that the visual cortex is not fully activated because of the very low speed. The visual cortex had spare time to process other visual information and did not respond to the target movement all the time because the low target speed was easy to follow. For the higher speed, 0.5Hz and 1.0Hz, the participant had to pay all attentions so that the visual cortex responded to the target movement all the time, then a corresponding periodic potential change could be observe by averaging out the noise. These results are a further validation of the EEG signal, which show that neuron was activity corresponding to the target movement.

In order to further confirm that the signal comes from the visual cortex, the channel averaging from the other region of brain was assessed with the same method. The frontal region signal was an averaging of three channels: F1, Fz, and F2, while the central region signal was an averaging of three channels as well: C1, Cz, and C2. Results are shown in Figure A.9. This figure shows that the rhythm corresponding to the speed of target was also found in other regions of brain, but with different amplitude. Additionally, the signals from three different parts of scalp, the frontal, central, and rear,
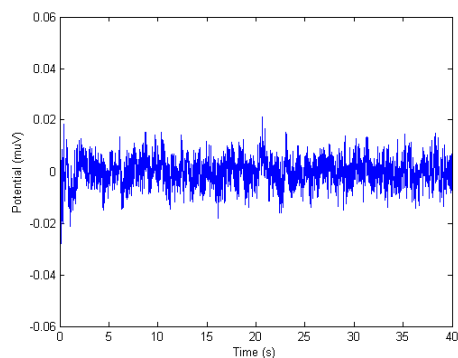
(a) Visual cortex signal of tracking trials (0.1Hz)
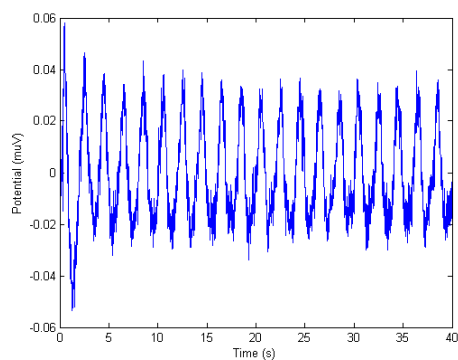
(b) Visual cortex signal of tracking trials (0.5Hz)
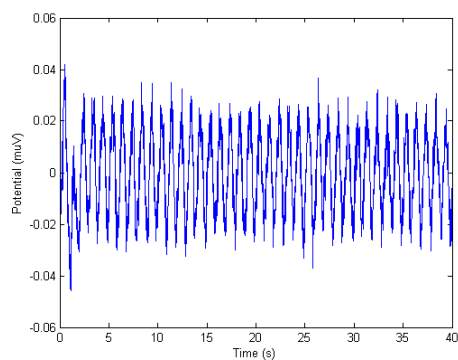
(c) Visual cortex signal of tracking trials (1.0Hz)

Figure A.8: The averaged EEG signal measured near visual cortex when participant performed tracking trials. Each of the subfigure was calculated from the mean signal of 4 channels: PO3, POz, PO4, and Oz, and then averaging of all the tracking trial with the same target speed across participants. It is clear that there is a obvious potential change corresponding to the target movement for 0.5Hz and 1.0Hz. For 0.1Hz the corresponding is not obvious, which may result from the very low speed.
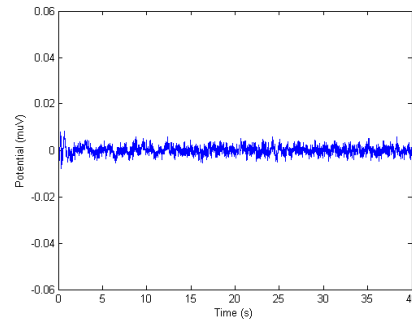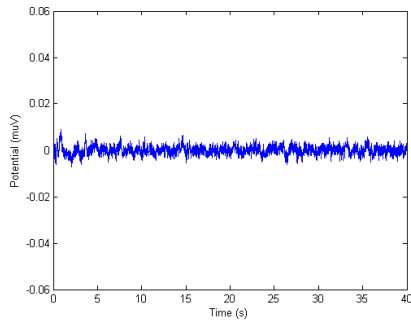
(a) Frontal region signal averaging (0.1Hz)

(b) Central region signal averaging (0.1Hz)
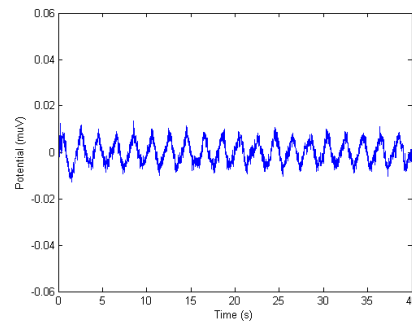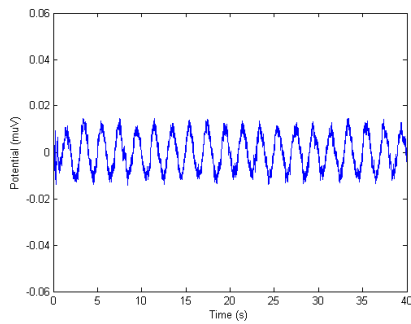
(c) Frontal region signal averaging (0.5Hz)

(d) Central region signal averaging (0.5Hz)
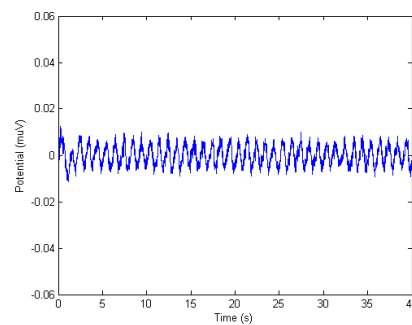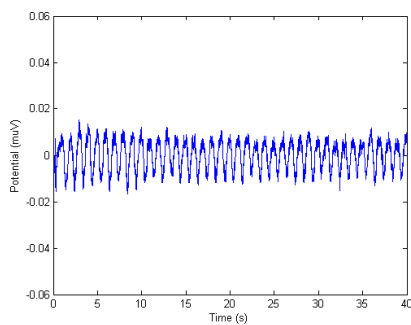
(e) Frontal region signal averaging (1.0Hz)

(f) Central region signal averaging (1.0Hz)

Figure A.9: The EEG signals measured from other region of brain, which shows the same pattern as in visual cortex. Frontal region signal was averaged from F1, Fz, and F2, while central region signal was averaged from C1, Cz, and C2.

141

were plotted into the same figure (Figure A.10) in order to compare their phase. First, it can be seen that the signal from the rear part of the scalp, which represents the visual cortex, has the largest amplitude in all the three trials of different speeds. It can also be learnt that the signal from central scalp always in-phase synchronise with the rear scalp signal, while the signal from frontal scalp always anti-phase synchronise with the rear scalp signal. This phenomenon can be observed in both 0.5Hz trial and 1.0Hz trial. Actually, zooming in the figure of 0.1Hz trial, as showed in Figure A.11, the in-phase and anti-phase relations can be found in 0.1Hz as well. It implies that this relation is a common property of the EEG rhythm. The phase shift in different scalp region makes this low frequency rhythm hardly be artefact, because artefact, like the eye ball movement or body movement, is not likely to generate a phase shifting when travel across the scalp. From the other aspect, the signal of the rear part of scalp seems to be the nearest to the signal source, because the electrical signal decays when travel across a conductor. As the conclusion of this section, the comparisons and analyses of EEG averaging supports that the EEG recording is valid. However, the reason of phase shift between different scalp region is still unclear. In future works, the phase relation of the whole scalp will be explored, and then the source of this rhythm can be found.

A.4 Conclusion

In this chapter, the EEG acquisition system was first described, and then the validation of the recorded EEG data was discussed. Several methods have been applied to show the validation of data. All of them showed the neural responding to the on-going behaviour of participants. This evidence concreted the validation of EEG data.
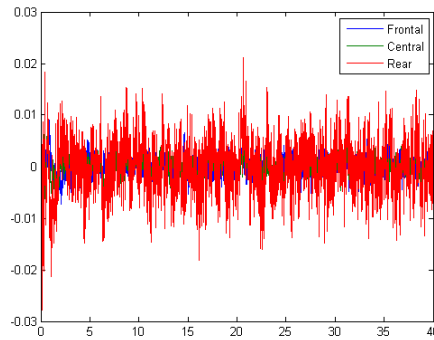
(a) Phase comparison of averaged signal from different scalp region (0.1Hz)
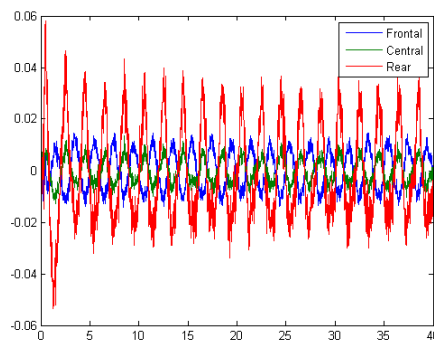
(b) Phase comparison of averaged signal from different scalp region (0.5Hz)
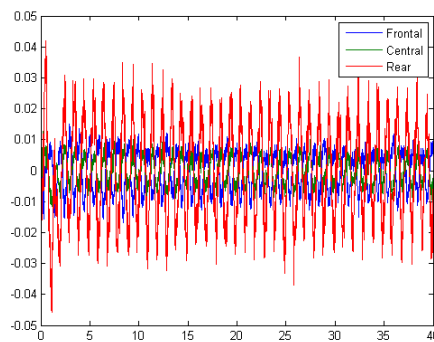
(c) Phase comparison of averaged signal from different scalp region (1.0Hz)

Figure A.10: The superposition of channel averaging signals from different regions of scalp. It can be found that the signal of rear part has the largest amplitude. And also there is a interesting phase relation between the signals from different regions. The rear part signal is in-phase synchronised with central signal, but anti-phase synchronised with frontal signal.
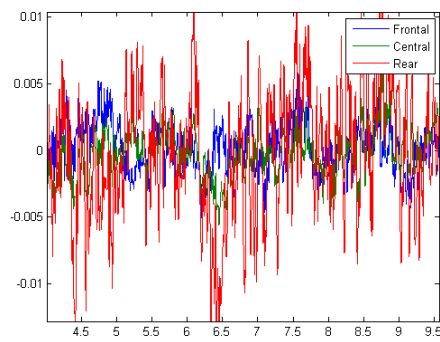
Figure A.11: Details of Figure A.10(a)

Appendix B

Statistical Topological Properties of Individual Participant
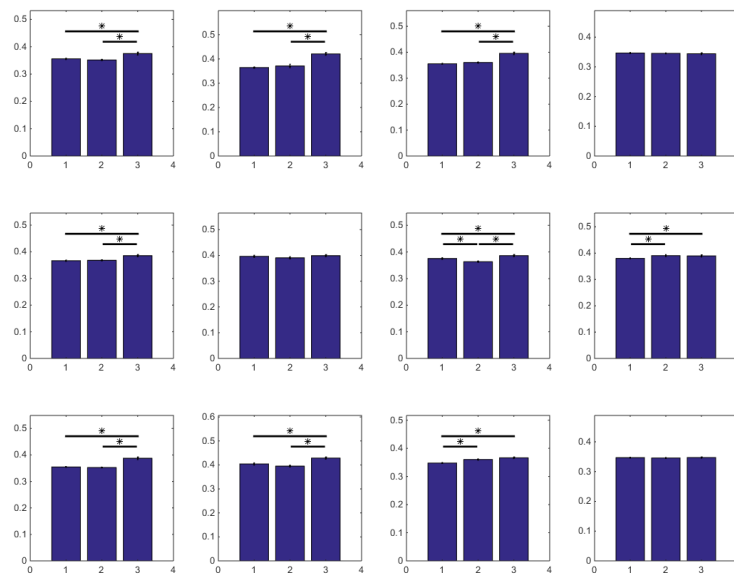
Figure B.1: Functional connectivity clustering coefficient of individual participant in 8-12Hz band.
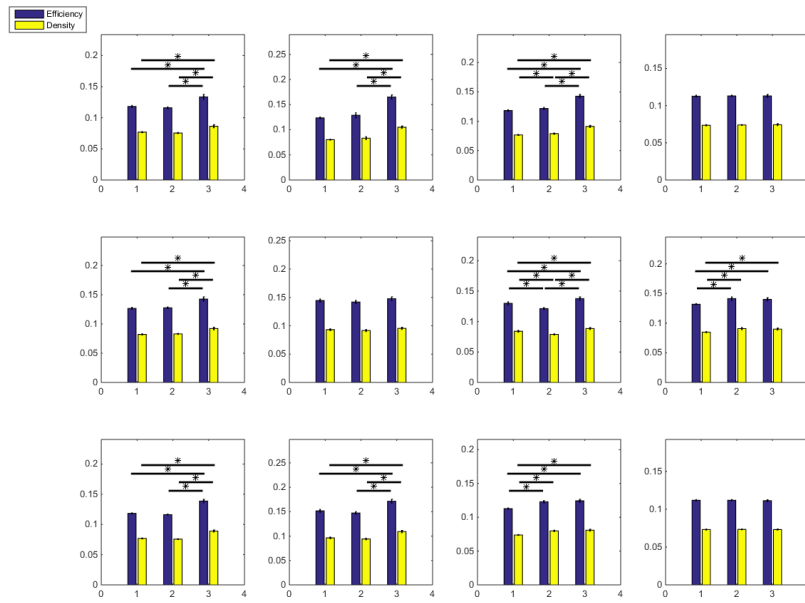
Figure B.2: Functional connectivity efficiency and density of individual participant in 8-12Hz band.
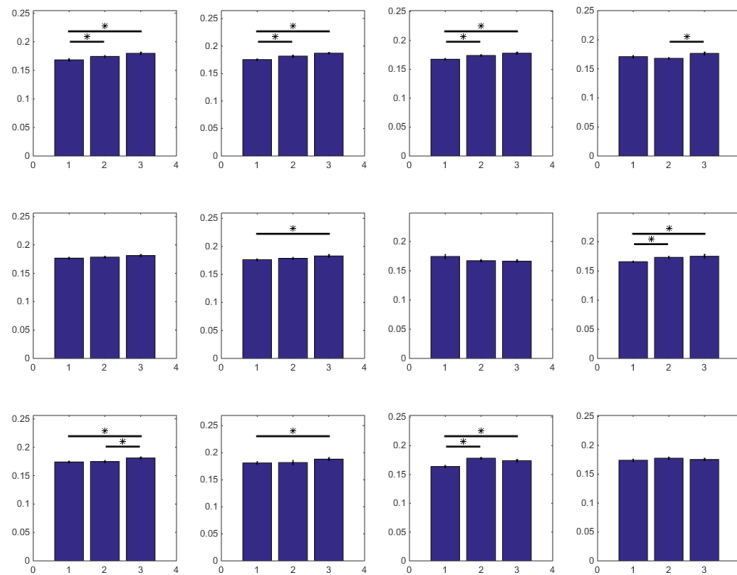
Figure B.3: Functional connectivity clustering coefficient of individual participant in 18-22Hz band.

146
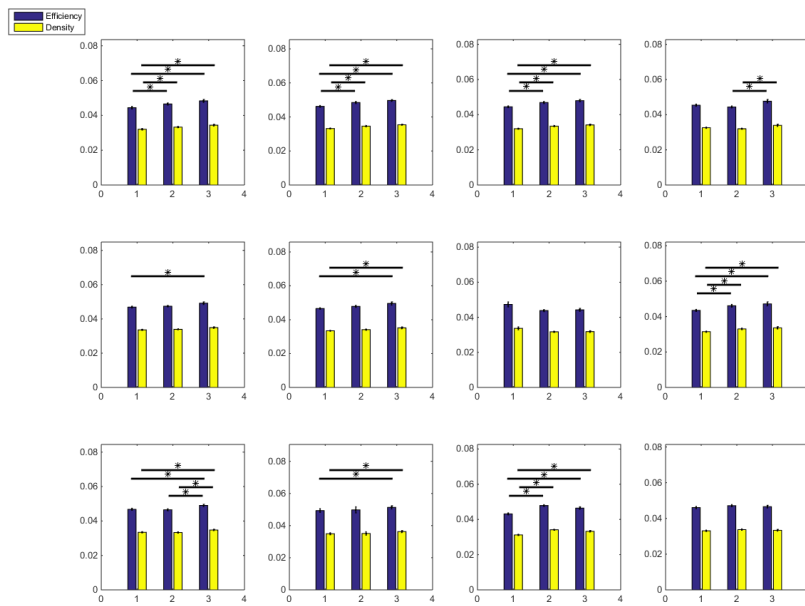
Figure B.4: Functional connectivity efficiency and density of individual participant in 18-22Hz band.
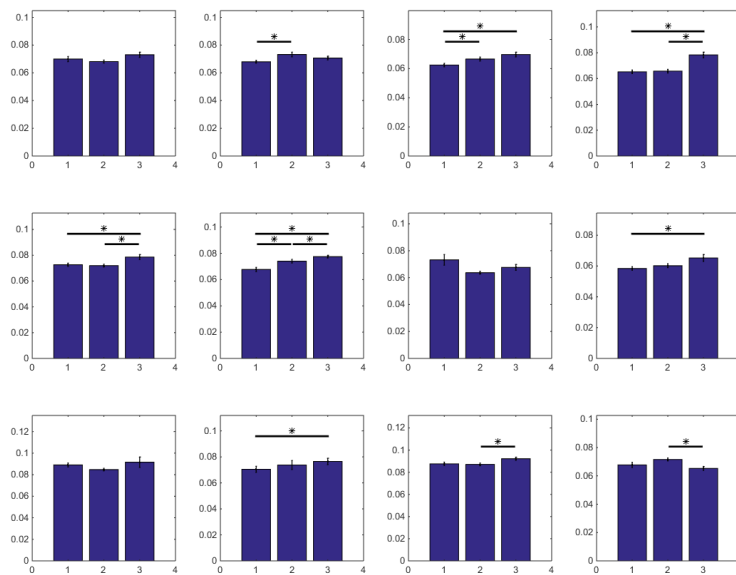
Figure B.5: Functional connectivity clustering coefficient of individual participant in 26-30Hz band.

Figure B.6: Functional connectivity efficiency and density of individual participant in 26-30Hz band.
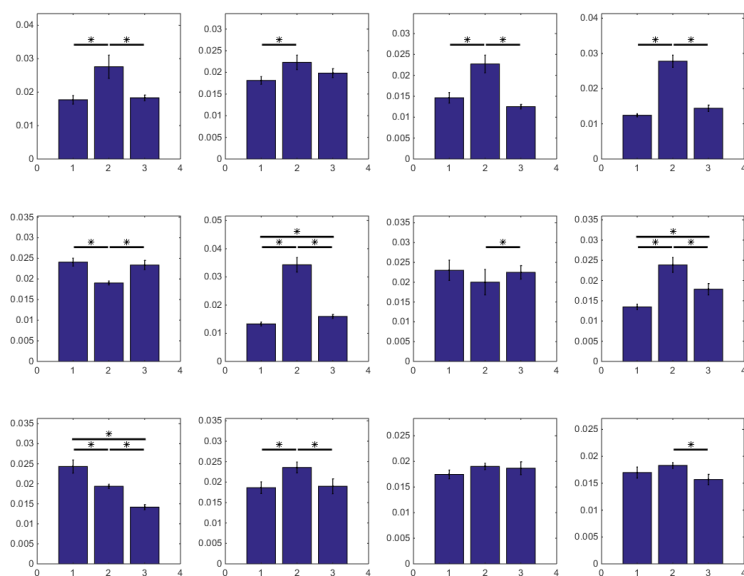
Figure B.7: Functional connectivity clustering coefficient of individual participant in 38-42Hz band.
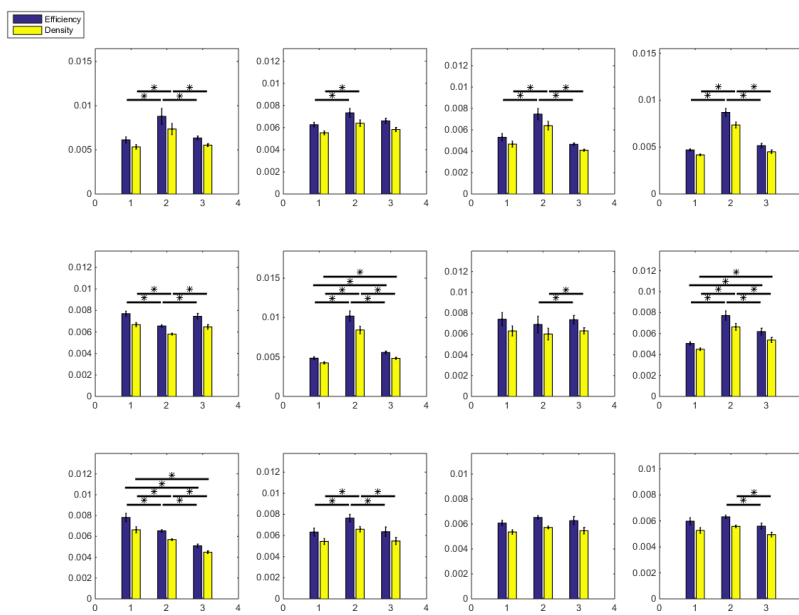
Figure B.8: Functional connectivity efficiency and density of individual participant in 38-42Hz band.

Publication

Declaration

I confirm that this is my own work and the use of all material from other sources has been properly and fully acknowledged.

<div align="right">Xinzhe Li</div>

Acknowledgement

It is not an easy task to finish a PhD, and I am the lucky one because I met many nice and friendly people who helped me, encouraged me, and supported me throughout this journey. I would like to give my sincerest thanks to all of them.

First, I would like to thank my two supervisors, Professor Slawomir Nasuto and Professor Yoshikatsu Hayashi, who have helped me, supported me, motivated me. and patiently guided me through this journey.

I would also like to thank Professor Bruno Mota, whose magnificent skills in physics and mathematics inspired me and turned me from a biologist to an expert in the network theory.

I would like to thank all my colleges, friends, and nice people I met in the University of Reading. I would like to thank Peter Tolson and Karim Djotni for development and maintenance of the haptic device. I would like to thank Nick and Jamie for the help of my experiments. I would like to thank Maitreyee, Henry, Asad and many other people in the School of System Engineering for supporting me in the research. I would like to thank Bowen, Shuguo, Oriental and all the other friends I met in the UK for their companion and kindness, which helped me survive 6 thousands miles away from home.

In the end I would like to specially give thanks to my family. Without the support of my family, I wouldn't be able to achieve all of these. Their support is the shoulder of giant where I can step on and have the view.

List of Figures

154

List of Tables

Bibliography

[1] Pieter R Roelfsema, Andreas K Engel, Peter König, and Wolf Singer. Visuomotor integration is associated with zero time-lag synchronization among cortical areas. *Nature*, 385(6612):157, 1997.

[2] Steven L Bressler, Richard Coppola, and Richard Nakamura. Episodic multiregional cortical coherence at multiple frequencies during visual task performance. *Nature*, 366(6451):153, 1993.

[3] Steven L Bressler. Interareal synchronization in the visual cortex. *Behavioural brain research*, 76(1-2):37–49, 1996.

[4] Brendan Z Allison, Elizabeth Winter Wolpaw, and Jonathan R Wolpaw. Brain–computer interface systems: progress and prospects. *Expert review of medical devices*, 4(4):463–474, 2007.

[5] Bruno H Repp. Sensorimotor synchronization: a review of the tapping literature. *Psychonomic bulletin & review*, 12(6):969–992, 2005.

[6] Jeff Pressing. The referential dynamics of cognition and action. *Psychological Review*, 106(4):714, 1999.

[7] Albrecht J Rilk, Surjo R Soekadar, Paul Sauseng, and Christian Plewnia. Alpha coherence predicts accuracy during a visuomotor tracking task. *Neuropsychologia*, 49(13):3704–3709, 2011.

[8] G Kurillo, B Koritnik, J Zidar, and T Bajd. Analysis of electroencephalographic correlation during grip-force tracking. In *EUROCON 2003. Computer as a Tool. The IEEE Region 8*, volume 2, pages 188–192. IEEE, 2003.

[9] Yanqing Chen, Mingzhou Ding, and Scott J Kelso. Task-related power and coherence changes in neuromagnetic activity during visuomotor coordination. *Experimental Brain Research*, 148(1):105–116, 2003.

[10] Cheng-Ya Huang, Jyong-Huei Su, and Shiou Hwang. Rate control and quality assurance during rhythmic force tracking. *Behavioural brain research*, 259:186–195, 2014.

[11] Chun-Ling Lin, Fu-Zen Shaw, Kuu-Young Young, Chin-Teng Lin, and Tzyy-Ping Jung. Eeg correlates of haptic feedback in a visuo-motor tracking task. *Neuroimage*, 60(4):2258–2273, 2012.

[12] Yoshikatsu Hayashi and Yasuji Sawada. Transition from an antiphase error-correction mode to a synchronization mode in mutual hand tracking. *Physical Review E*, 88(2):022704, 2013.

[13] I Miyake. Researches on rhythmic activity. *Studies From the Yale Psychological Laboratory*, 10:1–48, 1902.

[14] Herbert Woodrow. The effect of rate of sequence upon the accuracy of synchronization. *Journal of Experimental Psychology*, 15(4):357, 1932.

[15] ET Klemmer. Rhythmic disturbances in a simple visual-motor task. *The American journal of psychology*, 70(1):56–63, 1957.

[16] ET Klemmer. Sequences of responses to signals engaged in time only. *Acta Psychologica*, 27:197–203, 1967.

[17] David A Engström, JA Scott Kelso, and Tom Holroyd. Reaction-anticipation transitions in human perception-action patterns. *Human movement science*, 15(6):809–832, 1996.

[18] Paul Fraisse. L'anticipation de stimulus rythmiques. vitesse d'établissement et précision de la synchronisation. *L'année psychologique*, 66(1):15–36, 1966.

[19] Gisa Aschersleben. Effects of training on the timing of repetitive movements. In *Advances in psychology research*, pages 15–30. Nova Science Publishers, 2003.

[20] Gisa Aschersleben. Temporal control of movements in sensorimotor synchronization. *Brain and cognition*, 48(1):66–79, 2002.

[21] Gisa Aschersleben and Wolfgang Prinz. Synchronizing actions with events: The role of sensory information. *Perception & Psychophysics*, 57(3):305–317, 1995.

[22] Bruno H Repp and Amandine Penel. Auditory dominance in temporal processing: new evidence from synchronization with simultaneous visual and auditory sequences. *Journal of Experimental Psychology: Human Perception and Performance*, 28(5):1085, 2002.

[23] Fumihiko Ishida and Yasuji E Sawada. Human hand moves proactively to the external stimulus: an evolutional strategy for minimizing transient error. *Physical review letters*, 93(16):168105, 2004.

[24] JoaquiÌn M Fuster. Network memory. *Trends in neurosciences*, 20(10):451–459, 1997.

[25] John J Hopfield. Neural networks and physical systems with emergent collective computational abilities. *Proceedings of the national academy of sciences*, 79(8):2554–2558, 1982.

[26] David Meunier, Renaud Lambiotte, and Edward T Bullmore. Modular and hierarchically modular organization of brain networks. *Frontiers in neuroscience*, 4:200, 2010.

[27] Moshe Abeles. Local cortical circuits: Studies of brain function, 1982.

[28] Günther Palm. Cell assemblies as a guideline for brain research. *Concepts in Neuroscience*, 1:133–147, 1990.

[29] Howard Eichenbaum. Thinking about brain cell assemblies. *Science*, 261(5124):993–995, 1993.

[30] Rodolfo Llinas, Urs Ribary, Diego Contreras, and Christine Pedroarena. The neuronal basis for consciousness. *Philosophical Transactions of the Royal Society of London B: Biological Sciences*, 353(1377):1841–1849, 1998.

[31] David C Van Essen, Charles H Anderson, and Daniel J Felleman. Information processing in the primate visual system: an integrated systems perspective. *Science*, 255(5043):419–423, 1992.

[32] Francisco Varela, Jean-Philippe Lachaux, Eugenio Rodriguez, and Jacques Martinerie. The brainweb: phase synchronization and large-scale integration. *Nature reviews neuroscience*, 2(4):229, 2001.

[33] William A Gardner. A unifying view of coherence in signal processing. *Signal Processing*, 29(2):113–140, 1992.

[34] Florian Mormann, Klaus Lehnertz, Peter David, and Christian E Elger. Mean phase coherence as a measure for phase synchronization and its application to the eeg of epilepsy patients. *Physica D: Nonlinear Phenomena*, 144(3-4):358–369, 2000.

[35] MHJ Munk, PR Roelfsema, P Fries, AK Kreiter, and W Singer. Rapidly changing synchronisation of gamma-frequency oscillations across visual, parietal, and motor areas of macaque monkeys performing a visuo-motor task. 2000.

[36] Astrid Von Stein, Carl Chiang, and Peter König. Top-down processing mediated by interareal synchronization. *Proceedings of the National Academy of Sciences*, 97(26):14748–14753, 2000.

[37] Eugenio Rodriguez, Nathalie George, Jean-Philippe Lachaux, Jacques Martinerie, Bernard Renault, and Francisco J Varela. Perception's shadow: long-distance synchronization of human brain activity. *Nature*, 397(6718):430, 1999.

[38] Fabrice O Morin, Yuzuru Takamura, and Eiichi Tamiya. Investigating neuronal activity with planar microelectrode arrays: achievements and new perspectives. *Journal of bioscience and bioengineering*, 100(2):131–143, 2005.

[39] CJ Honey, O Sporns, Leila Cammoun, Xavier Gigandet, Jean-Philippe Thiran, Reto Meuli, and Patric Hagmann. Predicting human resting-state functional connectivity from structural connectivity. *Proceedings of the National Academy of Sciences*, 106(6):2035–2040, 2009.

[40] André M Bastos and Jan-Mathijs Schoffelen. A tutorial review of functional connectivity analysis methods and their interpretational pitfalls. *Frontiers in systems neuroscience*, 9:175, 2016.

[41] Andreas K Engel, Pascal Fries, and Wolf Singer. Dynamic predictions: oscillations and synchrony in top–down processing. *Nature Reviews Neuroscience*, 2(10):704, 2001.

[42] Emilio Salinas and Terrence J Sejnowski. Correlated neuronal activity and the flow of neural information. *Nature reviews neuroscience*, 2(8):539, 2001.

[43] Pascal Fries. A mechanism for cognitive dynamics: neuronal communication through neuronal coherence. *Trends in cognitive sciences*, 9(10):474–480, 2005.

[44] Ali Yener Mutlu, Edward Bernat, and Selin Aviyente. A signal-processing-based approach to time-varying graph analysis for dynamic brain network identification. *Computational and mathematical methods in medicine*, 2012, 2012.

[45] Junjie Wu, Junsong Zhang, Chu Liu, Dongwei Liu, Xiaojun Ding, and Changle Zhou. Graph theoretical analysis of eeg functional connectivity during music perception. *Brain research*, 1483:71–81, 2012.

[46] Saeid Mehrkanoon, Michael Breakspear, and Tjeerd W Boonstra. The reorganization of corticomuscular coherence during a transition between sensorimotor states. *Neuroimage*, 100:692–702, 2014.

[47] Mikail Rubinov and Olaf Sporns. Complex network measures of brain connectivity: uses and interpretations. *Neuroimage*, 52(3):1059–1069, 2010.

[48] Stavros I Dimitriadis, Nikolaos A Laskaris, Vasso Tsirka, Michael Vourkas, Sifis Micheloyannis, and Spiros Fotopoulos. Tracking brain dynamics via time-dependent network analysis. *Journal of neuroscience methods*, 193(1):145–155, 2010.

[49] Julia H Downes, Mark W Hammond, Dimitris Xydas, Matthew C Spencer, Victor M Becerra, Kevin Warwick, Ben J Whalley, and Slawomir J Nasuto. Emergence of a small-world functional network in cultured neurons. *PLoS computational biology*, 8(5):e1002522, 2012.

[50] Steven H Strogatz. Exploring complex networks. *nature*, 410(6825):268, 2001.

[51] Réka Albert and Albert-László Barabási. Statistical mechanics of complex networks. *Reviews of modern physics*, 74(1):47, 2002.

[52] Ed Bullmore and Olaf Sporns. Complex brain networks: graph theoretical analysis of structural and functional systems. *Nature Reviews Neuroscience*, 10(3):186, 2009.

[53] Sarah Feldt, Paolo Bonifazi, and Rosa Cossart. Dissecting functional connectivity of neuronal microcircuits: experimental and theoretical insights. *Trends in neurosciences*, 34(5):225–236, 2011.

[54] Lus A Nunes Amaral, Antonio Scala, Marc Barthelemy, and H Eugene Stanley. Classes of small-world networks. *Proceedings of the national academy of sciences*, 97(21):11149–11152, 2000.

[55] Duncan J Watts and Steven H Strogatz. Collective dynamics of "small-world" networks. *nature*, 393(6684):440, 1998.

[56] Neil Robertson, Paul D Seymour, et al. *Graph Structure Theory: Proceedings of the AMS-IMS-SIAM Joint Summer Research Conference on Graph Minors, Held June 22 to July 5, 1991, with Support from the National Science Foundation and the Office of Naval Research*, volume 147. American Mathematical Soc., 1993.

[57] Evar D Nering. Linear algebra and matrix theory. Technical report, 1970.

[58] Carsten Allefeld, Markus Müller, and Jürgen Kurths. Eigenvalue decomposition as a generalized synchronization cluster analysis. *International Journal of Bifurcation and Chaos*, 17(10):3493–3497, 2007.

[59] Ulrike Von Luxburg. A tutorial on spectral clustering. *Statistics and computing*, 17(4):395–416, 2007.

[60] Peter Grindrod and Desmond J Higham. Evolving graphs: dynamical models, inverse problems and propagation. In *Proceedings of the Royal Society of London A: Mathematical, Physical and Engineering Sciences*, page rspa20090456. The Royal Society, 2009.

[61] Marcelo G Mattar, Sharon L Thompson-Schill, and Danielle S Bassett. The network architecture of value learning. *Network Neuroscience*, (Just Accepted):1–27, 2016.

[62] Sitaram Asur, Srinivasan Parthasarathy, and Duygu Ucar. An event-based framework for characterizing the evolutionary behavior of interaction graphs. *ACM Transactions on Knowledge Discovery from Data (TKDD)*, 3(4):16, 2009.

[63] Dan Braha and Yaneer Bar-Yam. Time-dependent complex networks: Dynamic centrality, dynamic motifs, and cycles of social interactions. In *Adaptive Networks*, pages 39–50. Springer, 2009.

[64] Scott A Hill and Dan Braha. Dynamic model of time-dependent complex networks. *Physical Review E*, 82(4):046105, 2010.

[65] Mark A Kramer, Uri T Eden, Eric D Kolaczyk, Rodrigo Zepeda, Emad N Eskandar, and Sydney S Cash. Coalescence and fragmentation of cortical networks during focal seizures. *Journal of Neuroscience*, 30(30):10076–10085, 2010.

[66] Peter J Mucha, Thomas Richardson, Kevin Macon, Mason A Porter, and Jukka-Pekka Onnela. Community structure in time-dependent, multiscale, and multiplex networks. *science*, 328(5980):876–878, 2010.

[67] Christopher M Danforth. Chaos in an atmosphere hanging on a wall. *Mathematics of Planet Earth*, 17, 2013.

[68] Geoff Boeing. Visual analysis of nonlinear dynamical systems: chaos, fractals, self-similarity and the limits of prediction. *Systems*, 4(4):37, 2016.

[69] J Sousa Ramos. Introduction to nonlinear dynamics of electronic systems: tutorial. *Nonlinear Dynamics*, 44(1-4):3–14, 2006.

[70] Ricardo Severino, Alexander Sharkovsky, J Sousa Ramos, and Sandra Vinagre. Topological invariants in a model of a time-delayed chua's circuit. *Nonlinear Dynamics*, 44(1-4):81–90, 2006.

[71] Orlando Gomes, Vivaldo M Mendes, Diana A Mendes, and J Sousa Ramos. Chaotic dynamics in optimal monetary policy. *The European Physical Journal B*, 57(2):195–199, 2007.

[72] Shanbao Tong and Nitish Vyomesh Thakor. *Quantitative EEG analysis methods and clinical applications.* Artech House, 2009.

[73] Philippe Faure and Henri Korn. Is there chaos in the brain? i. concepts of nonlinear dynamics and methods of investigation. *Comptes Rendus de l'Académie des Sciences-Series III-Sciences de la Vie*, 324(9):773–793, 2001.

[74] Henri Korn and Philippe Faure. Is there chaos in the brain? ii. experimental evidence and related models. *Comptes rendus biologies*, 326(9):787–840, 2003.

[75] Steven J Schiff, Kristin Jerger, Duc H Duong, Taeun Chang, Mark L Spano, and William L Ditto. Controlling chaos in the brain. *Nature*, 370(6491):615, 1994.

[76] German Rodriguez-Bermudez and Pedro J Garcia-Laencina. Analysis of eeg signals using nonlinear dynamics and chaos: a review. *Applied mathematics & information sciences*, 9(5):2309, 2015.

[77] Peter T Walling and Kenneth N Hicks. Nonlinear changes in brain dynamics during emergence from sevoflurane anesthesiapreliminary exploration using new software. *Anesthesiology: The Journal of the American Society of Anesthesiologists*, 105(5):927–935, 2006.

[78] J Randall Flanagan and Alan M Wing. The role of internal models in motion planning and control: evidence from grip force adjustments during movements of hand-held loads. *Journal of Neuroscience*, 17(4):1519–1528, 1997.

[79] Sarah J Blakemore, Susan J Goodbody, and Daniel M Wolpert. Predicting the consequences of our own actions: the role of sensorimotor context estimation. *Journal of Neuroscience*, 18(18):7511–7518, 1998.

[80] J Hore, S Watts, and D Tweed. Prediction and compensation by an internal model for back forces during finger opening in an overarm throw. *Journal of Neurophysiology*, 82(3):1187–1197, 1999.

[81] Philipp Vetter and Daniel M Wolpert. Context estimation for sensorimotor control. *Journal of Neurophysiology*, 84(2):1026–1034, 2000.

[82] Yukari Ohki, Benoni B Edin, and Roland S Johansson. Predictions specify reactive control of individual digits in manipulation. *Journal of Neuroscience*, 22(2):600–610, 2002.

[83] Reza Shadmehr, Maurice A Smith, and John W Krakauer. Error correction, sensory prediction, and adaptation in motor control. *Annual review of neuroscience*, 33:89–108, 2010.

[84] RC Miall, DJ Weir, and JF Stein. Manual tracking of visual targets by trained monkeys. *Behavioural brain research*, 20(2):185–201, 1986.

[85] Otmar Bock. Coordination of arm and eye movements in tracking of sinusoidally moving targets. *Behavioural brain research*, 24(2):93–100, 1987.

[86] RE Kettner, S Mahamud, H-C Leung, N Sitkoff, JC Houk, BW Peterson, and AG Barto. Prediction of complex two-dimensional trajectories by a cerebellar model of smooth pursuit eye movement. *Journal of neurophysiology*, 77(4):2115–2130, 1997.

[87] Robert S Turner, Scott T Grafton, John R Votaw, Mahlon R Delong, and John M Hoffman. Motor subcircuits mediating the control of movement velocity: a pet study. *Journal of Neurophysiology*, 80(4):2162–2176, 1998.

[88] M Suh, H-C Leung, and RE Kettner. Cerebellar flocculus and ventral paraflocculus purkinje cell activity during predictive and visually driven pursuit in monkey. *Journal of Neurophysiology*, 84(4):1835–1850, 2000.

[89] Hermann Haken, JA Scott Kelso, and Heinz Bunz. A theoretical model of phase transitions in human hand movements. *Biological cybernetics*, 51(5):347–356, 1985.

[90] Yoshikatsu Hayashi, Yurie Tamura, Kazuya Sase, Ken Sugawara, and Yasuji Sawada. Intermittently-visual tracking experiments reveal the roles of error-correction and predictive mechanisms in the human visual-motor control system. *Transactions of The Society of Instrument and Control Engineers*, 46(7):391–400, 2010.

[91] Nigel Stepp. Anticipation in feedback-delayed manual tracking of a chaotic oscillator. *Experimental brain research*, 198(4):521–525, 2009.

[92] Nigel Stepp and Michael T Turvey. On strong anticipation. *Cognitive Systems Research*, 11(2):148–164, 2010.

[93] Silvia Gago. Spectral techniques in complex networks. *Selectec Topics on Applications of Graph Spectra, Matematicki Institut SANU, Beograd*, 14(22):63–84, 2011.

[94] Yoshiki Kuramoto. Self-entrainment of a population of coupled non-linear oscillators. In *International symposium on mathematical problems in theoretical physics*, pages 420–422. Springer, 1975.

[95] Jürgen Kayser and Craig E Tenke. Principal components analysis of laplacian waveforms as a generic method for identifying erp generator patterns: I. evaluation with auditory oddball tasks. *Clinical neurophysiology*, 117(2):348–368, 2006.

[96] Jürgen Kayser and Craig E Tenke. Principal components analysis of laplacian waveforms as a generic method for identifying erp generator patterns: Ii. adequacy of low-density estimates. *Clinical neurophysiology*, 117(2):369–380, 2006.

[97] J Kayser. Current source density (csd) interpolation using spherical splines-csd toolbox (version 1.1). *New York State Psychiatric Institute: Division of Cognitive Neuroscience*, 2009.

[98] Gert Pfurtscheller and FH Lopes Da Silva. Event-related eeg/meg synchronization and desynchronization: basic principles. *Clinical neurophysiology*, 110(11):1842–1857, 1999.

[99] Catherine Tallon-Baudry and Olivier Bertrand. Oscillatory gamma activity in humans and its role in object representation. *Trends in cognitive sciences*, 3(4):151–162, 1999.

[100] Catherine Tallon-Baudry. The roles of gamma-band oscillatory synchrony in human visual cognition. *Front Biosci*, 14:321–332, 2009.

[101] Andreas K Engel and Wolf Singer. Temporal binding and the neural correlates of sensory awareness. *Trends in cognitive sciences*, 5(1):16–25, 2001.

[102] J Ulbikas, A Cenys, and OP Sulimova. Chaos parameters for eeg analysis. *Nonlinear Analysis: Modelling and Control*, 3:1–8, 1998.

[103] Dietrich Lehmann. Brain electric microstates and cognition: the atoms of thought. In *Machinery of the Mind*, pages 209–224. Springer, 1990.

[104] I Kondakor, Roberto-Domingo Pascual-Marqui, Christoph M Michel, and D Lehmann. Event-related potential map differences depend on the prestimulus microstates. *Journal of medical engineering & technology*, 19(2-3):66–69, 1995.

[105] Arjun Khanna, Alvaro Pascual-Leone, Christoph M Michel, and Faranak Farzan. Microstates in resting-state eeg: current status and future directions. *Neuroscience & Biobehavioral Reviews*, 49:105–113, 2015.

[106] Dietrich Lehmann and Wolfgang Skrandies. Reference-free identification of components of checkerboard-evoked multichannel potential fields. *Electroencephalography and clinical neurophysiology*, 48(6):609–621, 1980.

[107] Dr Lehmann, H Ozaki, and I Pal. Eeg alpha map series: brain microstates by space-oriented adaptive segmentation. *Electroencephalography and clinical neurophysiology*, 67(3):271–288, 1987.

[108] Dietrich Lehmann, Pascal L Faber, Silvana Galderisi, Werner M Herrmann, Toshihiko Kinoshita, Martha Koukkou, Armida Mucci, Roberto D Pascual-Marqui, Naomi Saito, Jiri Wackermann, et al. Eeg microstate duration and syntax in acute, medication-naive, first-episode schizophrenia: a multi-center study. *Psychiatry Research: Neuroimaging*, 138(2):141–156, 2005.

[109] James M Shine, Patrick G Bissett, Peter T Bell, Oluwasanmi Koyejo, Joshua H Balsters, Krzysztof J Gorgolewski, Craig A Moodie, and Russell A Poldrack. The dynamics of functional brain networks: integrated network states during cognitive task performance. *Neuron*, 92(2):544–554, 2016.

[110] James M Shine and Russell A Poldrack. Principles of dynamic network reconfiguration across diverse brain states. *NeuroImage*, 2017.

[111] Alan Wolf et al. Quantifying chaos with lyapunov exponents. *Chaos*, 16:285–317, 1986.

[112] Masaki Sano and Yasuji Sawada. Measurement of the lyapunov spectrum from a chaotic time series. *Physical review letters*, 55(10):1082, 1985.

[113] J-P Eckmann, S Oliffson Kamphorst, David Ruelle, and S Ciliberto. Liapunov exponents from time series. *Physical Review A*, 34(6):4971, 1986.

[114] Paul Bryant, Reggie Brown, and Henry DI Abarbanel. Lyapunov exponents from observed time series. *Physical Review Letters*, 65(13):1523, 1990.

[115] g.tec. *gBSamp Basics*, jun 2014.

[116] W Walter, R Cooper, VJ Aldridge, WC McCallum, and AL Winter. Contingent negative variation: an electric sign of sensori-motor association and expectancy in the human brain. *Nature*, 203:380–384, 1964.

[117] Samuel Sutton, Margery Braren, Joseph Zubin, and ER John. Evoked-potential correlates of stimulus uncertainty. *Science*, 150(3700):1187–1188, 1965.

[118] Andrew F Rossi, Cynthia D Rittenhouse, and Michael A Paradiso. The representation of brightness in primary visual cortex. *Science*, 273(5278):1104, 1996.